Dipl.-Ing. Daniel Wallner

Experimental and Numerical Investigations on Brake Squeal

Development of a Smart Friction Force Measuring Sensor

PhD Thesis

For obtaining the academic degree of
Doctor of Engineering Sciences (Dr. techn.)

achieved at

University of Technology Graz

Assessors:
Univ.-Prof.i.R. Dr.techn. Wolfgang Hirschberg
Institute of Automotive Engineering
University of Technology Graz

Prof. Dr.-Ing. Michael Hanss
Institute of Engineering and Computational Mechanics
University of Stuttgart

Graz, July 2012

This work is dedicated to my deceased mother Helga and my niece Anja.

Abstract

In 1930 a survey examining the question of noise problems was conducted in New York City. Already at that time brake squeal was found to be one of the top-ten noise issues. In the meantime 80 years of intensive research on brake squeal has been conducted and much work has been done to successfully eliminate this problem, which is indeed annoying in its manifestation. Nevertheless, brake squeal is still present. It reduces the comfort of a vehicle and leads to high warranty costs for car manufacturers. This occurs because customers are not willing to accept noisy brakes.

There are several approaches to studying squealing brakes: simulations of analytical minimal models provide a basic understanding of brake squeal mechanisms. Detailed Finite Element Method models simulate the dynamic behaviour of the brake system to avoid squealing brake system assemblies a priori. Finally, experiments on test benches or road testing ensure that the brake system is quiet.

The present thesis examines these approaches and discusses their advantages and disadvantages, as well as their possibilities and limitations. Considerations lead to the question of whether, by means of simulations and reproducible measurements, the influence of the different instability mechanisms can be determined and how the system has to be changed to inhibit friction induced vibrations. Therefore, it is necessary to measure the resulting friction force of the pad as close as possible to the frictional contact between brake disc and pad.

This results in the design of a complex measurement system and the development of an innovative smart friction force measuring sensor using strain gauges. The optimal design of this sensor enables a measurement of the friction force in high resolution up to a very high limit frequency and thus allows the measurement of a superposed high frequency vibration which is only present during squeal occurrence.

Specially manufactured sintered brake pads may deliver a noisy brake system, which is suitable to perform repeatable measurements. Using this complex measurement system, in-depth investigations on single squealing brake applications as well as a sensitivity analysis are performed. The sensitivity analysis is carried out by changing one single parameter of the brake set-up between the measurements and this allows the determination of the individual parameter's influence on the squeal behaviour. The suitability of counter-measures regarding squeal is also determined. In addition, the influence of air temperature and humidity are investigated by performing tests in a climatic chamber.

An innovative complex measurement system is developed, which enables fundamental research on brake squeal. This system allows new insights into this extensive issue to be gained. In addition, the developed sensors can be used for matrix tests, hence as a supporting tool for brake system development. Thus, this work presents a valuable contribution towards reliably quiet brake systems.

Kurzfassung

Eine im Jahr 1930 durchgeführte Umfrage in New York City bezüglich Stadtlärms ergab, dass Bremsenquietschen eines der Top-Zehn-Lärmprobleme war. Seit damals sind über 80 Jahre vergangen, in denen mittels intensiver Forschung unter anderem das akustische Verhalten der Bremsen deutlich verbessert worden ist. Trotzdem quietschen Bremsen zum Leidwesen der Insassen, der Umwelt und der Fahrzeughersteller noch immer. Die Endkunden tolerieren quietschende Fahrzeugbremsen zudem nicht mehr, wodurch es zu hohen Gewährleistungskosten kommt.

Um Bremsenquietschen zu verhindern, gibt es unterschiedliche Untersuchungsansätze: Mittels einfacher Minimalmodelle werden die Instabilitätsmechanismen untersucht und somit ein grundlegendes Verständnis für diese aufgebaut. Mittels der Finiten-Element-Methode wird das dynamische Verhalten der Bremse a priori eruiert, womit ungünstige Bremssystemkombinationen ausgeschlossen werden können. Eine Überprüfung der Simulationsergebnisse sowie die endgültige Freigabe des Bremssystems erfolgen mittels Testfahrten und Komponententests auf Prüfständen.

Diese Ansätze zur Untersuchung von Bremsenquietschen werden für diese Arbeit genutzt und kritisch diskutiert. Des Weiteren wird untersucht, inwieweit es möglich ist, mit der Unterstützung von reproduzierbaren Messungen und Simulationen das akustische Verhalten eines Bremssystems zu verstehen, vorherzusagen und zu beeinflussen. Da Bremsenquietschen das Resultat einer reibungserregten Schwingung ist, wird die Reibungskraft detailliert untersucht. Dafür ist es notwendig, die Reibungskraft so nah wie möglich am Bremsbelag zu messen. Aus diesem Grund wurde ein komplexes Messsystem aufgebaut und ein innovativer Sensor entwickelt, der die resultierende Reibkraft am Belag mit einer hohen Auflösung misst. Dafür wird der Führungsbolzen, der den Bremsbelag im Bremssattel abstützt, gegen einen, mit Dehnungsmessstreifen applizierten, kraftmessenden Bolzen ersetzt. Bei quietschenden Bremsungen kann mittels dieses Sensors eine überlagerte hochfrequente Schwingung der Reibkraft gemessen werden.

Dank speziell dafür gefertigter Sinter-Bremsbeläge mit schlechtem akustischen Verhalten quietscht das untersuchte Bremssystem besonders häufig und ist daher für reproduzierbare Messungen geeignet. Mit dem entwickelten komplexen Messsystem werden einerseits einzelne Bremsungen detailliert untersucht, andererseits wird eine Sensitivitätsanalyse durchgeführt. Dabei wird immer nur ein Parameter des Bremssystems variiert und damit auch die Eignung bekannter Maßnahmen gegen das Bremsenquietschen quantifiziert. Zusätzlich werden die Versuche bei unterschiedlichen Lufttemperaturen und Feuchtigkeiten durchgeführt.

Die vorliegende Arbeit beschreibt die Entwicklung eines innovativen komplexen Messsystems, das Grundlagenforschung an quietschenden Bremsen ermöglicht und neue Einblicke in diese umfangreiche Problematik gewährt. Des Weiteren können die entwickelten Sensoren auch für umfangreiche Sensibilitätsstudien verwendet werden. Somit wurde ein wertvoller Beitrag für die Entwicklung von leisen Bremssystemen erarbeitet.

Statutory Declaration / Eidesstattliche Erklärung

I declare that I have authored this thesis independently, that I have not used other than the declared sources / resources, and that I have explicitly marked all material which has been quoted either literally or by content from the used sources.

Ich erkläre an Eides statt, dass ich die vorliegende Arbeit selbstständig verfasst, andere als die angegebenen Quellen/Hilfsmittel nicht benutzt, und die den benutzten Quellen wörtlich und inhaltlich entnommenen Stellen als solche kenntlich gemacht habe. Die Arbeit wurde bisher in gleicher oder ähnlicher Form keiner anderen Prüfungsbehörde vorgelegt und auch noch nicht veröffentlicht.

Graz, 01. July 2012

Acknowledgement

I would like to thank all those who helped me during my work on this doctoral thesis. First of all I want to thank the head of the Institute of Automotive Engineering at Graz University of Technology and my supervisor Univ.-Prof.i.R. Dr.techn. Wolfgang Hirschberg. He gave me the great chance to work as a scientific project researcher on a complicated, challenging and in its manifestation in daily life rather annoying topic: the squealing of brakes. I extremely enjoyed the fruitful discussions with him and his encouraging words helped me through the hard times of this work. Thank you.

I am also grateful to Prof. Dr.-Ing. Michael Hanss for acting as an assessor and for the especially inspiring discussions in Phoenix and Stuttgart. His input often delivered a new point of view on my work.

A special thanks also to all colleagues at the institute, above all those who worked on the test-bench. The development of the complex measuring system was hard work and without the help of Dipl.-Ing.(FH) Stefan Bernsteiner, Erich Erhart and Andreas Podlipnig it would never exist. I also want to thank Univ.-Doz. Dr.techn. Arno Eichberger, who partially took over the supervision in the final phase of my thesis. Thanks also to all my co-working students who helped me greatly. I want to thank all my colleagues at the institute for the great support over the last years.

I also would like to mention the industrial partners of my research work. Special thanks for the financial support and the feedback go to Dipl.-Ing. Christoph Fankhauser, Dipl.-Ing. Alexander Rabofsky, Dipl.-Ing. Gerhard Rieder and Dipl.-Ing. Michael Ruß from MAGNA Steyr Fahrzeugtechnik. The interesting discussions and the subsequent suggestions resulted in a continuous evolution of this doctoral thesis. Additionally, I have to thank MIBA Frictec GmbH for the production of the sintered brake pad prototypes.

Last but not least I have to thank my family. My parents, who have supported and encouraged me since childhood; my older sister, who will always help me if things go wrong and my brother-in-law who helps her to help me. Finally I want to thank my niece: a smile from her is perhaps the best way to relieve stress. Therefore, my thanks go to my deceased mother Helga, my father Herbert, my sister Nora, her husband Harry and their child Anja, who was born while I was finalising this thesis.

Daniel Wallner
Graz, July 2012

Contents

Nomenclature

Symbol	Unit
Abbreviations	
Chap.	Chapter
Coef.	Coefficient
Equ.	Equation
Ext.	Extraction
Fig.	Figure
Freq.	Frequency
Tab.	Table
Acronyms	
ABS	Anti-lock Brake System
CAx	Computer Aided
CAD	Computer Aided Design
CAE	Computer Aided Engineering
CEA	Complex Eigenvalue Analysis
COP	Carry-Over Parts
CoP	Centre of Pressure
DFT	Discrete Fourier Transform
DMU	Digital Mock-Up
DoF	Degree of Freedom
DTV	Disc Thickness Variation
ECS	Eddy Current Sensor
FEA	Finite Element Analysis
FEM	Finite Element Method
FFT	Fast Fourier Transformation
NVH	Noise, Vibration and Harshness
ODS	Operational Deflection Shape
RMS	Root Mean Square
SAE	Society of Automotive Engineers
SNM	Squeal Noise Matrix
SNO	Squeal Noise Occurrence
SNR	Signal to Noise Ratio
SOP	Start of Production
SPL	Sound Pressure Level
TA	Transient Analysis

Symbol	Unit	
TAS		Triaxial Acceleration Sensor
TPA		Transfer Path Analysis
Matrices and Vectors		
$\mathbf{C}$		Covariance Matrix
$\mathbf{D}$		Damping Matrix
$\mathbf{F}$		Force Vector
$\mathbf{G}$		Gyroscopic Matrix
$\mathbf{K}$		Stiffness Matrix
$\mathbf{M}$		Mass Matrix
$\mathbf{N}$		Circulatory Matrix
$\mathbf{R}$		Correlation Matrix
$\mathbf{S}$		Sensor Results Vector
$\mathbf{T}$		Measurement Result Matrix
$\mathbf{Y}$		Discrete Signal Vector Frequency Domain
$\mathbf{u}$	m	Displacement Vector
$\dot{\mathbf{u}}$	$^{\mathrm{m}}/_{\mathrm{s}}$	Velocity Vector
$\ddot{\mathbf{u}}$	$^{\mathrm{m}}/_{\mathrm{s}^2}$	Acceleration Vector
$\mathbf{y}$		Discrete Signal Vector Time Domain
$\mathbf{z}$		Position Vector
Latin Letters		
A	m	Amplitude
A	m^2	Area
B	m^2	Brake Coefficient
C		Centre
E	J	Energy
E		Expansion Mode
F	N	Force
G	N	Force of Gravity
H	m	Height
H		Hourglass Mode
J	kgm^2	Moment of Inertia
L	m	Length
N		Shape Function
P		Point
P	W	Power
R		Region
S	$^{\mathrm{mV}}/_{\mathrm{V}}$	Shear Strain Signal
S		Shear Mode
SPL	dB	Sound Pressure Level
T	Nm	Torque

Symbol	Unit	
W	J	Work
Y	$^{N}/_{m^2}$	Young's Modulus
a	$^{m}/_{s^2}$	Acceleration
a		Polynomial Coefficient
b	$^{s}/_{m}$	Friction Velocity Factor
d	$^{Ns}/_{m}$	Damping Rate
f	$^{1}/_{s}$	Frequency
f_B		Brake Force Distribution
$\mathrm{f}(\xi)$		Function
g	$^{m}/_{s^2}$	Gravity
g	$^{Ns}/_{m}$	Damping Coefficient
$\mathrm{g}(\xi)$		Approximation Function
i		Imaginary Unit
k	$^{N}/_{m}$	Spring Rate/Stiffness
m	kg	Mass
m		Nodal Circle
n		Nodal Diameter
n		Degree (Order)
p	$^{N}/_{m^2}$	Pressure
p	Pa	Sound Pressure
$\mathrm{p}_n(\xi)$		Polynomial Function
r	m	Radius
s	m	Displacement/Distance
t	sec	Time
v	m	Displacement
v	$^{m}/_{s}$	Velocity
$\mathrm{w}(\xi)$		Weight-function
x	m	Displacement
$\dot{x}$	$^{m}/_{s}$	Velocity
$\ddot{x}$	$^{m}/_{s^2}$	Acceleration
x		Coordinate Axis
y		Coordinate Axis
z		Coordinate Axis
z		Dimensionless Deceleration
Greek Letters		
Δ		Difference
Ψ		Static Load Distribution
α	rad	Cone Angle Brake Pad
α	rad	Deformation Angle

Symbol	Unit	
β	rad	Installation Angle
γ	rad	Angular Deviation
δ		Kronecker Delta
δ		Real Part of Complex Eigenvalue
ζ		Coordinate Axis FEM
η		Coordinate Axis FEM
η		Efficiency
λ		Eigenvalue
λ		Wavelength
μ		Friction Coefficient
ν		Poisson's Ratio
ξ		Coordinate Axis FEM
ρ	$\mathrm{kg/m^3}$	Density
τ	$\mathrm{N/m^2}$	Friction Force per Area Unit
τ		Shear Strain
τ	s	Time Constant
ϕ		Coordinate Axis
ϕ		Rear Axle Brake Force Proportion
χ		Ratio of Gravity Height to Wheelbase
ω	$\mathrm{rad/s}$	Circular Frequency
ω		Imaginary Part of Complex Eigenvalue
ω	$\mathrm{rad/s}$	Rotational Speed
Indices		
B		Brake
C		Conveyor Belt
C		Curve Path
CO		Cut-Off
F		Friction
F		Front
G		Gravity
I		Inner
L		Linear
L		Longitudinal
M		Measured
N		Normal
O		Outer
P		Possible
Q		Quadratic
R		Rear
RMS		Root Mean Square
S		Sampling

Symbol	Unit	
S		Squeal
SG		Strain Gauge
TH		Threshold
axi		Axial
cri		Critical
d		Damping
d		Disc
dyn		Dynamic
eff		Effective
ext		External
hyd		Hydraulic
k		Stiffness
kin		Kinetic
max		Maximum
min		Minimum
p		Pad
ref		Reference
rel		Relative
s		Scaled
sl		Sliding
st		Static
sum		Sum
veh		Vehicle

1. Introduction

1.1. Background

The automotive industry is faced with continuously increasing demands regarding reliability, safety, sustainability and of course acoustics. Hence also the *Noise, Vibration and Harshness* (NVH) characteristics of brake systems gain in importance.

Among others, three main trends drive current brake development:

- Firstly, regard has to be taken of the increase in engine power and vehicle weights of cars in the last decades. Therefore, higher velocities can be reached with heavier vehicles, which otherwise increase the maximum obtainable kinetic energy of the vehicle. This kinetic energy is one of the main driving factors in brake design and determines the size and type of the brake system. Figure 1.1 shows this progress for the vehicle weight and the maximum engine power for several vehicle series from the small and large family car class.

- Secondly, cars have become quieter in the last decades. This was necessary because of the expectations of customers, who no longer tolerate noise levels which were acceptable 20 years ago [91].

- Thirdly, the development of new vehicle and driving concepts, such as electric vehicles, will lead to a further lowering of vehicle noise in urban regions. Further the number of brake applications will decrease, because electric motors are able to recuperate kinetic energy. In future brakes will be used mainly for emergency braking and for brake to halt from low speeds, where deceleration using the electric motor does not make sense.

Exactly these trends, hence increasing demands on braking performance as well as infrequent and gentle low speed brake applications, lead to a squealing brake system. This situation is compounded by customer satisfaction. Of course, a squealing brake does not influence the braking performance, but customers are simply not willing to accept noisy brakes. Akay [12] refers to a record of a survey conducted in New York City in 1930, wherein brake noise was one of the top-ten noise problems. In this publication the estimated warranty costs as a result of NVH issues in North America are declared to reach one billion dollars each year. According to Abendroth and Wernitz [4], friction material suppliers spend up to 50 percent of their engineering budgets on NVH issues.

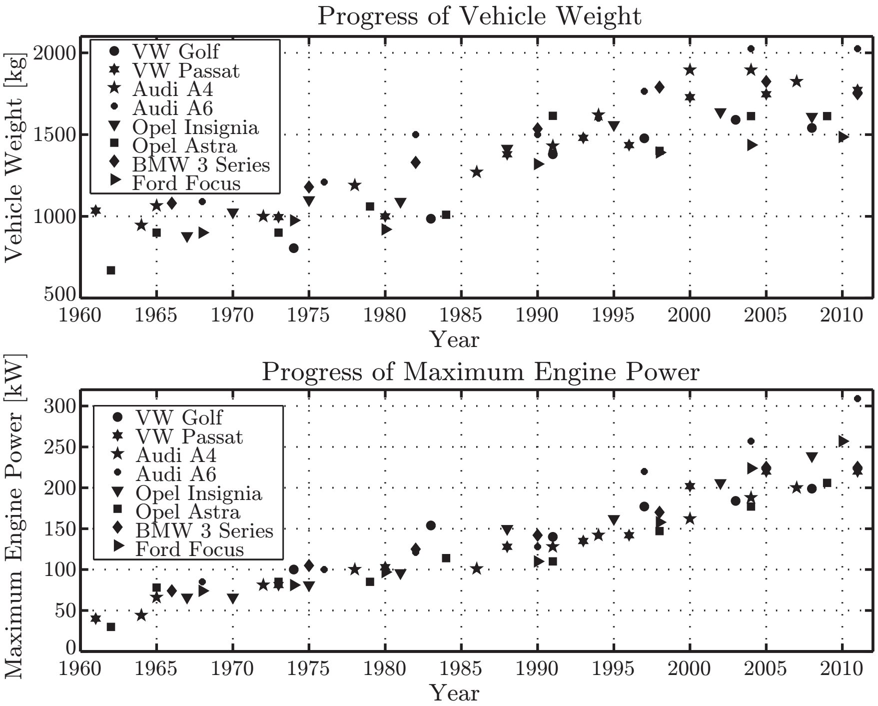

Figure 1.1.: Progress of vehicle weight and maximum available engine power of several vehicle series from the small and large family cars class over the last decades.

1.1.1. Brake System

The brake system reduces the velocity of the car by converting kinetic energy into thermal energy, hence heat because of adhesion, visco-elasticity and friction. The maximum achievable kinetic energy E_{kin} depends on the gross vehicle weight m_{veh} and the top speed v_{veh}. The corresponding equation reads

$$E_{\text{kin}} = \frac{m_{\text{veh}} \cdot v_{\text{veh}}^2}{2}. \tag{1.1}$$

Additionally, automotive brakes do not have a defined operation point. Depending on the current velocity and the required deceleration, the brake performance demand can be calculated. Neglecting all driving resistances such as air, roll and gradient resistance, the entire brake force F_B for a deceleration a is given by Newton's second law:

$$F_B = m_{\text{veh}} \cdot a. \tag{1.2}$$

The maximum braking power is the key requirement of a brake system. It can be determined as follows: Mechanical power is the time derivative of work W. Work is defined as the line integral of a force F that travels along a path C and reads

$$W_C = \int_C F \cdot \mathrm{d}x = \int_C F \cdot \frac{\mathrm{d}x}{\mathrm{d}t} \cdot \mathrm{d}t = \int_C F \cdot v \cdot \mathrm{d}t. \tag{1.3}$$

The time derivative of the work equals the instantaneous power and results in

$$P = W'_C = F \cdot v. \tag{1.4}$$

In the case of decelerating a vehicle, the force F equals the brake force F_B while the curve path C is the braking distance and due to this v equals v_{veh}. By combining Equ. (1.2) and Equ. (1.4), the current total braking power demand P_B depending on demanded deceleration a, current velocity v_{veh} and vehicle mass m_{veh} is given as

$$P_B = F_B \cdot v = m_{\mathrm{veh}} \cdot a \cdot v_{\mathrm{veh}}. \tag{1.5}$$

Figure 1.2 presents the curves at constant braking power demand P_B taking a vehicle mass of 2200 kg into account. The braking power demand ranges from almost zero at low speeds and low deceleration, which is the classical squealing brake application, to far over 1000 kW for full braking at top speed.

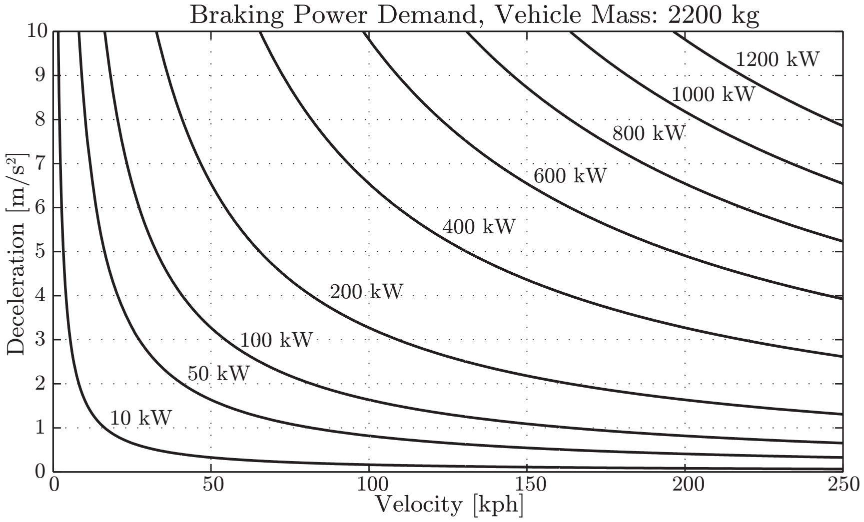

Figure 1.2.: Braking power demand depending on deceleration and speed.

Today, the dominant brake system type is the disc brake system. Due to this, it is this system which is discussed in the following. A disc brake consists of a brake disc which is fixed to the rolling wheel. Two brake pads push from either side onto the disc when the brake is used. Due to the friction between pads and disc, kinetic energy is transformed into heat and the wheel is decelerated. A standard hydraulic disc brake consists of the following parts:

Brake Disc: This is the central part of the brake system which is coupled with the rotating wheel. It is usually made of cast iron. Some developments for high performance brakes lead to brakes made of composites such as reinforced carbon-ceramic or ceramic matrix composites. If necessary, ventilated discs are used because of the better heat dissipation.

Drills and slots improve the performance under wet conditions by preventing water film and furthermore steam layer formation in the contact area which significantly reduces the friction coefficient at the beginning of the brake application. Thus the response of the brake system is increased. Figure 1.3 shows different ventilation channel designs of brake discs with drills.

Figure 1.3.: Examples of different ventilation channel designs in brake discs.

Brake Pads: During braking they are pressed on each side of the brake disc. Depending on the contact pressure, the resulting effective radius and the current friction coefficient between disc and pads the brake torque results.

Automotive brake pads consist of a friction material, typically made of organic material, and a carrier, the pad backplate (usually made of steel sheet). The composition of the friction material, hence the mixture, is confidential know-how of brake pad material manufacturers. Regarding squeal, different lubricants and softeners are added to the mixture, which mostly reduce the wear performance. Hence a trade-off between squeal and wear has to be found. Thereby, the lubricants should not decrease the friction coefficient.

Brake Pistons: The pistons of conventional brakes are loaded by the brake pressure and press the brake pads to the brake disc. Using more pistons results in a more even contact pressure distribution. This leads to a smooth thermal energy input and reduces the squeal possibility, the formation of *hot spots* and wear. In the meantime there are brake systems with up to twelve brake pistons for racing and sport cars.

Brake Caliper: This is the housing for the brake pad and the brake pistons and distributes the brake fluid to them. There are two different kinds of disc brake systems which differ in their caliper type: the floating and the fixed caliper.
Figure 1.4 shows a image of a floating caliper. The feature of the floating caliper is that the outer part of the caliper (1) can slide with respect to the disc parallel

to the rotation axis. Only on the inner side there are pistons which press the inner brake pad until contact. Then the outer part of the caliper (1), the so-called *fingers*, pull the outer brake pad (4). In this way brake pressure is applied to the brake pads using pistons only on one side. The shown caliper in Fig. 1.4 has only one piston (2) and the inner brake pad (3) is disassembled for better visibility.

The fixed caliper is fixed with respect to the disc and has the same number of pistons on each side of the disc. They need more design space, are more complex and expensive than floating calipers, but their performance is better. Using e.g. two pistons which are different in size on each side results in a better brake force distribution along the pad area and reduced wear.

Figure 1.4.: Floating brake caliper.

Wheel carrier: The brake caliper is mounted on the wheel carrier. The rotating wheel axle goes through the wheel bearing mounted in the wheel carrier. Additionally, several suspension parts such as steering arm, anti-roll bar, whishbone, spring and damper are mounted at the wheel carrier.

This work focusses on disc brakes with a fixed caliper. This type of brake system is more complex and thus more expensive than floating caliper brakes or drum brakes, but has a better braking performance. Consequently, they are used e.g. in expensive sport cars. However, exactly the customers of such cars are not willing to accept noisy brakes. These things lead to the decision to investigate a disc brake with a fixed caliper.

The majority of the currently used brake systems are based on a transfer of the brake force applied on the brake pedal via brake fluid to the brake system, hence a hydraulic brake system. Because new innovative vehicle concepts are being developed, a separation of brake actuation (brake pedal) and application (actuation of the brakes) becomes necessary. For example, an electric car can brake via recuperation, which is converting kinetic energy into electric energy using an electric generator, or via the hydraulic friction brake, see Fig. 1.5.

Thereby, one common problem is *brake blending*: at low speeds or fully charged batteries the recuperation is inappropriate and the brake system has to change from electrical braking to frictional braking. This transition should be unnoticed by the driver [76, 78, 95, 98, 113].

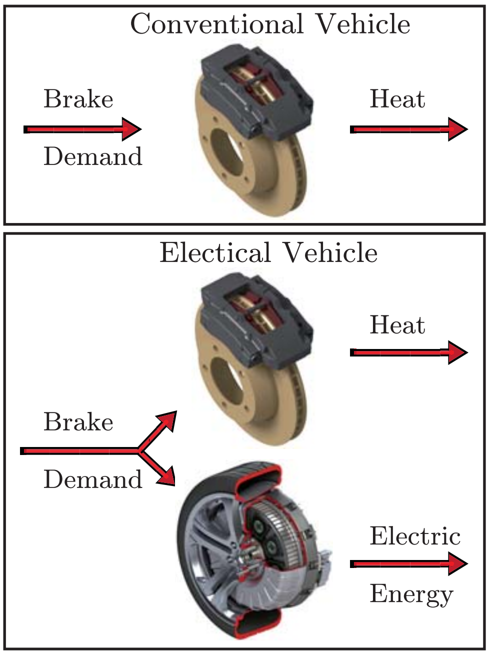

Figure 1.5.: Principal depiction recuperation.

As a consequence, new brake systems are being developed which separate the direct connection between brake pedal and brakes. Solutions range from brake pedal travel simulator to new brake systems based on electrical or electro mechanical actuation as for example developed by *Vienna Engineering* [138, 139, 140].

1.1.2. Vibrations in Brake Systems

In dynamic systems vibrations always may occur. Thereby, Allgaier [14] and Wallaschek et al. [167] provide a brief overview of the different vibration phenomena in brake systems. Figure 1.6 shows a classification of the different vibration types and their frequency range. The acting mechanisms and the resulting vibrations are described in the following:

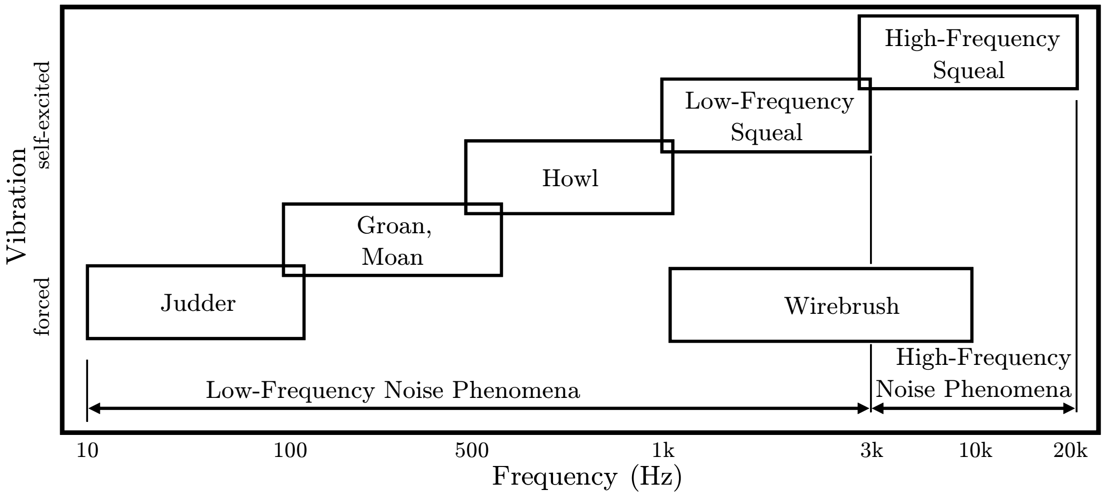

Figure 1.6.: Classification of brake vibrations, adapted from [14, 39, 167].

Forced Vibration: In this case the vibration is forced by an exciting mechanism. For example, an unevenness in the brake disc surface leads to a sinusoidal excitation due to the deflection. The frequency of the excitation depends on the rotational speed, hence on the driving velocity.

Self-Excited Vibration: These vibrations are excited by themselves. Therefore some instability mechanisms are necessary such as varying parameters of the system. One example is the velocity dependent friction coefficient. With decreasing velocity the friction coefficient increases and due to this the friction force increases, which may lead to an unstable system. Additionally, the friction coefficient also depends on the temperature and the applied brake pressure. Another dynamic instability mechanism is *mode-coupling*. This results when two vibrations with similar frequencies are coupled. In general this resulting vibration is unstable.

Judder: Due to inaccuracies in the manufacturing process or thermal stress, the thickness of the brake disc may vary. These *Disc Thickness Variations* (DTV) lead to a forced vibration of the brake system which is velocity and rotational speed dependent. Thereby, the frequency range is from 10 Hz to 100 Hz [25]. In addition to the audible noise, the vibration is also noticeable at the brake pedal and the steering wheel. The influence of the manufacturing process can be minimised using quality specifications. However, the thermal stress may cause the formation of *hot spots* on the disc which results in an uneven disc surface because of unsteady heat distribution. A smoother contact leads to fewer *hot spots* and therefore to fewer problems with brake judder [90].

Groan & Moan: In contrast to Judder these vibration phenomena are independent of the rotational speed and are caused by dynamic instabilities in the brake system. In the frequency range from 100 Hz to 500 Hz vibrations with different tonal components occur. Groan especially occurs when the vehicle stands downhill, the brakes are open gently and the car starts to creep forward slowly [169]. At such low vehicle speeds and brake pressures the brake disc and pad may stick for a brief moment. This results in a stick-slip vibration [46].

Howl: This phenomenon is similar to Groan and Moan but in a higher frequency range from 500 Hz to 1 kHz.

Wirebrush: This is a superposition of different (high) frequency vibrations with varying amplitudes at a frequency range from 1 kHz to 10 kHz. Sometimes it is also called *chirping*, because it sounds like the twittering of birds. Because there is no dominant frequency or vibration, it is very complicated to gain control of this phenomenon.

Low-frequency Squeal: At low speeds and brake pressures the brake system may exhibit an unstable motion. Thereby, the vibration reaches a critical *limit cycle*. The limit cycle is the oscillation cycle at steady state vibration. Thereby, the amplitudes and frequencies reach a constant value. The system squeals at a frequency range from 1 kHz to 3 kHz. Usually the squealing frequency is close to an eigenfrequency of the brake disc. The disc mode shape in that frequency range has usually two to four nodal diameters, and the main vibration is mostly an out-of-plane vibration. Since of the high sensitivity of the human ear in that frequency range, these vibrations are especially disturbing.

High-frequency Squeal: This is similar to low-frequency squeal, but correlated to squeal frequencies from 3 kHz to 20 kHz. At higher frequency, the in-plane vibrations of the disc becomes more important.

1.2. Development Process in Automotive Engineering

The automotive history began more than one hundred years ago. At that time the aim was to replace the horses of coaches by a motor. As a result, people called the first automobiles ”coaches without horses”. At that time the development of motor and coach was separated. Drawings and calculations were done by hand. Also research was strictly problem-orientated and development cycles were based on experiments and testing.

Today’s product development in automotive engineering is driven by a wide range of customers and legislative requirements. The number of model variants increases to fulfil these in part contradicting requirements. Figure 1.7 shows an example of this development. Additionally, the development time of the vehicle has decreased. In the 1960s the development time of a vehicle was approximately seven years. In the meantime a vehicle is developed in about two years [80].

1979	1989	1999	2009
			Polo
			Golf
			Golf Plus
			Golf Variant
			Beetle
			Beetle Cabrio
			Scirocco
		Golf	Jetta
		Golf Variant	Touran
		Golf Cabrio	Tiguan
		Polo	Eos
Golf	Golf	Lupo	Passat
Polo	Polo	Beetle	Passat Variant
Derby	Jetta	Bora	Passat CC
Jetta	Passat	Passat	Sharan
Passat	Scirocco	Passat Variant	Touareg
Scirocco	Corrado	Sharan	Phaeton

Figure 1.7.: Range of car models of Volkswagen AG, German market only [72].

1.2.1. Computer Aided Technologies

To obtain a reduction in the development time, *Computer Aided* (CAx) technologies are useful. Figure 1.8 shows the historical development of these technologies. Up to the 1970s design was made by hand on drawing boards. Thereafter the first commercial programmes for *Computer Aided Design* (CAD) using 2D drawings and 3D wireframe models were implemented. In the meantime it is possible to design 3D solid and surface models in a parametric manner. The whole vehicle design is done on computers. Thereby, collision checks and calculation of clash and assembly procedures are performed using *Digital Mock-Ups* (DMU).

In addition to CAD for functional investigations, *Computer Aided Engineering* (CAE) has also become more important. In former times parts were manually calculated, later simple single-computer supported calculations were performed. Today, the resulting strain and deflection because of mechanical loads on complex parts can be analysed by means of numerical methods. Powerful computing clusters are needed for these tasks.

1.2.2. Full Vehicle Development Process

Figure 1.9 shows the phases of a full vehicle development process. During the whole process virtual and physical development are performed simultaneously. The results of the simulations have to be verified by experiments. The development process has become less experimental and the focus is now more on virtual methods. The final aim is to develop a vehicle only virtually without any experimental testing.

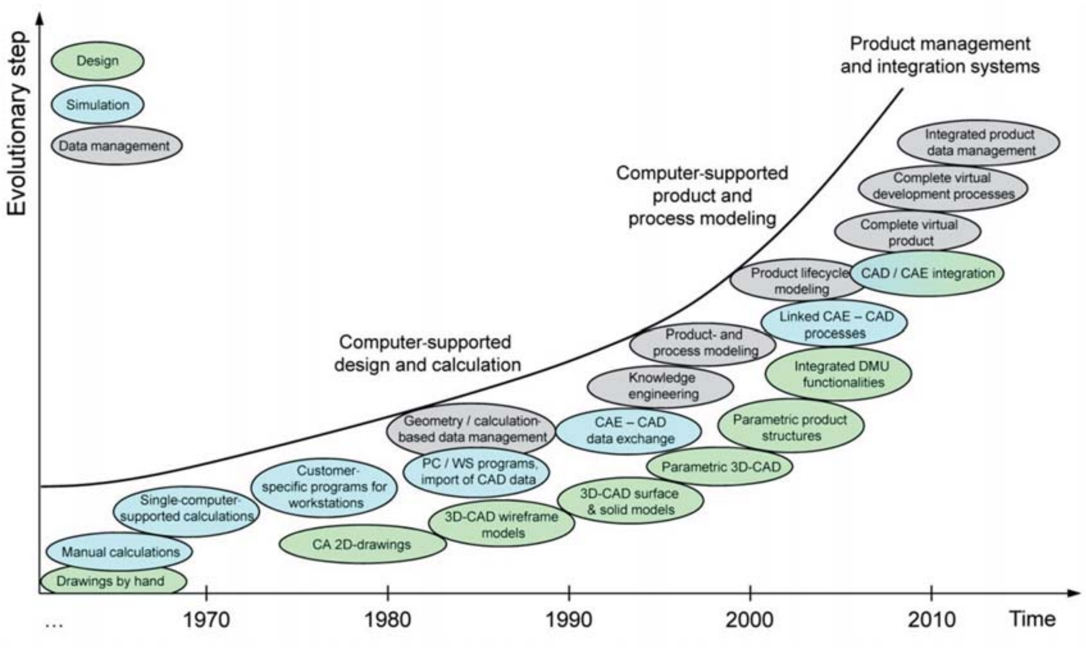

Figure 1.8.: Historical development of CAx technologies [80].

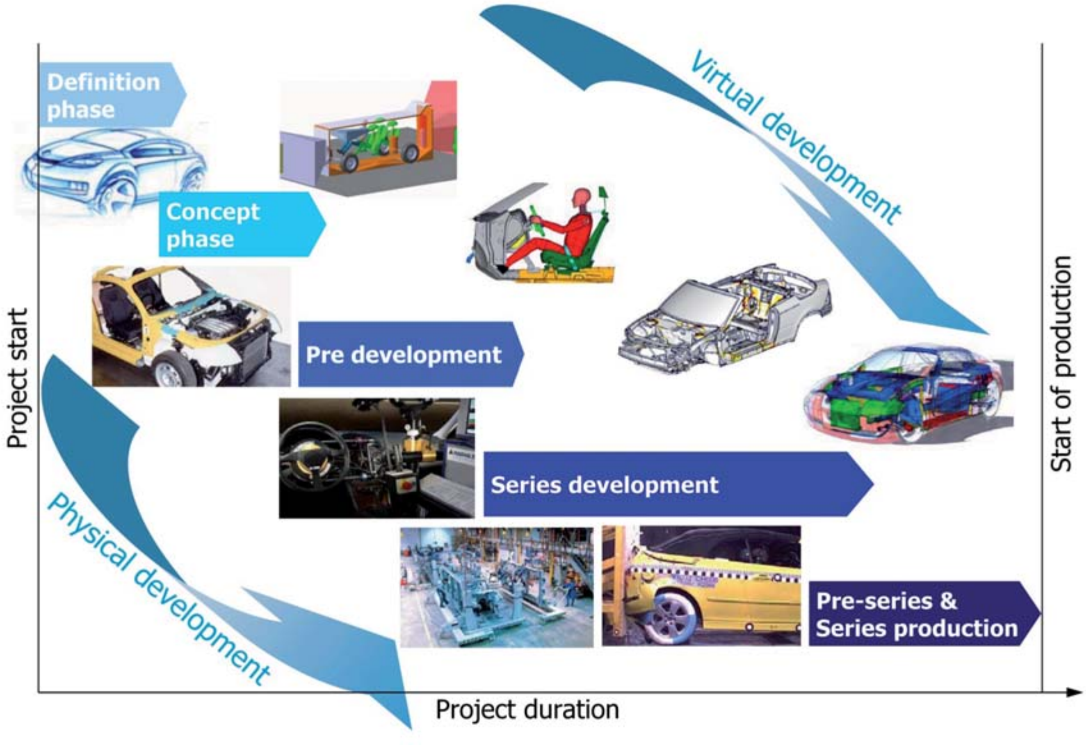

Figure 1.9.: Sample phases of an automotive full vehicle development process [81].

In the definition phase, market research and trend prognoses deliver the requirements during the projected product life cycle. The overall product strategy of the manufacturer as well as the economic situation have to be considered. At the end of the definition phase a *list of requirements* is defined, which includes, for example, target group, dimensions, car classification and first styling guidelines.

In the concept phase a detailed description of the vehicle is worked out. This includes packaging studies, styling, technical and legislative requirements, etc. Thereby, knowledge from former project and research work is taken into consideration. One main task is the styling. Stylists are faced with different boundaries resulting from technology, but also market and fashion trends. In addition, brand characteristics have to be taken into account. To assist the stylists, benchmark studies are performed to subsequent achieve a successful market placement. Next to the styling technical characteristics are also taken into account.

Another task is the consideration of new technologies. Different propulsion types, such as electrical or hybrid drives, have to be examined. Also the development of new vehicle concepts (e.g. low emission city vehicle) will be discussed and determined in this phase. Nevertheless, all the considered new technologies have to be checked against the previously defined requirements. Finally, a feasibility study is performed and the functional concept is defined. At this time the new technologies need to have been approved for their principal usability.

In the pre-development phase, the chosen technologies and styling are designed and optimised, which includes a detailed definition of the vehicle layout and packaging studies. If possible, existing vehicle platforms are used and existing modules are evaluated regarding their suitability for the new vehicle. In this phase, the new vehicle has to be prepared to fulfil all legislative requirements. Additionally, the design space for brake systems is specified, which is rather important for the brake development. The specification of the whole vehicle leads to a full vehicle concept.

This specification is adjusted in consultation with the different development departments. Therefore, several steps or development cycles are necessary. At the end of this phase, a final styling concept is chosen and verified, which has to fulfill all engineering based requirements. The verification of the virtual development is supported by hardware tests of components. The functionality is tested using prototype vehicles. The final styling concept is freezed. No modifications are allowed from this time on, because the impact on subsequent engineering tasks would be significant.

The series development phase focuses on the manufacturing development. Interfaces between parts or system suppliers are defined. All developments are also performed in close cooperation with the production engineering. Highly accurate models at a high detailed level are used to design the manufacturing process of the vehicle. At the end of this phase, the complete product is developed, including its production, the supplier integration and the quality management. Important milestones, which are carried out during series development, are the *styling freeze* and the *design freeze*.

The last phase includes the pre-series and series production. The pre-series production is used to check the manufacturing process and to train employees. For *homologation*[1] of the vehicles pre-series vehicles are usually used. The different phases do not always occur consecutively. There is always an overlap between the phases [80].

1.2.3. NVH in Brake System Development

The design of the brake system is influenced among others by packaging, costs, durability and the possibility to use *Carry-Over Parts* (COP). One important parameter is the targeted braking performance. This parameter is mainly influenced by the vehicle mass and the engine power. These two parameters are already roughly known at the beginning of the concept phase and they determine the necessary maximum braking power, Equ. (1.5). For the brake design thermal simulations are mainly performed [159], but also the acoustical behaviour is studied by means of numerical methods.

To avoid NVH issues, the natural modes of the brake system parts are investigated. Through modifications of the parts, these natural modes can be shifted in order to avoid mode-coupling in advance. Nevertheless, acoustical problems in brake systems are usually identified lately in the development process. Typically they are detected with the first prototype vehicle. At this stage the suspension parts are already optimised regarding vehicle dynamics and driving comfort. Due to this, possibilities for modifications are quite limited.

To solve the problem, a close collaboration between simulations and experiments is necessary. Simulations tend to overestimate the number of possible instabilities, see Chap. 3 for a detailed explanation. The relevant ones have to be determined using experimental methods. Once the relevant critical instabilities are known, simulations can be performed to find out how these unstable vibrations can be avoided.

Marschner [107] introduced two terms to describe the characteristic outputs of these two approaches: simulations using *Complex Eigenvalue Analysis* (CEA) deliver the *Ability* of the system to vibrate owing to self-excitation. The problem here is that the result of the simulations delivers the amplification rate of the instable states, but not their reached limit cycle amplitude which equals the emitted noise.

As a result, instabilities with high amplification rates are identified as critical, but they need not be critical at all because of a low limit cycle amplitude. In contrast, the experiments on the test bench show the *Behavior* of the system at real-world conditions and the limit cycles of the unstable states are determined. Therefore, both approaches are important and necessary to develop a quiet brake system.

---

[1] Check of an official authority that the car fulfils the legislative requirements and is allowed to be sold.

The present thesis aims to present a proposed development process for brake systems regarding NVH. However, in order to provide a proper dimensioning regarding braking performance of a brake system several issues have to be considered. One basic requirement is that the car always remains stable during braking. Braking stability must not depend on vehicle load, tyres, braking demand or road conditions. Additionally, unwanted movements of the vehicle have to be limited automatically.

In fact neither driving errors nor disturbances of any kind are allowed to result in unwanted vehicle movements. This means that during braking the vehicle may slide forward, but the tail is not allowed to break away. In addition, the vehicle should be easily controllable as long as no wheel locks. As a result, the vehicle shall react accurately to steering movements and remain stable. The method for brake system dimensioning concerning the braking performance is not in the focus of this work, anyway it is discussed in the Appendix, Chap. A.1.

1.3. State of the Art

There are different approaches to solve the issue of brake squeal. The academic approach is to investigate the basic mechanisms which can exhibit self-induced vibrations using analytical models. Therefore, in the majority of cases rather simple minimal models with only a few *degrees of freedom* (DoF) are developed. The industrial approach uses the power of computational calculations using the nonlinear *Finite Element Method* (FEM) and very detailed models with a huge number of DoF.

Additionally experiments are performed. Thereby, tests on small tribometer test rigs up to full vehicle test benches and even road testing with prototypes are performed. In the following section the different approaches as well as their advantages and disadvantages will be explained briefly. For more detailed information see comprehensive reviews such as [31, 34, 94, 133].

1.3.1. Analytical Approach

The friction force in the brake pad and brake disc contact may lead to self-excited vibrations and furthermore to a dynamic instability in the brake system. As a result, the brake system starts to vibrate and to squeal. Thereby, the vibration reaches a limit cycle, whereby a higher limit cycle indicates a noisier brake. There are several accepted scientific theories about mechanisms, which cause the brake system to become unstable. These mechanisms are simulated using simplified minimal models. However, not all of the models are proven by experiments [164].

One of the most commonly accepted squeal mechanism is the change of the friction coefficient with respect to the sliding speed. Thereby, a negative slope of the friction coefficient, increasing friction coefficient at decreasing speeds, leads to self excited vibrations. This characteristic could be proven in experiments. Nevertheless, squeal can also occur with a constant friction value. For example, mode-coupling instability may occur at constant friction coefficients. Here, vibrations are coupled in two different directions.

Another mechanism is the flutter instability, which is originally a dynamic aeroelasticity term. One famous example for flutter instability is the collapse of the *Tacoma Narrows Bridge* in the year 1940. Thereby, several DoF of the bridge were coupled, driven by the (almost) constant light wind. Since brake squeal also occurs at a constant friction coefficient some research is focused on this. Von Wagner et al. [164] claim that flutter instability is the realistic cause of brake squeal in most cases.

The main advantage of the minimal models is that they are useful to gain a basic understanding of the elementary excitation mechanism. Brakes modelled as FEM models or multibody systems have usually a high number of DoF. To obtain a basic insight into the brake squeal phenomenon, the minimal models are more convenient. Thus, it could be much easier to investigate excitation mechanism and the influence of different parameters of the system. Nevertheless, the association of simple minimal models to automotive disc brakes is hardly possible.

1.3.2. Finite Element Method

In the last decades computation power and simulation methods have increased rapidly. Because of the friction in the contact, the main simulation method for brake squeal is the *Complex Eigenvalue Analysis* (CEA). The advantage of the FEM is that usually a model of the brake system already exists which is used for performance (temperature) or strength calculation. Thus, the effort for the modelling is kept within limits. The complex eigenvalues describe the frequencies and the actual damping values at the complex modes. If the damping value is negative, the system may become unstable.

Unfortunately the FEM estimates in general to many critical points [32, 101, 103, 133]. Additionally, there are several parameters, especially material properties, which are difficult to measure or even have to be estimated. Furthermore, wear changes among other factors the contact between disc and pad [7, 9, 10]. These complex mechanisms need to be simplified and linearised for the CEA simulation. Such inaccuracies may lead to additional instabilities which do not exist in reality [26]. Therefore, the simulation results have always to be verified and validated with experimental results.

As a consequence of this, much work is spent on better material properties measurements and estimations [64, 89, 144, 170]. Additionally, the implementation in the simulation of viscoelastic material, such as the brake pad material, and its damping effects are the focus of several research studies [35, 160]. In the meantime also the effect of a temperature depending friction coefficient is taken into account [5, 6].

1.3.3. Experimental Approach

There are several possibilities to investigate brake squeal experimentally. On the one hand matrix tests on test benches are performed, such as the recommended standard of the *Society of Automotive Engineers* (SAE), called *"Disc and Drum Brake Dynamometer Squeal Noise Matrix"*, SAE J2521 test procedure [143]. The complete test consists of 2321 brake applications at different brake pressures, velocities, temperatures of brake pad and disc and rotating directions. As a result, a *Squeal Noise Matrix* (SNM) is obtained which delivers critical operation points and their absolute and relative frequencies. In addition to this, road testing is also necessary in order to obtain reliable results.

In addition, in-depth investigations on test benches can be carried out. For example, parameter studies of brake discs and brake pads are performed [46]. Some research also focuses on *beam on disc* set-ups. There the brake pads are replaced by a single beam which presses against the disc. Thus it is easier to test and reproduce results of similar analytical models [15, 109, 110, 161].

An extended double pin-disc model, based on a pin-disc model [123], has also been developed and compared with the results of an experimental rig. In the model and on the test rig the effects of parameter variations such as brake disc stiffness or brake pad damping are investigated [47]. Ramasami et al. [141] developed a simplified disc brake system including a U-shape fixed caliper and two round pads. Due to the simplified pad shape this model equals almost the double pin-disc model.

1.3.4. Innovations

The accuracy of simulations depends on a proper modelling of the brake system components and knowledge of the relevant acting physical mechanisms. As mentioned above, much research is being conducted on the material properties of brake pads, but also the friction contact is important. Eriksson et al. [49, 50, 51] investigated the influences of humidity and changed contact surfaces on squeal generation. For this a brake disc was grit-blasted or the surface of the brake pads was changed by a variable number of bores. These tests were performed on a simplified laboratory test rig. Also other investigations are carried out on simplified small test rigs, such as [13, 68, 83].

For the present work the combined brake and suspension test rig of the *Institute of Automotive Engineering* is available for in-depth investigation. Thereby, a complete vehicle axle including the suspension parts can be mounted on the rack which has the same connection points as the suspension has to the car body in reality. The axle can also be preloaded to obtain the so-called "K_0" position, which indicates the static deflection of the suspension due to the vehicle's weight.

This kind of test method is standard for industrial acoustical testing of brake systems. There, in most cases only one microphone is used as prescribed in the SAE J2521 standard, which is the performed test method. High frequency vibrations above 2 kHz are observed to be critical. At these frequencies the vibrations of brake disc and/or the brake pad and/or the caliper are coupled. Nevertheless, it is important to test the whole suspension because it also influences the acoustical behaviour. Kruse et al. [96] highlight this importance using a model of a simplified nine DoF oscillator on a conveyor belt.

Consequently, there is a gap between the simplified test rigs used for research and the test method using the complete vehicle axle in industry. This work aims at the presentation of basic considerations on analytical models, investigations of a FEM model and the development of a complex measuring system which shall be implemented on a full suspension test rig. The research question is whether, if by means of simulations and reproducible measurements the influence of the different instability mechanisms can be determined and how the system has to be changed in order to inhibit friction induced vibrations. Hence, how does friction influence vibration and vice versa?

Therefore, a measuring device is necessary which measures the friction force as closely as possible to the contact area of brake pad and disc. This is indented by developing a sensor which measures the friction force in a very high resolution up to a very high limit frequency. As a result, further information regarding mechanisms in the contact area is expected.

Using a complex measurement system, sensitivity analysis can be performed. Thus, the influence of different counter-measures are may evaluated. Nevertheless, it has to be mentioned that no general statements regarding the usability of the different counter-measures can be made, because only one brake system will be tested. However, the second aim is to evaluate the usage of different sensors and sensor positions, hence what kind of sensor at which position delivers practicable results for future investigations on other brake systems. Therefore, contact-free measuring *Eddy Current Sensors* (ECS) will be tested as well as the suitability of strain gauges.

2. Analytical Minimal Models

2.1. Introduction

There are numerous publications which deal with modelling of disc brake squeal. They all have in common that brake squeal is initiated by an instability due to the friction force which leads to a self-excited vibration of the brake system. The oscillating system reaches a certain limit cycle, which is the oscillation cycle at steady state vibration. Thereby, the amplitudes and frequencies reach a constant value. The size of the limit cycle amplitude correlates with the squeal sound intensity.

There are different explanations for the onset of instability. Recent publications demonstrate that non-conservative friction forces are responsible for the instability. To illustrate the different mechanisms, several minimal models are used. Minimal models usually look quite different to an automotive disc brake. Due to this, a direct transferability of the results is hardly possible. Nevertheless they are useful to gain a basic understanding of the acting instability mechanism [164].

In the models, friction is usually responsible for the excitation or for the coupling of two vibrations. A good overview of the different dynamic friction laws and their impact on friction induced vibrations is given by Awrejcewicz and Olejnik [17] and by Ostermeyer [126]. Figure 2.1 shows the principle appearance of the most common friction laws. Already in 1785 Coulomb [38] proved that there is a difference between static and sliding friction coefficient. He also claimed that the sliding friction coefficient is independent of the velocity. For most technical problems, this assumption is accurate enough.

Nevertheless, some experiments show that there is a negative gradient of the friction coefficient with respect to relative velocity v_{rel} between a brake pad and disc. Such a linear approach is suggested by e.g. Shin et al. [149]. Ostermeyer [125] presented a more complex non-linear semi-physical friction law. It is defined as

$$\mu = \frac{0.4}{\pi} \arctan(200 \cdot v_{\mathrm{rel}}) \left(\frac{1}{|v_{\mathrm{rel}}| + 1} + 1 \right) , \tag{2.1}$$

where μ denotes the friction coefficient depending on the relative velocity v_{rel}. The main advantage of this law is that it is a continuous function and no distinction of cases is necessary. However, this continuous regularisation of the friction delivers no friction force for $v_{\mathrm{rel}} = 0$.

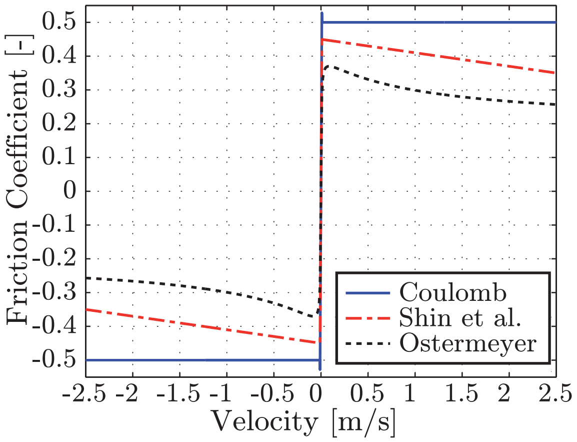

Figure 2.1.: Three different laws of friction, schematic diagram adapted from [38, 125, 149].

2.2. Investigated Minimal Models

2.2.1. Stick-Slip

Figure 2.2 shows the simplest model to describe brake squeal, which is a single-*Degree of Freedom* (DoF) system on a conveyor belt. Thereby, a mass is supported by a spring with a spring rate k and a damper with a damping rate d. As long as the mass sticks on the conveyor belt the mass moves with the same velocity ($v_x = \dot{x}$) as the conveyor belt, $\dot{x} = v_C$. At a certain point, the reaction forces of the spring-damper element are greater than the static friction and the mass starts to slide.

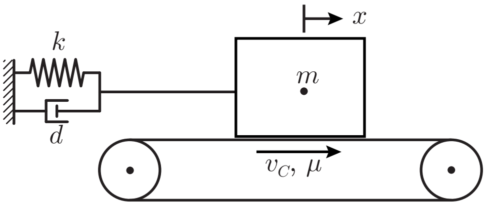

Figure 2.2.: Minimal model for stick-slip.

Considering the Coulomb law of friction, the sliding friction coefficient μ_{sl} is smaller than the static friction coefficient μ_{st}. In the model $\mu_{\text{sl}} = 0.8\mu_{\text{st}}$ is considered. The relative velocity is given by

$$v_{\text{rel}} = v_C - \dot{x}. \tag{2.2}$$

The mass slides as long as the relative velocity is not equal to zero. Hence, two motion states *sliding* and *sticking* are possible which results in the following equations of motions:

Sliding:

$$\ddot{x} + \frac{d}{m}\dot{x} + \frac{k}{m}x = -g \cdot \mu_{\mathrm{sl}} \cdot \operatorname{sign}(v_{\mathrm{rel}}), \tag{2.3}$$

Sticking:

$$\dot{x} = v_C \quad \text{if } m \cdot g \cdot \mu_{\mathrm{st}} \leq |d \cdot \dot{x} + k \cdot x|. \tag{2.4}$$

Depending on the initial conditions of displacement x_0 and velocity $\dot{x}_0$, two different paths of motion for the mass are possible:

1. If the system starts near the equilibrium point for the sliding conditions, the motion is stable and tends to the equilibrium point. Finally the mass reaches the equilibrium point and stops moving. Figure 2.3 shows on the left the curves of displacement and velocity versus time. It can be seen that the vibration fades away due to damping.

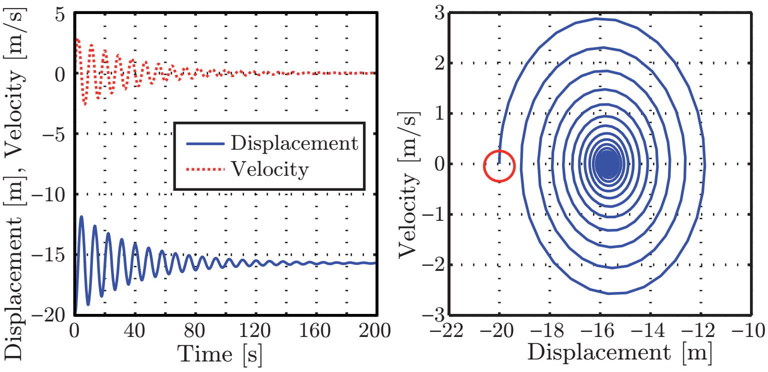

Figure 2.3.: Stable movement of minimal model shown in Fig. 2.2.

The right side of Fig. 2.3 presents the phase portrait of this vibration. The starting point (initial condition) is marked with a red circle. Oscillations in the phase portrait always run in a clockwise direction. At the starting point the mass has its maximum negative x-value. To reduce this value, a positive velocity is necessary. The same applies for the turning point of the velocity. After reaching the maximum velocity, the velocity is still positive and the positive displacement must increase.

2. Figure 2.4 shows the result for a different displacement as initial condition. All other parameters of the model remained the same. Looking at the phase portrait (right) it can be seen that the system gets excited and the vibration reaches a certain limit cycle. The left side shows the classical sawtooth shape of this vibration type, which results because of the constant change between stick and slip.

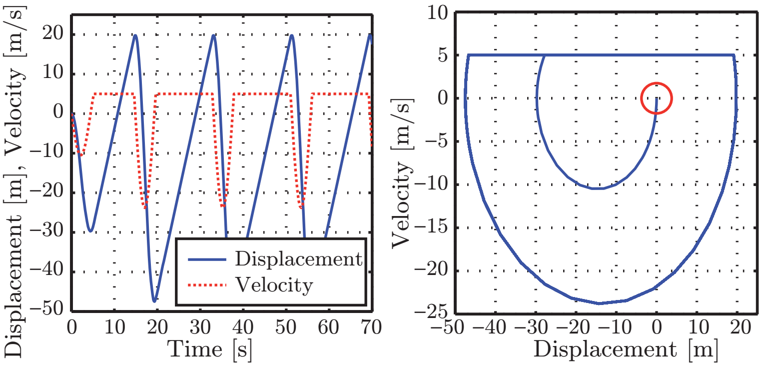

Figure 2.4.: Unstable movement of minimal model shown in Fig. 2.2.

2.2.2. Negative Friction-Velocity Slope

In 1938 Mills [115] performed several investigations on a drum brake. He observed that the friction coefficient is a decreasing function of the sliding velocity for squealing combinations of drum brake and brake lining. A similar conclusion with regard to all automotive brake systems can be found in the paper by Sinclair in 1955 [150]. In 1961 Fosberry and Holubecki [65] concluded that:

> *"Disc-brake squeal has the characteristic of a frictional vibration of the type which can be induced by a frictional pair having either a static coefficient of friction higher than the dynamic coefficient, or a dynamic coefficient which decreases with increase of speed."* [65]

Figure 2.5 shows the minimal model by Shin et al. [149], which applies this school of thought to explain the instability. The model consists of the two single-DoF systems representing the pad (index p) and the disc (index d). Thereby, mass m, damping rate d and spring rate k are taken into account. The coupling between the two systems is modelled through a friction interface, which is pre-stressed by the force F_N representing the brake pressure. The resulting friction force F_F reads

$$F_F = F_N \cdot \mu(v_{\mathrm{rel}}). \tag{2.5}$$

The given relative (sliding) velocity v_{rel} depends on the initial velocity v_0 (rotation speed of the disc) and the current velocities of pad and disc, see Fig. 2.6. Additionally, the friction coefficient μ has a decreasing characteristic with increasing relative velocities due to a factor b. The maximum value is at $v_{\mathrm{rel}} = 0$ which equals the static friction μ_{st}. The resulting equation of motion is given by

$$\underbrace{\begin{bmatrix} m_p & 0 \\ 0 & m_d \end{bmatrix}}_{\mathbf{M}} \underbrace{\begin{bmatrix} \ddot{x}_p \\ \ddot{x}_d \end{bmatrix}}_{\ddot{\mathbf{z}}} + \underbrace{\begin{bmatrix} d_p - F_N b & F_N b \\ F_N b & d_d - F_N b \end{bmatrix}}_{\mathbf{D}} \underbrace{\begin{bmatrix} \dot{x}_p \\ \dot{x}_d \end{bmatrix}}_{\dot{\mathbf{z}}} + \underbrace{\begin{bmatrix} k_p & 0 \\ 0 & k_d \end{bmatrix}}_{\mathbf{K}} \underbrace{\begin{bmatrix} x_p \\ x_d \end{bmatrix}}_{\mathbf{z}} = \underbrace{\begin{bmatrix} F_N(\mu_{\mathrm{st}} - b v_0) \\ -F_N(\mu_{\mathrm{st}} - b v_0) \end{bmatrix}}_{\mathbf{0}}, \tag{2.6}$$

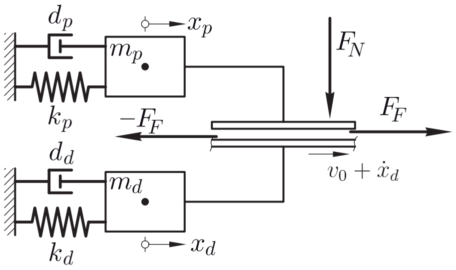

Figure 2.5.: Minimal model by Shin et al. [149].

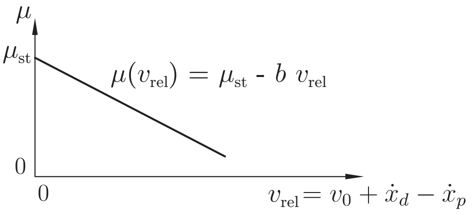

Figure 2.6.: Friction characteristic of minimal model and by Shin et al. [149].

where $\mathbf{M}$, $\mathbf{D}$ and $\mathbf{K}$ denote the mass, damping and the stiffness matrix of the system. The position vector is given by $\mathbf{z}$. For stability analysis only the homogeneous solution is investigated. Using the trial function $\mathbf{z} = \mathbf{z}_0 \cdot e^{\lambda t}$ results in the characteristic equation:

$$\det \begin{bmatrix} \lambda^2 + \lambda \dfrac{d_p - F_N b}{m_p} + \dfrac{k_p}{m_p} & \dfrac{F_N b}{m_p} \\ \dfrac{F_N b}{m_d} & \lambda^2 + \lambda \dfrac{d_d - F_N b}{m_d} + \dfrac{k_d}{m_d} \end{bmatrix} = 0, \tag{2.7}$$

where λ denotes the eigenvalues of the system. The resulting fourth order characteristic polynomial in general form reads

$$\lambda^4 + a_1 \lambda^3 + a_2 \lambda^2 + a_3 \lambda + a_4 = 0, \tag{2.8}$$

where a_i denote the polynomial coefficients. Regarding the Routh-Hurwitz criterion, see e.g. [88, 136], the conditions for instability are given by

$$\begin{gathered} a_1 < 0, \text{ or } a_2 < 0, \text{ or } a_3 < 0, \text{ or } a_4 < 0, \text{ or } a_1 a_2 - a_3 < 0, \\ \text{or } a_1 a_2 a_3 - a_1^2 a_4 - a_3^2 < 0. \end{gathered} \tag{2.9}$$

Thus, it is possible to determine stability charts of this minimal model. Solving the characteristic polynomial given by Equ. (2.8) results in several eigenvalues of the form given by

$$\lambda_i = \delta_i \pm \mathrm{i}\omega_i, \tag{2.10}$$

where α and ω indicates the real part and the imaginary part of the eigenvalue λ. An instability, hence negative damping which may lead to a self-excited vibration of the system, is determined by a positive real part. The imaginary part equals the eigenfrequency [149, 164].

2.2.3. Mode-Coupling

Figure 2.7 shows another minimal model published by Hoffmann et al. [85]. Using this model, the physical mechanisms can be clarified which lead to *mode-coupling* instabilities. In this model a decreasing friction coefficient with increasing speed is not necessary to obtain instabilities. Again, similarities to a disc brake system are hardly recognisable.

The model consists of a conveyor belt with a constant velocity v_C, which may be interpreted as a rotating brake disc. A block with the mass m is in contact with this conveyor belt. The contact stiffness is represented by the linear spring k_3. In addition, the block is suspended by linear springs with the spring rates k_1 and k_2 at angles β_1 and β_2. This may be interpreted as the brake pad with a contact stiffness which is suspended by the brake caliper. The resulting contact force F_N reads

$$F_N = -k_3 y. \tag{2.11}$$

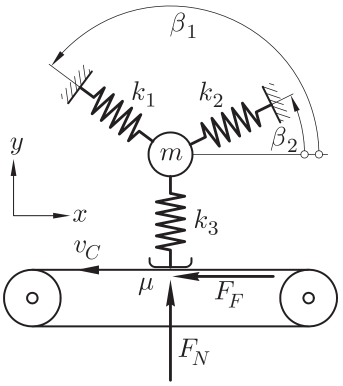

Figure 2.7.: Minimal model by Hoffmann et al. [85].

The friction force F_F is modelled as a Coulomb-type friction with constant friction coefficient μ. Considering a steady sliding state with neither change of sign of the relative velocity nor zero-crossing, F_F depends only on the vertical movement y of the block m and is given by

$$F_F = -\mu k_3 y. \tag{2.12}$$

The resulting equation of motion reads

$$\underbrace{\begin{bmatrix} m & 0 \\ 0 & m \end{bmatrix}}_{\mathbf{M}} \underbrace{\begin{bmatrix} \ddot{x} \\ \ddot{y} \end{bmatrix}}_{\ddot{\mathbf{z}}} + \underbrace{\begin{bmatrix} k_{11} & k_{12} - \mu k_3 \\ k_{21} & k_{22} \end{bmatrix}}_{\mathbf{K}} \underbrace{\begin{bmatrix} x \\ y \end{bmatrix}}_{\mathbf{z}} = \underbrace{\begin{bmatrix} 0 \\ 0 \end{bmatrix}}_{\mathbf{0}}, \tag{2.13}$$

where the coefficients k_{ij} are specified as

$$k_{11} = k_1 \cos^2 \beta_1 + k_2 \cos^2 \beta_2, \tag{2.14}$$

$$k_{12} = k_{21} = k_1 \sin \beta_1 \cos \beta_1 + k_2 \sin \beta_2 \cos \beta_2, \tag{2.15}$$

$$k_{22} = k_1 \sin^2 \beta_1 + k_2 \sin^2 \beta_2 + k_3. \tag{2.16}$$

Now again the complex eigenvalues of the system can be calculated. In contrast to the previously presented model, the non-symmetric components are now in the stiffness matrix **K**. Hoffmann et al. [85] also discussed the work W of the non-conservative friction force F_F. During one cycle displacement, the work is given by

$$W = \oint F_F \mathrm{d}x. \tag{2.17}$$

To obtain a non-zero energy gain, two conditions have to be fulfilled. Firstly, non-zero cyclic changes in the friction force F_F and in the corresponding vibration in x-direction are necessary. Secondly, there has to be a phase shift between the time dependency of the friction force and the corresponding vibrations: both are harmonic and the net energy transfer would therefore vanish without it. Hoffmann and Gaul [86] present a extension of this model which additionally includes damping.

Figure 2.8 depicts this model. The sliding mass m on the conveyor belt is suspended by two springs with the spring rates k_x and k_1 and by two dampers with the damping rates d_x and d_y. The spring k_y represents the contact stiffness. In this model, the coupling between the horizontal motion x and the vertical motion y is only due to the spring k_1.

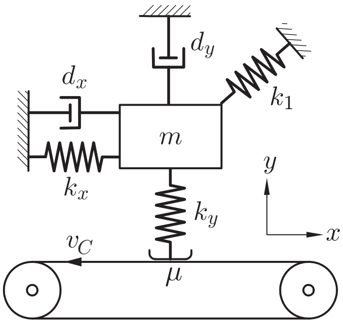

Figure 2.8.: Minimal model by Hoffmann and Gaul [86].

In all these models the influence of friction is modelled as friction-loaded spring. This kind of modelling is often used for contact formulations including frictional effects in minimal models or in FEM models. Thereby, friction is incorporated through a geometric coupling. Figure 2.9 shows such a spring that connects a pair of nodes of e.g. brake disc and the brake pad. In the figure, u_i and v_i indicate the displacement of the nodes in normal and tangential direction, F_{Ni} and F_{Fi} the corresponding forces. The forces are coupled due to the friction coefficient μ: $F_{Fi} = \mu F_{Ni}$ [101, 119, 130, 133].

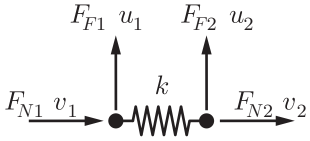

Figure 2.9.: Geometric coupling, adapted from [132].

An extension of the model by Hoffmann and Gaul [86] is presented by Kruse et al. [96, 97]. Experiments showed that there is an influence of the vehicle suspension parts on the squeal occurrence. Hence, the boundary conditions of the brake system influence the reachable limit cycle during squeal. The same brake system (brake disc, pad and caliper) mounted in two different vehicles may lead to significantly different results regarding the squeal occurrence.

Figure 2.10 shows the extended model to describe this influence [97]. Thereby, the sliding mass on the conveyor belt is suspended by a chain of masses connected by springs and dampers. This chain represents the influence of the suspension. Beside the calculation of the complex eigenvalues, a limit cycle approximation using the *Constrained Harmonic Balance Method*, which is introduced by Coudeyras et al. [36, 37], is also presented in that work.

2.2.4. Flutter Instability

Brake squeal may also be described as a result of *flutter instability*. This kind of instability is also sometimes defined as *binary flutter* or *Hopf bifurcation* and was originally observed at aircraft wings. Thereby, the energy is exchanged between two modes of vibration in a manner, that additional energy is feed into the system.

The size and direction of action of the contact forces depends on the deformation of the parts in contact. That is why these forces are also called *follower forces*. The first minimal model which discussed this effect was presented by North [123] in 1976. A quite similar model, which may be interpreted as the extension of North's model, is presented by Popp et al. [137]. Figure 2.11 shows this minimal model.

In this model the brake disc is represented by a beam with a certain mass m and a moment of inertia J^c. The beam is supported by springs and dampers in vertical and

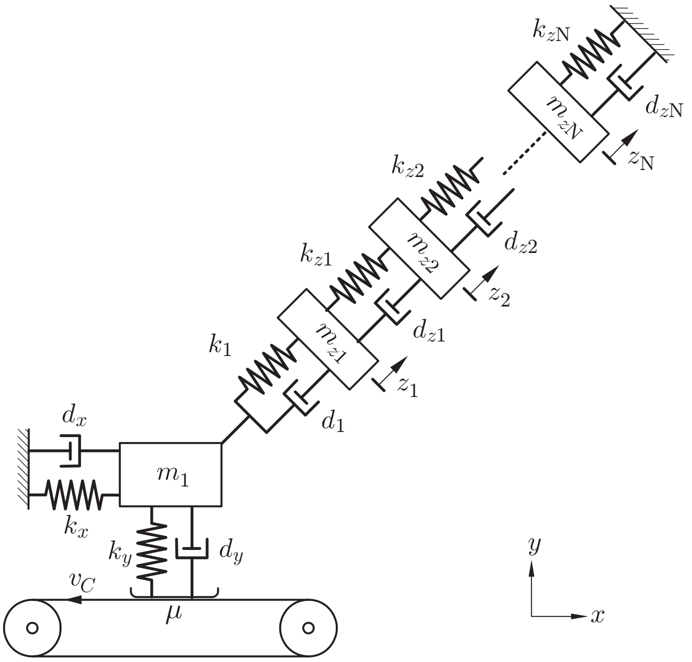

Figure 2.10.: Minimal model by Kruse et al. [97].

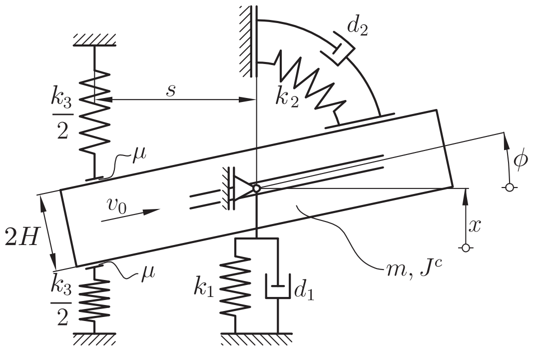

Figure 2.11.: Minimal model by Popp et al. [137].

rotational direction (k_1, k_2, d_1, d_2). At a certain distance s the beam is sandwiched of the two springs which represent the brake pads with the (contact) stiffness $k_3/2$. There is a steady sliding condition with a sliding velocity v_0 and a constant friction coefficient μ is assumed. Using the generalised coordinates x and ϕ, the equation of motion reads

$$\begin{bmatrix} m & 0 \\ 0 & J^c \end{bmatrix} \begin{bmatrix} \ddot{x} \\ \ddot{\phi} \end{bmatrix} + \begin{bmatrix} d_1 & 0 \\ 0 & d_2 \end{bmatrix} \begin{bmatrix} \dot{x} \\ \dot{\phi} \end{bmatrix} + \begin{bmatrix} k_1 + k_3 & -k_3 s \\ -k_3(s - \mu H) & k_2 + k_3(s^2 - \mu H s) \end{bmatrix} \begin{bmatrix} x \\ \phi \end{bmatrix} = \begin{bmatrix} 0 \\ 0 \end{bmatrix}. \tag{2.18}$$

Additionally, the pads are preloaded by the force F_{N0}, thus the brake pads always stay in contact. Consequently, the expanded equation of motion is given by

$$\begin{aligned}&\begin{bmatrix} m & 0 \\ 0 & J^c \end{bmatrix}\begin{bmatrix}\ddot{x}\\ \ddot{\phi}\end{bmatrix} + \begin{bmatrix} d_1 & 0\\ 0 & d_2\end{bmatrix}\begin{bmatrix}\dot{x}\\ \dot{\phi}\end{bmatrix}\\ &+ \begin{bmatrix} k_1+k_3 & -k_3 s \\ -k_3(s-\mu H) & k_2 + k_3(s^2-\mu H s) + 2F_{N0}(H(1+\mu^2)+\mu s)\end{bmatrix}\begin{bmatrix}x\\ \phi\end{bmatrix} = \begin{bmatrix}0\\0\end{bmatrix}.\end{aligned} \tag{2.19}$$

Now this model includes the effect of a preload due to the ϕ-proportional term. Furthermore, this model already looks more similar to an automotive disc brake than the previously explained models. A very similar model, which also models the disc as a beam, is presented by Flint and Hulten [63]. In their paper the influence of the lining deformation is investigated.

2.2.5. Sprag-Slip

Sprag-slip can usually be observed at pin-on-disc test set-ups. The pin is pressed at a certain inclination against the rotation direction of a rotating disc and, due to the friction, the pin deforms until the reacting force of the deformation exceeds the friction force. At that moment the pin slips along the surface and relaxes. Figure 2.12 shows such a sprag-slip model presented by [137], where a torsional spring-damper (k_2, d_2) element is used to model the deformation of the pin. The system has got two DoFs, the vertical motion y of the block mass m_1 and the rotational motion ϕ of the pin m_2. The block mass is suspended by a spring k_1 and a damper d_2 in vertical direction. The pin has the mass m_2, the length L_2 and the moment of inertia J with respect to the centre of mass of the pin.

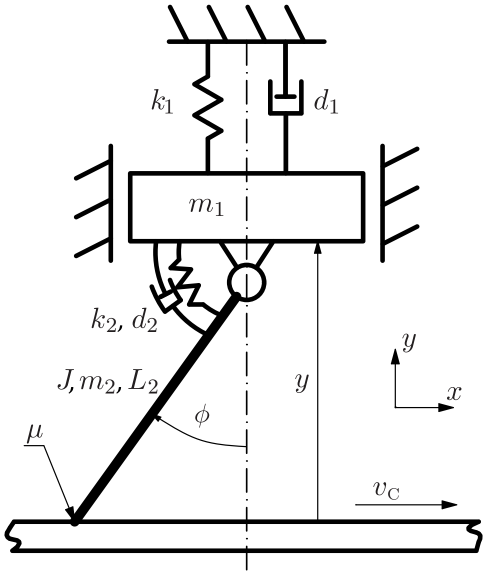

Figure 2.12.: Sprag-slip model adapted from [137].

Popp et al. [137] used this model to explain chatter of chalk on a blackboard. This model provides further insight into vibrations caused by shear deformations. With the help of this approach, it is easy to observe that the drawn line consists of unconnected dots. The reason for that is that two motions are possible: spraging and relaxing. Firstly, the pin locks to the conveyor belt and the contact point moves with the same velocity as the conveyor belt. There is a non-zero contact force and the pin deforms in order to allow its tip to stay on the contact point. Secondly, due to the ongoing deformation, the contact normal force decreases until it vanishes. In this moment, the friction force becomes zero, lift off takes place and the pin relaxes.

The relaxing of the pin is due to the spring k_2. After the relaxing, the pin once again contacts the conveyor belt and locks again. Because of the locking mechanism, the height of the lift off depends on the velocity of the conveyor belt v_C. An increasing velocity leads to a longer time period and extends the limit cycle. It has to be noted that this model should only investigate the effects of sprag-slip, since neither friction coefficient nor sliding on the surface is taken into account.

A similar model is also presented by Hoffmann and Gaul [87]. In their model only the mass of the pin is taken into account, which is elastically suspended in axial direction and clamped in transversal direction. Instead of a rotational spring, the bending-induced displacement of the pin is taken into account.

2.2.6. Expanded Sprag-Slip Model

Experiments carried out within the present research, see Chap. 5, show that the vibrations of the pad at the leading edge are significantly higher than at the trailing edge[1]. This can be explained by sprag-slip effects at the leading edge. Therefore, the sprag-slip model by Popp et al. [137] is expanded with a more realistic friction law adopted from Ostermeyer [125]. The friction coefficient μ is defined as

$$\mu = \frac{0.4}{\pi} \cdot \arctan(20000 \cdot v_{\mathrm{rel}}) \left(\frac{1}{|v_{\mathrm{rel}}| + 1} + 1 \right) \quad \text{with: } v_{\mathrm{rel}} = v_C + L_2 \dot{\phi} \cos(\phi), \tag{2.20}$$

where v_{rel} depends on the velocity of the conveyor belt v_C and the position ϕ of the pin . Additionally, three states of motion are possible now: free motion without contact of the pin, sliding of the pin on the conveyor belt and locking to the conveyor belt. Since μ is a continuous function, no extra equation is necessary to distinguish the motions sliding and locking. During lift off, the system has two DoFs (ϕ, y) and the equations of motion read [137]

---

[1] The *leading edge* is the brake pad edge were a rotating point on the disc gets first in contact with the brake pad, at the trailing edge this point exits the contact area.

$$\left(J + \left(\frac{L_2}{2}\right)^2 m_2\right)\ddot{\phi} + \frac{L_2}{2} m_2 \sin(\phi)\ddot{y} + d_2\dot{\phi} + \frac{L_2}{2} m_2 g \sin(\phi) + k_2(\phi - \phi_0) = 0, \tag{2.21}$$

$$(m_1 + m_2)\ddot{y} + \frac{L_2}{2} m_2 \sin(\phi)\ddot{\phi} + \frac{L_2}{2} m_2 \cos(\phi)\dot{\phi}^2 + d_1\dot{y} + k_1(y - y_0) + (m_1 + m_2)g = 0, \tag{2.22}$$

where ϕ_0 and y_0 indicate the positions of the springs when they are free of tension. Additionally, it is assumed that the pin (mass m_2, length L_2) is homogeneous. Therefore, its centre of gravity C_G is in its middle at $L_2/2$. The moment of inertia of the pin with respect to the C_G is given by J. As the pivot is not equal to the C_G of the pin, the moment of inertia has to be extended using the *parallel axis theorem* or *Huygens-Steiner* theorem. The moment of inertia with respect to the pivot is then given by the first term in Equ. (2.21).

During contact the system has only one DoF because $y = L_2 \cos\phi$. Figure 2.13 shows the free body diagram of pin and block mass. In addition to the forces of the spring F_{1k} and damper F_{1d}, a contact normal force F_N and a friction force F_F act on the system. Including the friction law given by Equ. (2.20) it holds

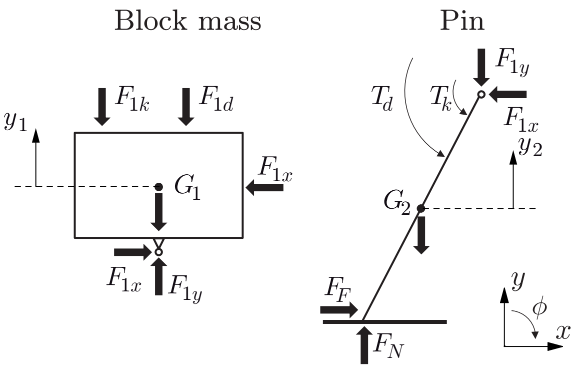
Block mass

Pin

Figure 2.13.: Free body diagram of pin and block mass.

$$F_F = F_N \mu(v_{\mathrm{rel}}). \tag{2.23}$$

The forces and torques as depicted in Fig. 2.13 read

$$
\begin{aligned}
T_k &= k_2(\phi - \phi_0), && (2.24)\\
T_d &= d_2\dot{\phi}, && (2.25)\\
F_{1k} &= k_1(y_1 - y_0), && (2.26)\\
F_{1d} &= d_1\dot{y}_1, && (2.27)\\
G_1 &= m_1 g, && (2.28)\\
G_2 &= m_2 g. && (2.29)
\end{aligned}
$$

The principle of linear momentum in vertical direction for the free bodies, which are block mass (y_1) and pin (y_2), see Fig. 2.13, gives

$$
\begin{aligned}
m_1\ddot{y}_1 &= F_{1y} - d_1\dot{y}_1 - k_1(y_1 - y_0) - m_1 g, && (2.30)\\
m_2\ddot{y}_2 &= F_N - F_{1y} - m_2 g. && (2.31)
\end{aligned}
$$

The principle of angular momentum around the connection point between pin and block mass reads[2]

$$
\begin{aligned}
\left(J + \left(\frac{L_2}{2}\right)^2 m_2\right)\ddot{\phi} = -T_d - T_k - \frac{L_2}{2} m_2 \sin(\phi)\ddot{y}_1 - m_2 g \frac{L_2}{2}\sin(\phi)\\
-F_F L_2 \cos(\phi) + F_N L_2 \sin(\phi). \qquad (2.32)
\end{aligned}
$$

Using Equ. (2.30) and Equ. (2.31) F_{1y} can be eliminated and by solving the equation for F_N

$$F_N = m_1\ddot{y}_1 + m_2\ddot{y}_2 + d_1\dot{y}_1 + k_1(y_1 - y_0) + m_1 g + m_2 g. \qquad (2.33)$$

The geometry of the contact phase gives the relation between the heights y_1, y_2 and angle ϕ and read

$$
\begin{aligned}
y_1 &= L_2\cos(\phi) &&= 2y_2, && (2.34)\\
\dot{y}_1 &= -L_2\sin(\phi)\dot{\phi} &&= 2\dot{y}_2, && (2.35)\\
\ddot{y}_1 &= -L_2(\cos(\phi)\dot{\phi}^2 + \sin(\phi)\ddot{\phi}) &&= 2\ddot{y}_2. && (2.36)
\end{aligned}
$$

Inserting Equ. (2.34), Equ. (2.35) and Equ. (2.36) into Equ. (2.33) yields

$$
\begin{aligned}
F_N = -m_1 L_2(\cos(\phi)\dot{\phi}^2 + \sin(\phi)\ddot{\phi}) - m_2\frac{L_2}{2}(\cos(\phi)\dot{\phi}^2 + \sin(\phi)\ddot{\phi})\\
- d_1 L_2 \sin(\phi)\dot{\phi} + k_1(L_2\cos(\phi) - y_0) + m_1 g + m_2 g. \qquad (2.37)
\end{aligned}
$$

---

[2] Because this point can move the term $m_2 \cdot g \cdot L_2 \cdot \sin(\phi)/2$ follows because of the pins inertia.

The conservation of angular momentum, Equ. (2.32), can now be reformulated to one equation of motion of the variable ϕ, which describes the movement of the system during contact of the pin with the conveyor belt and reads

$$\begin{aligned}\left(J+\left(\frac{L_2}{2}\right)^2 m_2\right)\ddot{\phi}-\frac{L_2^2}{2}m_2\sin(\phi)\left(\cos(\phi)\dot{\phi}^2+\sin(\phi)\ddot{\phi}\right)+d_2\dot{\phi}+k_2(\phi-\phi_0)\\ +m_2 g\frac{L_2}{2}\sin(\phi)+F_N L_2(\mu\cos(\phi)-\sin(\phi))=0.\end{aligned} \tag{2.38}$$

Equation (2.38) is a differential equation of second order without any closed analytical solutions. Cantoni et al. [31] even postulated that a time-domain simulation is the only proper way to analyse the dynamic behaviour of a brake system when the effects of non-linearities are present. Thus, the system has to be investigated numerically in the time domain considering an appropriate integration strategy because of the varying DoFs. Figure 2.14 shows the ϕ-t diagram (left) and phase plots of ϕ (right) for two about identical parameter sets which almost equals the parameters given in the minimal model by Popp et al. [137]. Table 2.1 shows the used parameters.

Table 2.1.: Expanded sprag-slip model parameter set.

m_1:	10	kg	g:	0	m/s^2
m_2:	6	kg	ϕ_0:	$\pi/9$	rad
J:	0.005	kgm^2	y_0:	0	m
d_1:	0.1	Ns/m	v_C:	0.1	m/s
d_2:	0.01	Nm/s	μ:	0.4	-
L_2:	0.1	m			

In Fig. 2.14 only the stiffness k_1 and k_2 are varied. More precisely: the stiffness of the upper diagram are $k_1 = 100\,\mathrm{N}/\mathrm{m}$ and $k_2 = 10\,\mathrm{Nm}/\mathrm{rad}$, for the bottom diagram $k_1 = 200\,\mathrm{N}/\mathrm{m}$ and $k_2 = 20\,\mathrm{Nm}/\mathrm{rad}$. Both simulations result in a self-excited vibration. Nevertheless, two things are different: the reached limit cycle and the amplification rate.

In the lower depiction of Fig. 2.14 the amplification rate of the vibration is high and the limit cycle is reached fast. In the upper diagram the vibration has a lower amplification rate, but a more than one third higher limit cycle amplitude. In the end, the higher limit cycle amplitude indicates a more critical vibration. Calculating the eigenvalues of the system delivers the eigenfrequency and the associated amplification rate, but not the reached limit cycle. This is also one of the main challenges for the computer-based calculation methods which will be discussed in Chap. 3.

To investigate the influence of the different parameters on the stability of the system, a sensitivity analysis is performed. As initial conditions the block is held at a certain height at which the pin is relaxed and just not in contact with the conveyor belt. Thus,

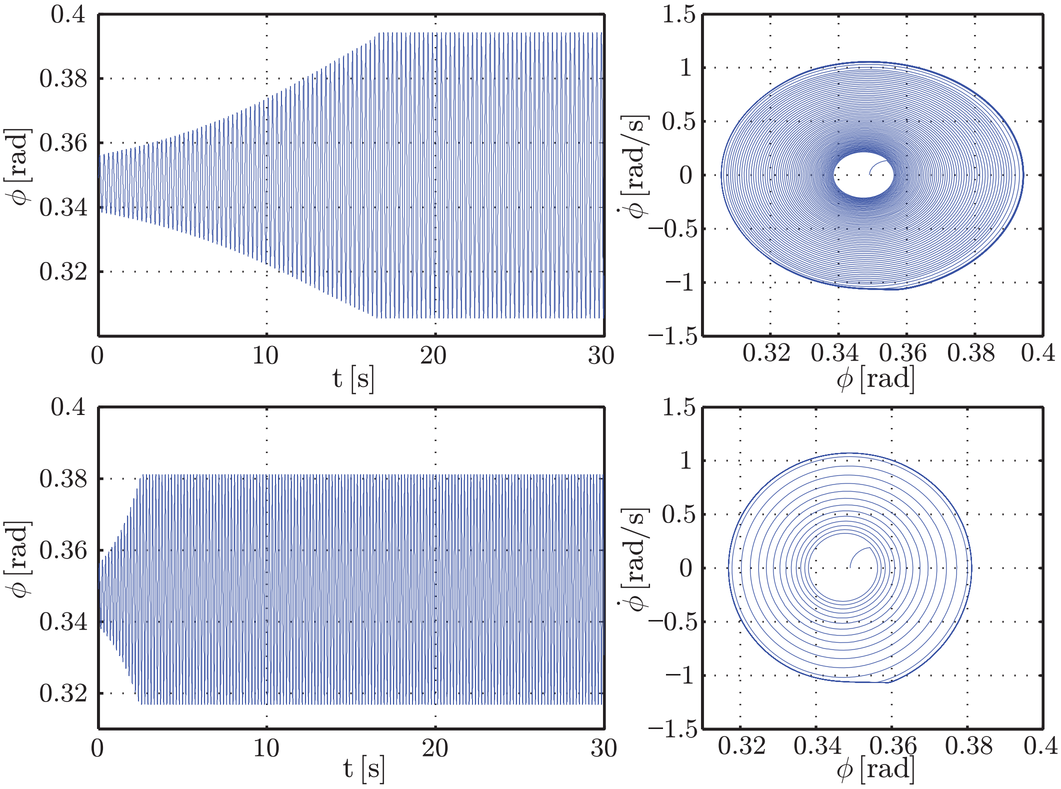

Figure 2.14.: Angle ϕ vs time plot and phase portrait for two different parameter sets.

the system falls down on the conveyor belt. These initial conditions are unchanged during the sensitivity analysis. To investigate the impact of the parameters on the stability, two of them are varied within a certain range. The motion of the first five seconds is calculated, which is taken as transient response of the system.

As it can be seen in the upper diagram in Fig. 2.14, the final limit cycle and thus the transient response may not be reached after five seconds. However, to keep simulation time of the stability chart within reasonable limits, this end time was chosen. The amplitude ϕ of this transient response is compared with a predefined limit value. Instability is defined if this limit value is exceeded.

Figure 2.15 shows such an obtained stability chart. In that case, the stiffness of the system (k_1, k_2) is varied and a point indicates an instability. It can be seen that a certain minimum value is needed for k_1 to obtain instability. This is only partially true, because the amplification rate of the simulations with $k_1 = 100\,\mathrm{N/m}$ is small and thus the limit cycle. Hence the maximum amplitude, is not reached within the simulation time of five seconds, see also Fig. 2.14. A higher stiffness k_1 leads rather to an unstable solution and a higher stiffness k_2 more likely leads to a stable solution. Due to the higher stiffness, the pin sprags earlier which results in a lower limit cycle amplitude.

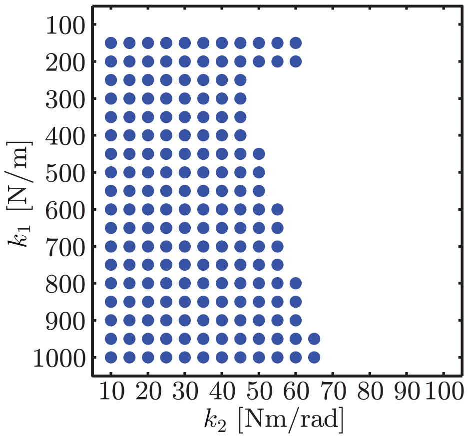

Figure 2.15.: Stability chart for varying stiffness.

Nevertheless, there are combinations with a high value of k_2 and a low value of k_1 which result in instability. At the beginning the amplification rate is low but increases with continuation of the vibration. Figure 2.16 shows this phenomenon. One explanation of this effect is that the excitation mechanism of the negative friction-velocity slope and the sprag-slip mechanism (lift off) are coupled. However, the lift off also limits the amplitude of the vibration.

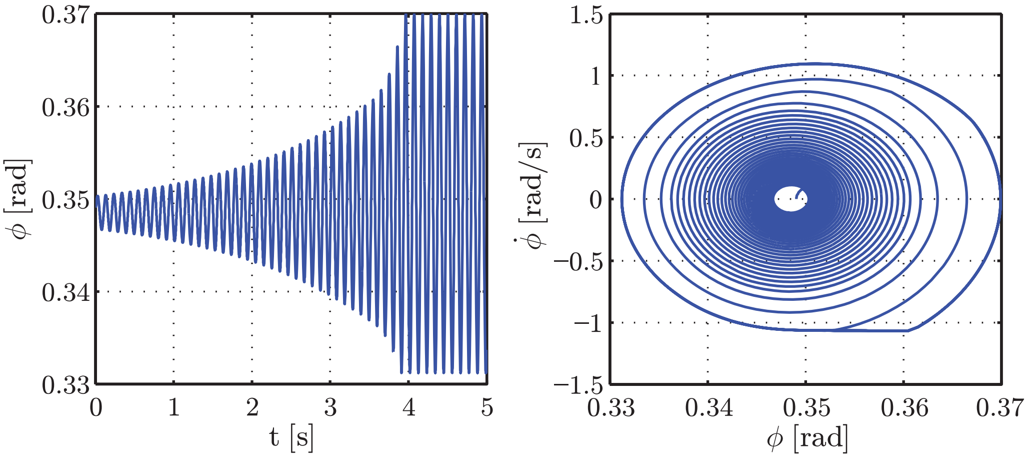

Figure 2.16.: Angle ϕ vs time plot and phase portrait ($k_1 = 200\,\mathrm{N/m}$, $k_2 = 60\,\mathrm{Nm/rad}$).

2.3. Minimal Model by Matsushima et al. [111]

Matsushima et al. [111] presented an interesting approach for an optimal design method to avoid brake squeal. After investigations on an existing brake system, the aim was to develop a simplified model of the brake system which includes the most relevant parameters. Figure 2.17 shows the corresponding minimal model.

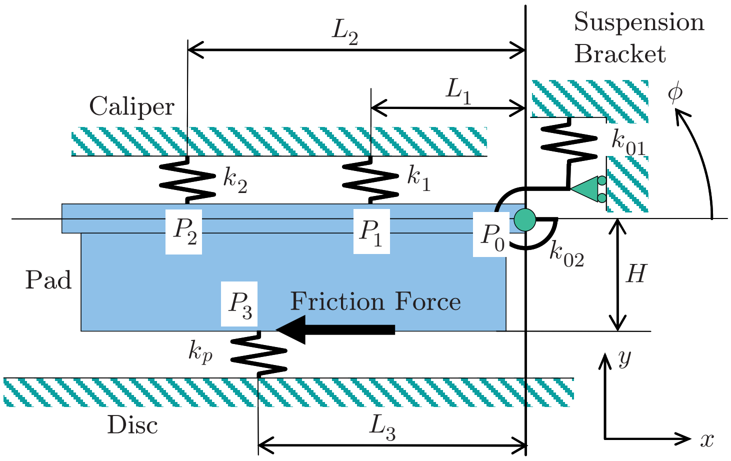

Figure 2.17.: Analytical minimal model by Matsushima et al. [111], for better explanation the original figure has been slightly modified.

In the paper some assumptions are unquoted. However, due to the similarity to real brake systems, this model is chosen for a comparative study of an FEM model in this work. The results are presented in Chap. 3. In this chapter the minimal model and the simplifications made are discussed in detail.

As can be seen in Fig. 2.17 the brake pad is held in position by the two springs k_1 and k_2 at the top. These springs represent the pistons of the caliper. The spring at the bottom k_p represents the contact stiffness between disc and pad. At this point P_3 the friction force is applied. Another boundary condition of the pad is the suspension bracket, which is a part of the caliper. At the movable point P_0 the forces of the vertical spring k_{01} and the rotational spring k_{02} act. Furthermore, L_1, L_2, L_3 and H declare the horizontal and vertical distances of the springs to P_0. The pad has three DoFs: x, y and ϕ.

Figure 2.18 shows the different reacting forces as a result of small deflections of the pad along y-direction and around ϕ-rotation. First simplifications are already done: first of all, it is assumed that only small angular deflections occur. Hence, the simplification $\sin\phi = \phi$ applies. Second, no motion in x-direction is possible. Consequently, the friction force enters the equations of motions only as a torque about point P_0. Third, there is no information given about the centre of gravity of the brake pad. Based on the data in [111], it is assumed, that C_G is located at a distance of L_3 in x-direction and $H/2$ in y-direction. Additionally, gravity is neglected. Thus, the equilibrium of forces in y-direction reads

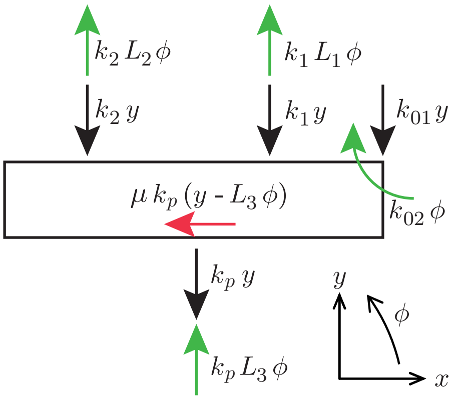

Figure 2.18.: Depiction of the acting forces of the minimal model shown in Fig. 2.17.

$$m\ddot{y} = \phi(k_1L_1 + k_2L_2 + k_pL_3) - y(k_1 + k_2 + k_{01} + k_p). \tag{2.39}$$

This equation is simplified using the trial functions for y and ϕ

$$\begin{aligned} y =& \quad y_0e^{\lambda t} & \phi = \phi_0e^{\lambda t}, \quad (2.40)\\ \ddot{y} =& \quad \lambda^2 y_0e^{\lambda t} & \ddot{\phi} = \lambda^2\phi_0e^{\lambda t}, \quad (2.41)\end{aligned}$$

where λ indicates the complex eigenvalue. Thus, the following equation applies:

$$\frac{\phi_0}{y_0} = \frac{m\lambda^2 + (k_1 + k_2 + k_{01} + k_p)}{k_1L_1 + k_2L_2 + k_pL_3}. \tag{2.42}$$

Calculating the equilibrium of moments about the point P_0 results in

$$\begin{aligned} J\ddot{\phi} = m&L_3\ddot{y} + y(k_1L_1 + k_2L_2 + k_pL_3 - \mu k_pH)\\ &-\phi(k_{02} + k_1L_1^2 + k_2L_2^2 + k_pL_3^2 - \mu k_pHL_3). \end{aligned} \tag{2.43}$$

In this equation J equals the moment of inertia with respect to P_0 around the ϕ-rotation. The term $mL_3\ddot{y}$ in that equation exists because P_0 is a moveable point. This term is caused by the inertia force ($m\ddot{y}$) and acts at the C_G in y-direction (distance L_3). Insertion of Equ. (2.40) and Equ. (2.41) yields in

$$\frac{\phi_0}{y_0} = \frac{mL_3\lambda^2 + (k_1L_1 + k_2L_2 + k_pL_3 - \mu k_pH)}{J\lambda^2 + (k_{02} + k_1L_1^2 + k_2L_2^2 + k_pL_3^2 - \mu k_pHL_3)}. \tag{2.44}$$

Equalising the two Equ. (2.42) and Equ. (2.44) for the elimination of ϕ_0/y_0 and resolving results in

$$\frac{m\lambda^2 + (k_1 + k_2 + k_{01} + k_p)}{k_1L_1 + k_2L_2 + k_pL_3} = \frac{mL_3\lambda^2 + (k_1L_1 + k_2L_2 + k_pL_3 - \mu k_pH)}{J\lambda^2 + (k_{02} + k_1L_1^2 + k_2L_2^2 + k_pL_3^2 - \mu k_pHL_3)}, \tag{2.45}$$

where the terms of this equation can be roughly ordered by the powers of λ which reads

$$\begin{aligned} \lambda^4\{Jm\} + \lambda^2\{J(k_1+k_2+k_{01}+k_p) + m(k_{02}+k_1L_1^2+k_2L_2^2+k_pL_3^2-\underline{\mu k_pHL_3})\} \\ +\{[k_1+k_2+k_{01}+k_p][k_{02}+k_1L_1^2+k_2L_2^2+k_pL_3^2-\underline{\mu k_pHL_3}] \\ -[k_1L_1+k_2L_2+\underline{k_pL_3}][k_1L_1+k_2L_2+\underline{k_pL_3}+\underline{mL_3\lambda^2}-\mu k_pH]\} = 0. \end{aligned} \tag{2.46}$$

Comparing the re-calculated coefficients with those of the calculated equations of [111], the simplifications made can be determined. Some of the terms are missing due to the simplifications. They are underlined in Equ. (2.46). Now the simplifications made can be determined:

- Term k_pL_3: There is no reaction force caused by the angular deflection ϕ in point P_3. However, the caused torque in the equilibrium of moments ($k_pL_3^2$) is still taken into account.
- Term μk_pHL_3: As a result of ignoring the term of the reaction force (k_pL_3) the associated entry in the friction force is also missing.
- Term $mL_3\lambda^2$: The equilibrium of moments is calculated around point P_0, but this point is supported by a vertical spring and can move in a vertical direction. Nevertheless, the equations are calculated under the assumption that P_0 is a fixed-point and cannot move.

Figure 2.19 shows the resulting depiction of the forces including these simplifications. Now the characteristic polynomial reads

$$\begin{aligned} \lambda^4\{\overbrace{Jm}^{A}\} + \lambda^2\{\overbrace{J(k_1+k_2+k_{01}+k_p)+m(k_{02}+k_1L_1^2+k_2L_2^2+k_pL_3^2)}^{B}\} \\ C\left\{ \begin{array}{r} +\{[k_1+k_2+k_{01}+k_p][k_{02}+k_1L_1^2+k_2L_2^2+k_pL_3^2] \\ -[k_1L_1+k_2L_2][k_1L_1+k_2L_2-\mu k_pH]\} \end{array} \right. \\ = 0, \end{aligned} \tag{2.47}$$

where the eigenvalues can be calculated using the quadratic formula

$$\lambda^4A+\lambda^2B+C=0 \Rightarrow \lambda_{1,2,3,4} = \pm\sqrt{\frac{-B\pm\sqrt{B^2-4AC}}{2A}}. \tag{2.48}$$

Figure 2.20 shows the result for the complex eigenvalues λ over varying friction coefficients μ. Looking at the left side it can be seen that there is a critical friction coefficient at $\mu_{\text{cri}} = 0.514$. A further increasing friction coefficient beyond this value leads to bifurcation and therefore to a positive real part which indicates instability and furthermore

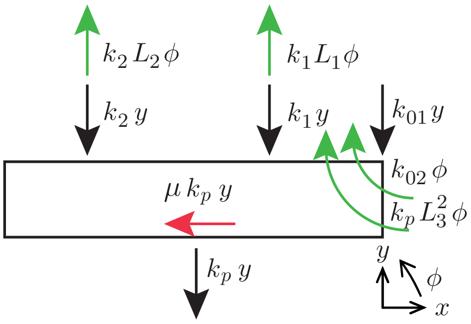

Figure 2.19.: Depiction of the acting forces of the minimal model shown in Fig. 2.17 including simplifications.

squeal. The right side of Fig. 2.20 shows the curves of imaginary part of the eigenvalues which equals the eigenfrequencies. It can be observed that two eigenfrequencies are coupled if the critical friction coefficient is reached.

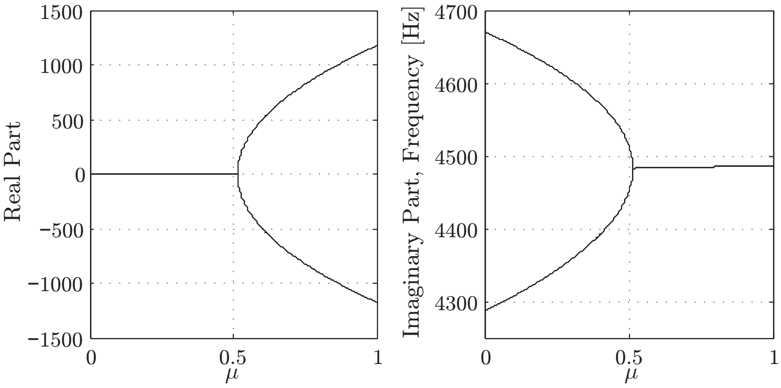

Figure 2.20.: Complex eigenvalue results, variation μ.

Something similar can be observed if the contact stiffness k_p is varied. Thereby, the friction coefficient is assumed to be constant ($\mu = 0.6$). Figure 2.21 shows the results for the complex eigenvalues. There is a critical region for $k_p = 1.02 \cdot 10^8 \ldots 2.85 \cdot 10^8$ N/m where the system is self-excited to unstable vibrations. The mode-coupling and decoupling can be observed at the right side. Additionally, it can be seen that the squeal frequency depends on the contact stiffness.

Matsushima et al. [111] used this model to define a critical brake squeal region R_S and the possible available region regarding friction coefficient and contact stiffness R_P, see Fig. 2.22. These two factors are the main driving factors for brake squeal which can also be varied. In addition, some geometric design parameters are included (L_1, L_2, L_3 and H) which shall be used for optimisation. This optimisation shall minimise the region of intersection of R_S and R_P, but a sensitivity analysis showed only a small influence of these parameters because their range of variation is limited.

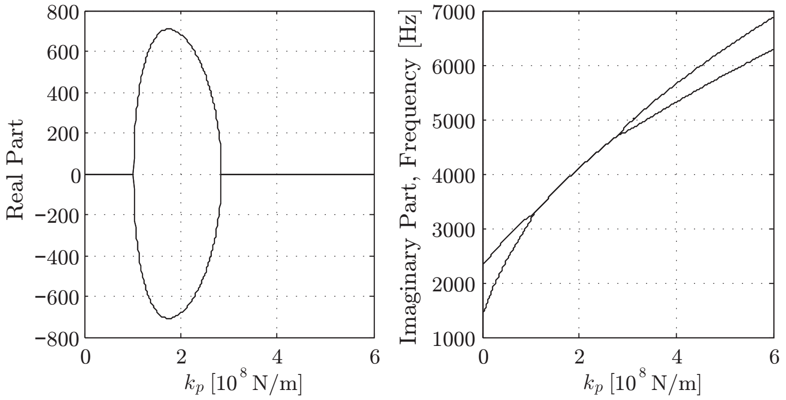

Figure 2.21.: Complex eigenvalue results, variation k_p.

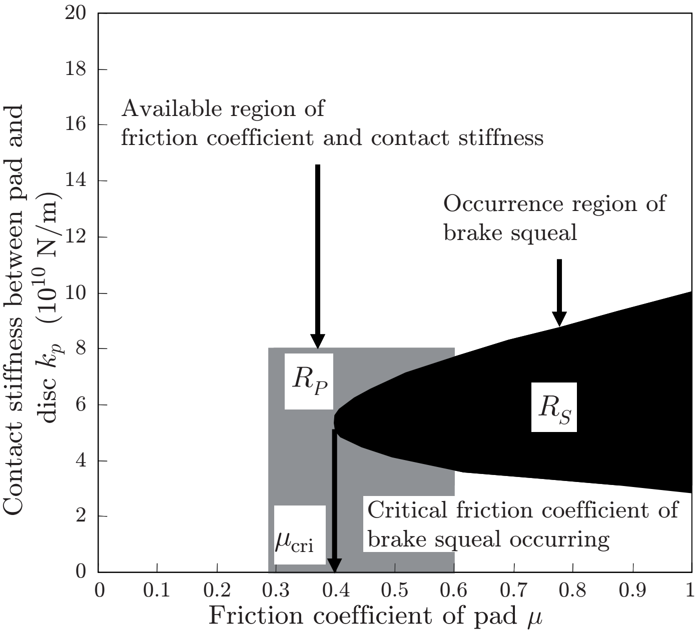

Figure 2.22.: Final results for brake system design by Matsushima et al. [111].

The simplifications made are hardly to understand. As a consequence, simulations are performed without the simplifications regarding Equ. (2.46). Figure 2.23 and Fig. 2.24 show the result for the identical parameter set. Now the critical friction coefficient is already at $\mu_{\text{cri}} = 0.096$. Additionally the stable region for contact stiffness variation starts at $k_p = 3.77 \cdot 10^8\ \text{N/m}$.

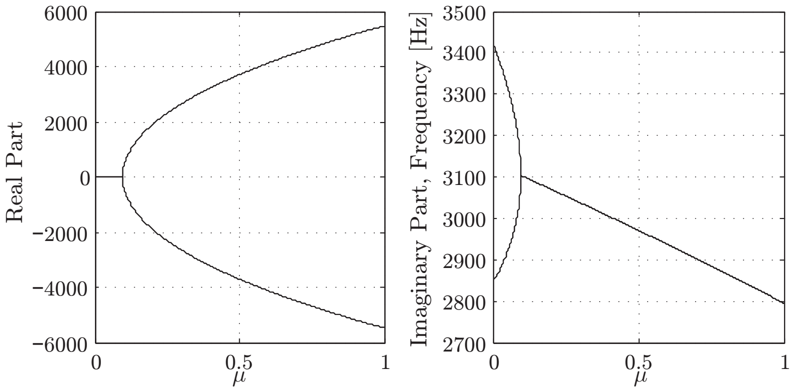

Figure 2.23.: Complex eigenvalue results model without simplifications, variation μ.

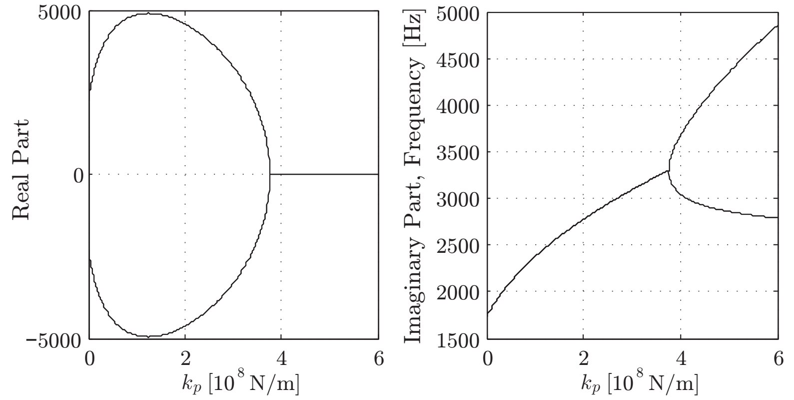

Figure 2.24.: Complex eigenvalue results model without simplifications, variation k_p.

Due to the use of the complete equations of motion without simplifications, the behaviour of the minimal modes changes significantly. In fact, the stable region of the parameter set is significantly reduced. Nevertheless, this model presented an interesting approach which has similarities to a real brake system. Therefore, this model has been investigated in detail and used for comparison with the FEM model presented in Chap. 3.

3. Finite Element Method

3.1. Introduction

The *Finite Element Method* (FEM)[1] has become increasingly popular in the last decades. Among others, one reason for this is the steady increasing computational power which allows the calculation and simulation of very detailed models. Regarding brake squeal, two different methods are mainly used: the *Complex Eigenvalue Analysis* (CEA) and the *Transient Analysis* (TA), which will be explained in detail later. The model approach of the FEM is based on the decompensation of the real continuous structure into a finite number of more or less simple partial elements, so called *"finite elements"*, which are connected to each other at certain nodes. The deformation of the structure is then approximately described by the DoFs of the nodes.

Due to the increasing computation power, the level of detail has increased significantly. Figure 3.1 left presents an FEM model from [101] published in 1989. This was the first published work including an acoustic FEM analysis of a real brake system. In contrast to, Fig. 3.1 right displays the FEM model of the tested brake disc used in this work at the beginning of the investigations. Here tetrahedral elements are used and even the ventilation holes are modelled.

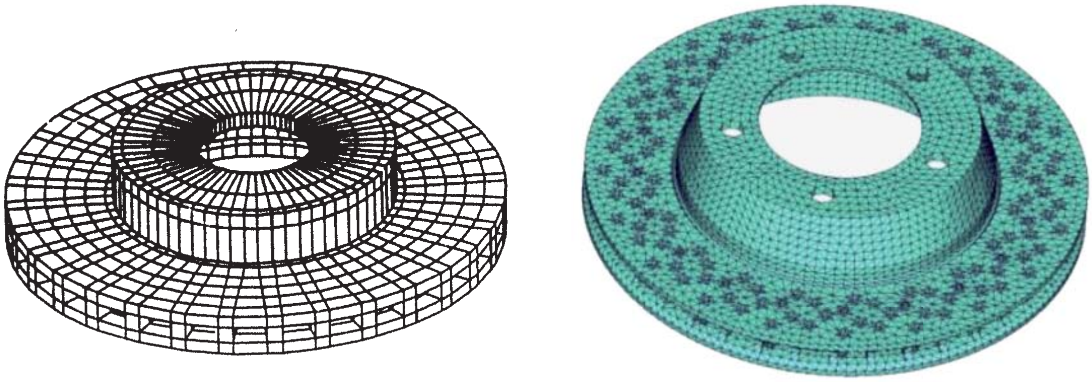

Figure 3.1.: Development of brake disc meshes, left brake disc mesh published by Liles [101] in 1989, right investigated ventilated brake disc meshed with tetrahedral elements.

---

[1] Also known as *Finite Element Analysis* (FEA).

To underpin this known development, the meshes of the caliper are also presented. Fig. 3.2 left shows the first mesh published by Liles [101] and Fig. 3.2 right demonstrates the current mesh of the investigated brake system.

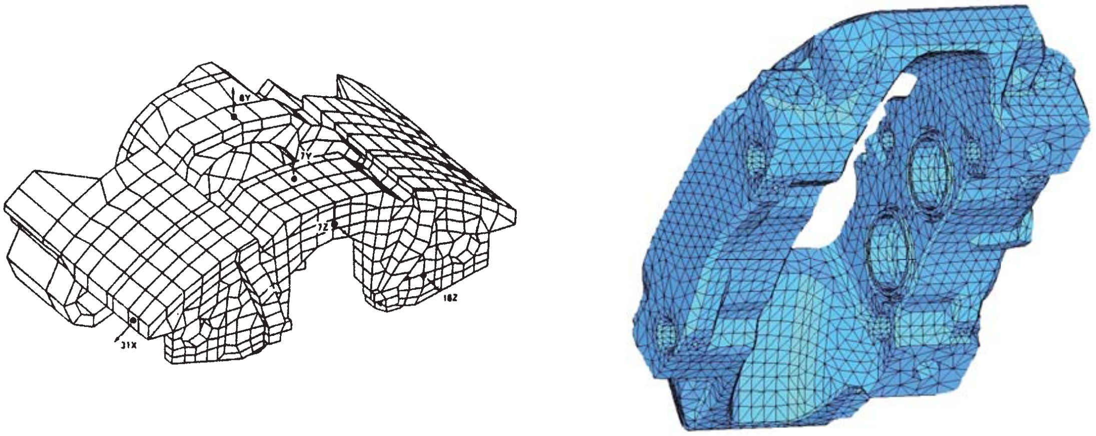

Figure 3.2.: Development of brake caliper meshes, left brake caliper mesh published by Liles [101] in 1989, right investigated brake caliper meshed with tetrahedral elements.

3.1.1. Complex Eigenvalue Analysis

The necessary discretisation and linearisation due to the FEM, which will be discussed in detail later, results in a system of equation of motions. The general and linearised form reads

$$\mathbf{M} \cdot \ddot{\mathbf{u}} + (\mathbf{D} + \mathbf{G}) \cdot \dot{\mathbf{u}} + (\mathbf{K} + \mathbf{N}) \cdot \mathbf{u} = \mathbf{F}_{\text{ext}}(t), \tag{3.1}$$

where $\mathbf{M}$ declares the mass matrix, $\mathbf{D}$ the damping matrix and $\mathbf{K}$ the stiffness matrix, which are symmetric. Because of the large rotation the skew-symmetric gyroscopic matrix $\mathbf{G}$ and circulatory matrix $\mathbf{N}$ also exist. Furthermore, $\mathbf{F}_{\text{ext}}$ describes the time depending external forces and $\mathbf{u}, \dot{\mathbf{u}}, \ddot{\mathbf{u}}$ the displacement, velocity and acceleration of the nodes [120].

Since brake squeal occurs at low speed, the gyroscopic, hence the skew-symmetric terms $\mathbf{G}$ and $\mathbf{N}$ can be neglected, see e.g. [107]. The friction force is the only non-conservative external force[2] and can be implemented under the assumption of a constant friction coefficient μ through geometrical coupling ($F_F = \mu \cdot F_N$, friction force equals normal force times friction coefficient). Therefore, the friction force depends on the normal displacement $\mathbf{u}$ of the nodes in contact.

---

[2] Non-conservative force means, that if the force works along a path this energy is not stored as potential energy.

So it is possible to model the contact nodes along the friction contact with friction-loaded springs [101, 119, 133, 134], also compare Chap. 2. The friction-loaded springs enter Equ. (3.1) via part of the stiffness matrix denoted as $\mathbf{K}_F$. Due to this the resulting stiffness matrix $\mathbf{K}_{\text{sum}}$ becomes skew-symmetric. The external forces are neglected and therefore $\mathbf{F}_{\text{ext}}$ equals zero. Thus, the resulting equation of motion reads

$$\mathbf{M} \cdot \ddot{\mathbf{u}} + \mathbf{D} \cdot \dot{\mathbf{u}} + \underbrace{(\mathbf{K} + \mathbf{K}_F)}_{\mathbf{K}_{\text{sum}}} \cdot \mathbf{u} = 0. \tag{3.2}$$

From this equation, the eigenvalues can be calculated using the trial function $\mathbf{u} = \mathbf{u}_0 \cdot e^{\lambda \cdot t}$ which results in the characteristic polynomial written as

$$\lambda^2 \mathbf{M} + \lambda \mathbf{D} + \mathbf{K}_{\text{sum}} = 0. \tag{3.3}$$

The skew-symmetric part in $\mathbf{K}_{\text{sum}}$ leads to complex eigenvalues. For the calculation of these eigenvalues it is necessary to linearise the system at a steady state. Therefore, a steady sliding condition is assumed and for the first iteration step a *normal mode calculation* is performed [133]. This means that the classical calculation procedure is:

1. Calculate the contact, hence the contact pressure distribution.
2. Calculate the *normal modes* of the system neglecting the non-conservative forces ($\mathbf{K}_F = 0$).
3. Calculate the *complex modes*, using the normal modes as first iteration step

For example, the software package *MD Nastran* [112] delivers as calculation result a list of complex eigenvalues λ given by

$$\lambda_j = \delta_j \pm i \cdot \omega_j, \qquad j = 1, 2, \ldots, N_j, \tag{3.4}$$

where α and ω denote the real value and the imaginary value and N_j is the number of vibratory modes. The frequency f can be calculated by

$$f_j = \frac{\omega_j}{2 \cdot \pi}, \tag{3.5}$$

and the damping coefficient g is defined as

$$g_j = \frac{-2 \cdot \delta_j}{\omega_j}. \tag{3.6}$$

Such an exemplary result is shown in Tab. 3.1. In this case an unstable frequency at 1030 Hz could be identified.

Equation (3.6) indicates that if a complex eigenvalue has a positive real part, the damping coefficient gets negative, which is an indicator for instabilities, because the system may exhibit self-excited vibrations. Nevertheless, the common problem in CEA

Table 3.1.: Example of an *MD Nastran* output file, an unstable complex frequency is indicated by a positive real eigenvalue and a negative damping coefficient, see root number four. The unstable frequency is typically one of the double frequencies (marked).

ROOT NO.	EXT. ORDER	EIGENVALUE (REAL)	EIGENVALUE (IMAG)	FREQ. (CYCLES)	DAMPING COEF.
1	1	-11.9	4810	765	0.00496
2	2	-10.8	4940	786	0.00438
3	3	-13.4	5600	892	0.00477
4	**4**	**60.5**	**6440**	**1030**	**-0.0188**
5	**5**	**-89.6**	**6440**	**1020**	**0.0278**
6	6	-13.5	7510	1200	0.00359

is that there is an overestimation of unstable modes. Figure 3.3 shows an exemplary result from [107]. There are several critical frequencies with negative damping visible, but not all of them are observable in experiments.

The reason for that is that the negative damping values only indicate the amplification rates of the system, but the CEA cannot give information on the reached limit cycles of these vibrations. Therefore, only information on the increase of the vibration amplitude, and not about the maximum amplitudes, is gained. Nevertheless, the CEA delivers the *Operational Deflection Shape* (ODS) at certain frequencies. Together with experimental results, the relevant unstable frequencies can be determined and the influence of countermeasures on these frequencies can be examined.

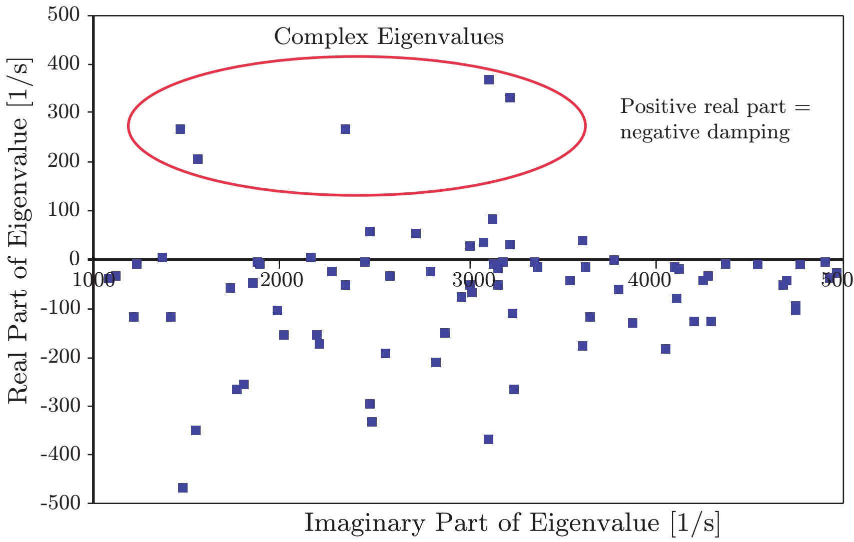

Figure 3.3.: Exemplary results of CEA [107].

3.1.2. Transient Analysis

In contrast to the static CEA, the *Transient Analysis* (TA) may include time-depending parameters. Thus, the effect of the vibration on the contact pressure distribution, or the changing friction coefficient with respect to speed and/or temperature can be taken into account. A stability analysis can be performed and limit cycles calculated. Solutions for situations can be simulated, which are far away from the equilibrium point and where non-linear effects are present [8, 11, 121, 122].

Nevertheless, the solution is in the time domain (note: solution of the CEA is in the frequency domain) and has to be transferred into the frequency domain applying e.g. *Fast Fourier Transformation* (FFT), see Chap. 4.3.3. The maximum frequency which should be analysed influences the maximum time step of the simulation. Ouyang et al. [133] denoted that, if vibrations up to a maximum frequency of 10 kHz are analysed, a time step smaller than 10^{-5} sec must not be exceeded. Vermot des Roches et al. used in their TA of a squealing brake a time step smaller than 10^{-7} sec [163].

Additionally, the TA delivers a huge amount of data and requires considerable calculation time. Due to this, sensitivity analyses of certain parameters are very time consuming. From the engineering point of view, the most common method is the CEA at the moment. Nevertheless, for example Mahajan et al. [106] declare that squeal analysis "*cannot be met by one single method*". Also Ouyang et al. [133] mentioned the following:

> *"These different methods all have a place at different stages of the analysis and are useful for different purposes. It is expected that a variety of analysis methods will coexist and the transient analysis will become more popular in future."* [133].

3.2. Analyses

As mentioned above, the main advantage of the TA in contrast to the CEA is, that time-depending mechanisms such as changes in the brake pressure distribution due to wear, are taken into account. For example Mueller and Ostermeyer [118], Ostermeyer [127] and Wahlström [166] presented *cellular automata* models for the contact. In that model the distribution changes continuously and small wear particles start to vibrate in phase.

The main question is, how strong does the contact influence the results of the CEA? Additionally, the calculation algorithms are "black boxes" in the commercial software, hence it is not possible to take a look at the used algorithm. To gain further insight into the calculation method, an FEM model with different discretisation levels is developed and simulated using two different software packages. Additionally, these results are compared with the results from experimental testing. The different investigations and the results will be explained step by step in the following.

The first aim of the investigation is to examine the calculation method in *MD Nastran*. Therefore, a simple analytical model from Matsushima et al. [111], which is explained in detail in Chap. 2, is investigated.

Next, the FEM model is modelled in a similar manner to this analytical model. Figure 3.4 shows the simplified FEM model. Among other simplifications, only one hexahedral element is used for the contact calculation. For the reason of comparison the friction value of the analytical and the FEM model is varied and the complex eigenvalue calculated. Above a certain value, mode-coupling occurs and the system becomes unstable.

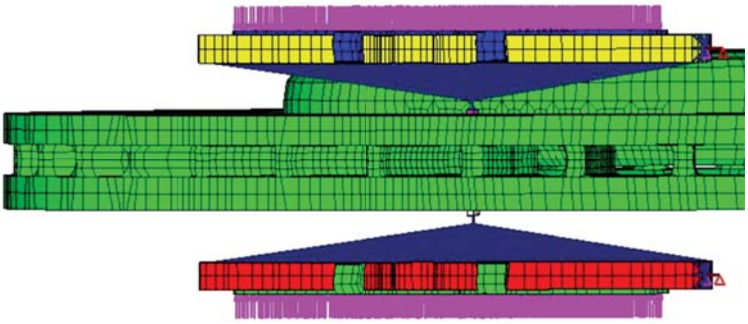

Figure 3.4.: Simplified finite element model: only one hexahedral element is used for the pad which is in contact. The system is similar to the analytical minimal model of Matsushima et al. [111], depicted in Fig. 2.17.

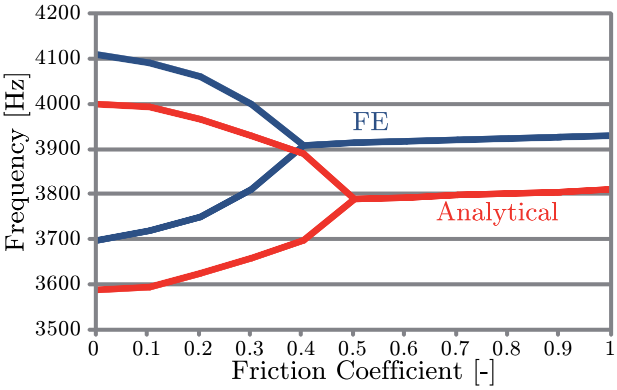

Figure 3.5.: Comparison of the results for the simplified models.

The results are compared in Fig. 3.5. As can be seen, the results are qualitatively similar. The different discretisation level of the two models leads to an expected difference in the results. Of course, it is not possible to simplify a complex FEM model in the same way as an analytical model. Nevertheless it can be seen, that the algorithm of the FEM software in principle works so far and instabilities can be calculated.

3.2.1. First Complex Eigenvalue Analysis

Next, the CEA is performed as described in the *MD Nastran* manual. The investigated model includes the brake disc with different mesh types, see Fig. 3.1 right for the first mesh using tetrahedral elements including the holes and Fig. 3.6, which is the final mesh where hexahedral elements are used and the holes are neglected. Furthermore, the brake pads (hexahedral elements including brake pad backplate), the brake pistons (hexahedral elements) and the brake caliper (tetrahedral elements) are included in the model.

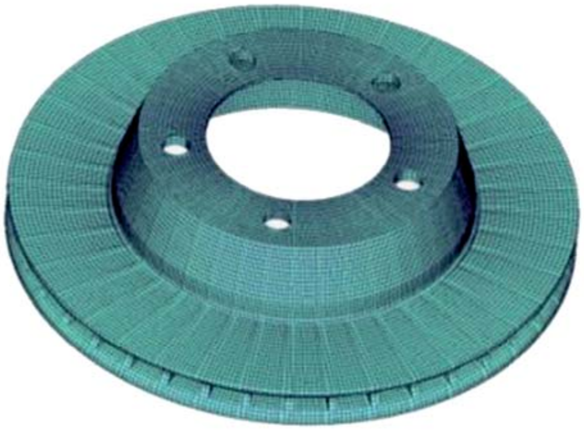

Figure 3.6.: Remeshed ventilated brake disc without ventilation holes with hexahedral elements.

The system is restrained at the position of the screws, which mount together brake caliper and wheel carrier. At these nodes, all six DoFs are locked. Also the three translational movements of the disc are locked as well as the rotational movement of the disc. As a consequence the calculation runs faster and more stable without changing the results. The complete FEM model is depicted in Fig. 3.7 left.

The second set-up also includes wheel carrier, shock absorber, spring, steering link and lower control arm. For reasons of clarity, Fig. 3.7 right shows only a principal depiction of these parts. In that case the boundary condition are the connection points of the suspension to the car body. At these joints all six DoFs are locked. The restraints of the translational movements of the disc are removed, because the disc is mounted to the wheel carrier. Only the rotational movement is locked again for faster calculation.

First of all, a calculation with the small model and the very detailed tetrahedral mesh for the brake disc is performed. The calculation algorithm in *MD Nastran* is called *BSQUEAL* and uses an implicit nonlinear solver (*SOL 600*). Thereby, the analysis is divided into two steps:

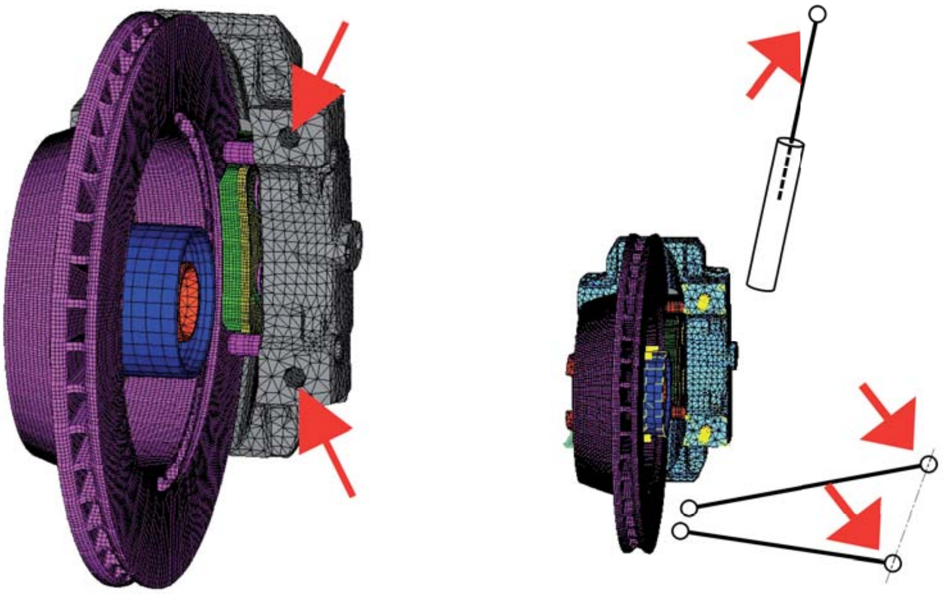

Figure 3.7.: Comparison investigated FEM models, left *small model*, right *complete model*. Boundary conditions are marked with arrows (all six DoFs locked).

1. **Static contact calculation:** Thereby, the brake pressure is applied in ten steps. In this calculation step the nonlinearities of the brake pad material as well as due to the contact calculation are taken into account.
2. **Complex eigenvalue extraction:** Linearisation is needed for the first performed normal mode calculation. This result is used as first iteration for the CEA, which identifies the unstable modes.

Contact calculations are critical in the FEM. In this case, the calculation should be almost impossible, because a smooth surface (pad) comes in contact with an uneven disc surface including even the ventilation holes. Thus, the pad surface comes in contact with many edges and numerically problems occur. Every hole adds several edges which causes problems in the calculation. Nevertheless, because the influence of a improper contact calculation on the brake squeal algorithm should also be evaluated, these calculations are performed.

The result of the CEA shows no unstable frequency, but in the experiments squeal frequencies at 1.89 kHz, 2 kHz and 13.4 kHz could be observed. A first view at the contact apparently shows a plausible contact calculation, see Fig. 3.8.

However, a closer examination shows irregularities in the shear direction of the pads. Consequently, two calculations with a low brake pressure of 8 bar and a comparatively high pressure of 160 bar are performed. The total contact force can be calculated by adding up the contact forces of every node. Figure 3.9 shows the process of the total

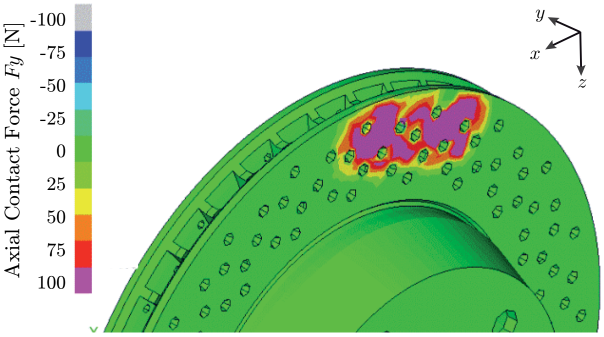

Figure 3.8.: Contact forces in axial direction on the disc, linear tetrahedral elements, friction coefficient equals 0.7.

forces of both sides with respect to the calculation step. It can be seen that, in addition to the expected axial forces (y-direction), there are forces in tangential (x) and radial (z) direction of the pad. Since the calculation is a static one and only axial forces are applied, these shear forces are irrational and obviously numerical computational errors.

Additionally, the sum of forces of the inner and the outer pad is not equal to zero, hence the forces are not symmetric. For high brake pressure (160 bar), these forces are between 2 and 8 % of the force in axial direction, but for low pressure (8 bar), they reach up to 80 % of the axial force. This difference also leads to completely different results in the CEA. As a result, the complex eigenvalues differ significant. It is therefore proven that the wrong contact calculation has an impact on the *black box* calculation of CEA. As expected, the ventilation holes cause numerical problems in the contact calculation which leads to significant differences in the results.

As a result of that wrong contact calculation, simulations with a higher element order are also investigated, but a calculation using quadratic tetrahedral elements shows that only few nodes are in contact. Hence, these calculations cannot deliver correct results and no CEA is performed. As a consequence, the whole disc is remeshed using hexahedral elements. Also the ventilation holes are now neglected, see previously presented Fig. 3.6. Background information about linear and quadratic element order of tetrahedral and hexahedral elements are given in the Appendix, Chap. A.2.

The brake pads including backplate and the brake pistons are also remeshed using hexahedral elements. However, this effort is time-consuming and in daily meshing practice usually omitted due to cost reasons. After remeshing, the force distribution and the total contact forces in all three directions look regular. Figure 3.10 shows the result for a final brake pressure of 160 bar. There are still contact shear forces, but they are almost linearly dependent on the axial contact force and symmetric, hence their sum equals zero. Also their total is less than 3 % of the normal contact force, which is an acceptable numerical calculation error.

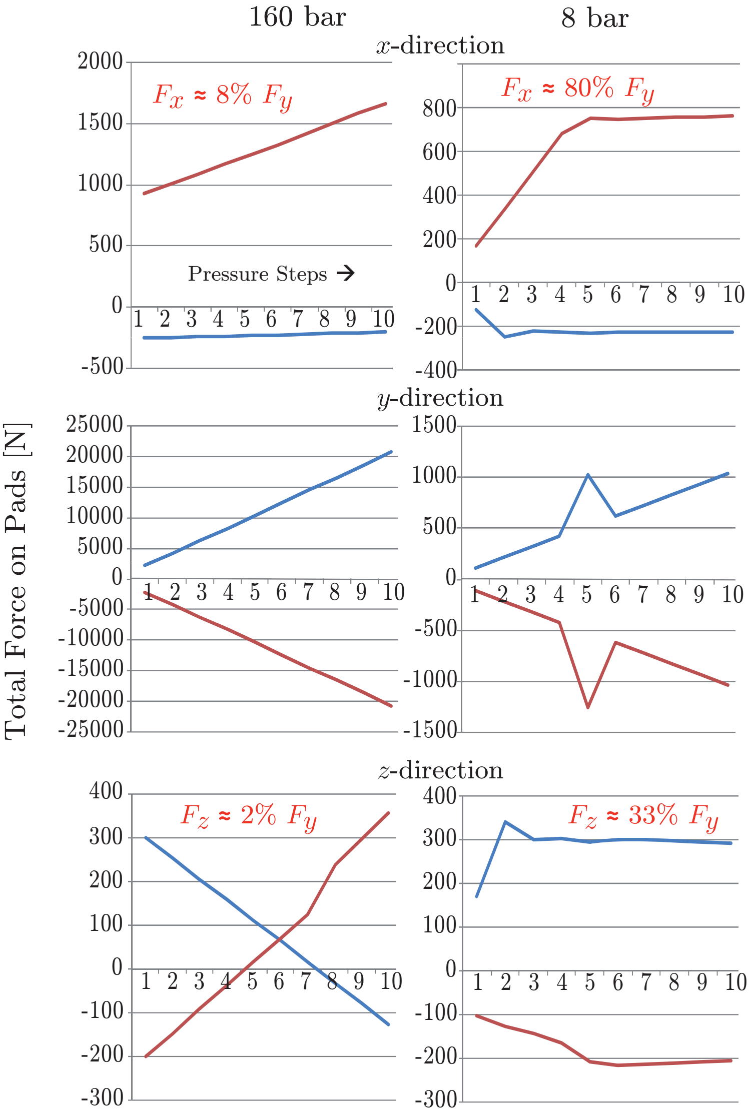

Figure 3.9.: Contact forces in all directions, linear tetrahedral elements, x is equal to tangential direction (shear), y to axial direction, z to radial direction (shear), left column 160 bar and right column 8 bar final pressure. The two depicted lines in each plot represent the inner and the outer pad, friction coefficient equals 0.7.

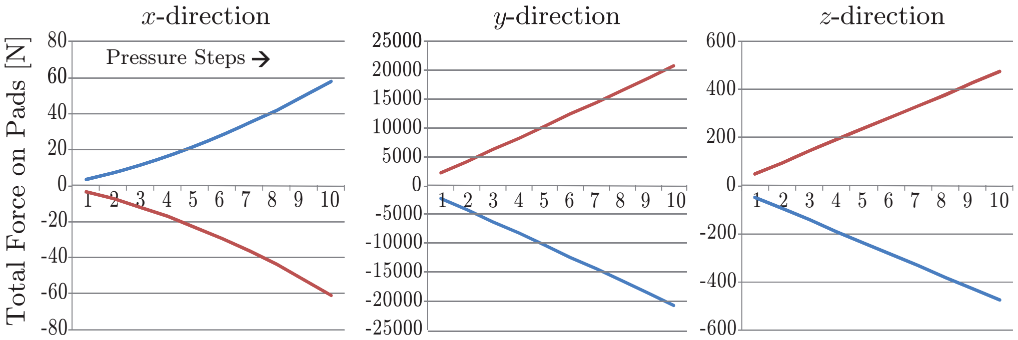

Figure 3.10.: Contact forces in all directions, linear hexahedral elements, 160 bar final pressure, disc without ventilation holes, friction coefficient equals 0.7.

The next step is to evaluate the influence of brake pressure and friction coefficient on the instabilities. As mentioned above, *MD Nastran* delivers as result of the CEA a complex eigenvalue λ and a damping coefficient g as defined in Equ. (3.4) and Equ. (3.6). Figure 3.11 shows the curve shapes of the damping coefficient for varied μ. Observations show that the damping coefficients are constant for small friction coefficients. Increasing the friction results in peaks. During experimental investigations the investigated brake system shows squeal noise at around 2 kHz. In the simulation there are peaks at 1.1 kHz and 2.2 kHz. Together with experimental results, it is now possible to indicate potential instable complex frequencies and the critical friction coefficient which should not be exceeded to avoid these vibrations.

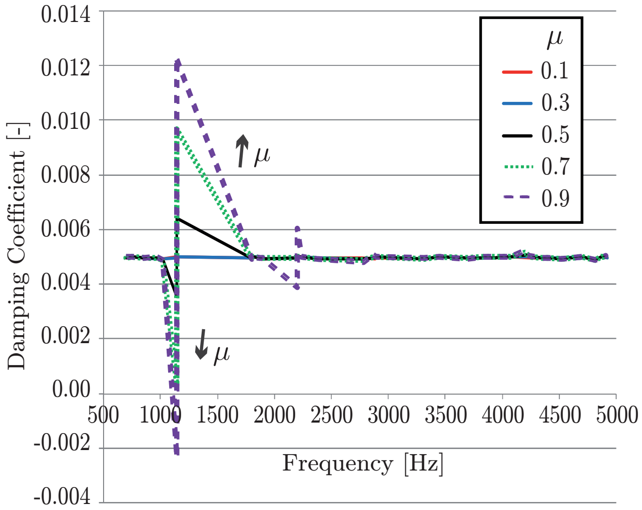

Figure 3.11.: Development damping coefficient for constant brake pressure 10 bar at constant velocity 10 kph, μ varied.

3.2.2. Comparison of Different FEM Systems

Next the results of different FEM systems should be evaluated. In general, the same FEM model calculated with two FEM calculation programs should provide similar results, which is investigated in the following. An overview of all results gained from testing and simulating with *MD Nastran* and *Abaqus* [1] can be found in the Appendix, see Tab. A.4. The performed calculation will be explained step by step in the following.

All the different variants have been simulated twice, once with a final brake pressure of 8 bar and once with 160 bar. Of course, a final brake pressure of 160 bar is very high and almost impossible to reach in reality. Additionally, squeal usually occurs at low brake pressures. Nevertheless, this high value is chosen to evaluate the impact of the brake pressure on the simulations.

The variants are simulated using *MD Nastran* and *Abaqus*. The calculation algorithm of these two software packages are in principle the same: firstly, the brake pressure is applied within ten steps allowing the simulation to determine the pressure distribution in the contact area of brake disc and pad. Secondly, the CEA is performed.

For the calculations, improved meshes using hexahedral elements for the brake piston, brake pad and brake pad backplate are used. The investigations focus on the mesh of the disc which has been varied. Simulations are performed using the detailed tetrahedral element mesh of the brake disc including the ventilation holes and the remeshed brake disc model using hexahedral elements neglecting the ventilation holes.

Figure 3.12 shows two equal colour-shaded plots of the axial contact force distribution calculated with the two software packages. In both plots, areas with high contact forces can be clearly identified. These are the positions of the brake pistons, which act on the pad backplate and furthermore on the brake pad. Overall the two results look quite similar.

Nevertheless, both software systems have got problems in the contact area because of the ventilation holes. However, compared to the previously mentioned calculations the contact is already significantly improved due to the hexahedral element mesh of the pads. For the calculation, the same element order for the disc elements and integration method, which will be considered later, is used.

The brake squeal analysis performed with *Abaqus* delivers a similar output to *MD Nastran*. Table 3.2 shows an exemplary output such as received from *Abaqus*. Again, instabilities are indicated by a positive real part of the eigenvalue and by a negative effective damping ratio. The plot of the effective damping ratio over the complex frequency looks similar to the *MD Nastran* plot (Fig. 3.11). However, the effective damping ratio for stable modes equals zero.

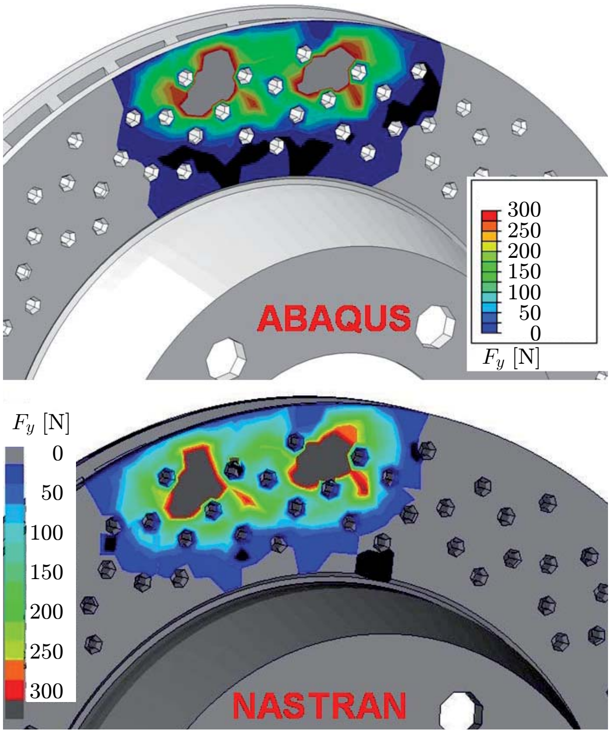

Figure 3.12.: Comparison of the axial contact force distribution for final brake pressure of 160 bar, calculated with *Abaqus* and *MD Nastran*, linear tetrahedral elements, reduced integration, friction coefficient equals 0.7.

Table 3.2.: Example of an *Abaqus* output file, unstable frequency is indicated by a positive real eigenvalue and a negative damping ratio. The unstable frequency is usually one of the double frequencies (marked).

NO	REAL PART OF EIGENVALUE	FREQUENCY		EFFECTIVE DAMPING RATIO
		(RAD/TIME)	(CYCLES/TIME)	
44	0	42953	6836.2	0
45	0	43140	6865.9	0
46	**-275.75**	**45658**	**7266.7**	**0.01208**
47	**275.75**	**45658**	**7266.7**	**-0.01208**
48	$7.52 \cdot 10^{-09}$	46673	7428.3	0
49	$-8.17 \cdot 10^{-09}$	47065	7490.7	0
50	$2.25 \cdot 10^{-07}$	48088	7653.4	0

The next step is a comparison of the contact calculation and the results of the CEA using the two different FEM software packages and the four different element types (two different meshes and element orders). To evaluate the pressure influence, the calculations are performed with an applied brake pressure of 8 bar and 160 bar. Additionally, the calculation in *Abaqus* is performed twice, once with full and once with reduced integration. All results are collected in four tables in the Appendix (Chap. A.2: Tab. A.1, Tab. A.2, Tab. A.3, Tab. A.4). The tables show the result of the CEA, hence the calculated complex frequencies. Unstable modes or double frequencies, respectively, are highlighted.

Because FEM solves essentially differential equations, a key step in the calculation is the definition of an appropriate deformation approach by means of an spatial numerical integration over the elements. As long as no integration points are a priori defined, the *Gaussian quadrature*[3] is the optimal method with the smallest possible integration error for a given number of integration points n.

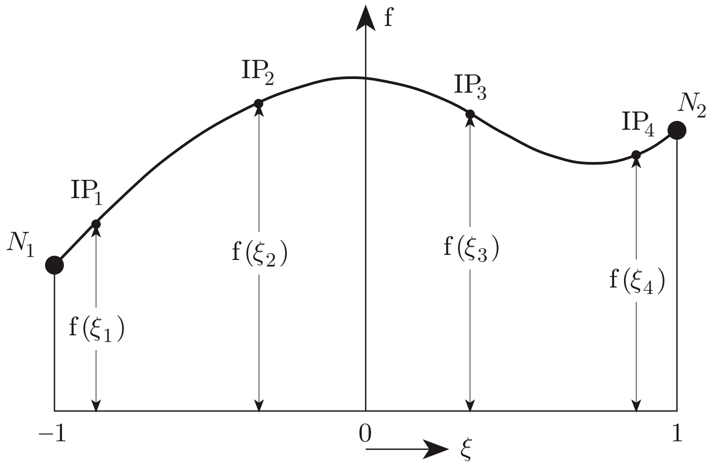

Figure 3.13.: One dimensional *Gauss-Legendre* integration of a function f(ξ).

Further theoretical considerations are taken for the one-dimensional case. Figure 3.13 depicts the function to be integrated f(ξ), the nodes of the element N_i and the integration points IP$_i$. The function f(ξ) is separated into a weight-function w(ξ) and a function g(ξ) as given by

$$\int_{-1}^{1} \mathrm{f}(\xi)\mathrm{d}\xi = \int_{-1}^{1} \mathrm{g}(\xi)\mathrm{w}(\xi)\mathrm{d}\xi \approx \int_{-1}^{1} \mathrm{p}_n(\xi)\mathrm{w}(\xi)\mathrm{d}\xi = \sum_{i=1}^{n} \mathrm{g}(\xi_i)\mathrm{w}_i, \tag{3.7}$$

where g(ξ) is approximated by a special polynomial p$_n$(ξ) with the integration points ξ_i defined by the *Gaussian quadrature*. The quadrature rule is constructed to deliver an exact result for polynomials of degree $2n-1$ if suitable integration points and weights

---

[3] The exact term is *Gauss-Legendre quadrature*.

can be chosen. The integration domain is conventionally taken as $[-1, 1]$. The weight-function w_i at the integration points reads

$$\mathrm{w}_i = \int_{-1}^{1} \mathrm{w}(\xi) \prod_{j=1, j \neq i}^{n} \frac{\xi - \xi_j}{\xi_i - \xi_j} \mathrm{d}\xi \qquad i = 1, ..., n. \tag{3.8}$$

To obtain optimal integration accuracy, the integration points ξ_i of the *Gaussian quadrature* of degree n have to be equal to the zero-points of the n^{th} orthogonal polynomial p_n. Additionally, the polynomials $\mathrm{p}_1, ...\mathrm{p}_n$ must be orthogonal to the with $\mathrm{w}(\xi)$ weighted scalar product (which is expressed by a *Kronecker delta* δ_{ij}):

$$\delta_{ij} = \langle \mathrm{p}_i, \mathrm{p}_j \rangle_{\mathrm{w}} := \int_{-1}^{1} \mathrm{p}_i(\xi)\mathrm{p}_j(\xi)\mathrm{w}(\xi)\mathrm{d}\xi. \tag{3.9}$$

The main and most important form of the *Gaussian quadrature* is the *Gauss-Legendre quadrature*. Usually this form is meant when referring to the *Gaussian quadrature*. In this case $\mathrm{w}(\xi) = 1$ applies. The resulting orthogonal polynomials are *Legrendre-Polynomials* [20, 114, 171].

Using the *2x2x2 Gaussian quadrature* on a linear hexahedral element ("brick element", *Hexa8*) results in eight integration points, see Fig. 3.14 left. For bending application or modal analysis, these elements may appear to stiff because a numerical problem called *shear locking* can occur if the mesh is too coarse. Using only one integration point, hence reduced integration, solves this problem but increases the numerical error of the integration. Figure 3.14 right shows such an element. However, due to the reduction to one integration point, an other numerical problem called *hourglassing* may occur [114].

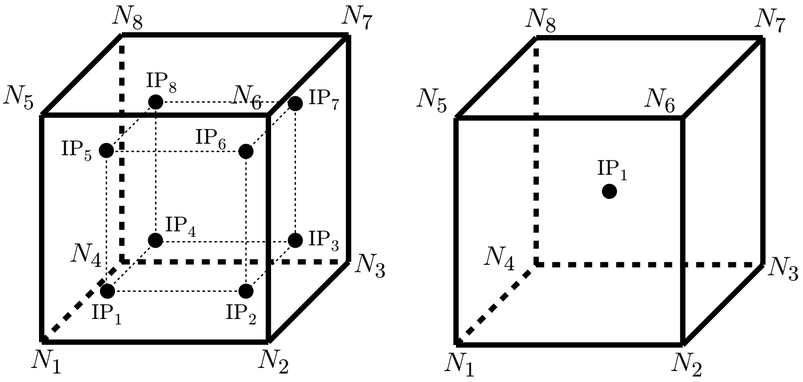

Figure 3.14.: Element nodes N_i and integration points IP_j of a linear hexahedral element, left full integration, right reduced integration. Adapted from [155].

Figure 3.15 presents the shape change of a *Hexa8* which is stressed by a torque T. Figure 3.15 a) shows the unstressed element and b) the deformation as it would be in reality. Thereby, the angle α remains 90 degrees, but the edges of a *Hexa8* full integrated element are not able to bend to curves. Consequently, the angle α has to change. This introduces an incorrect artificial shear stress. Thus, not a bending deformation but a shear deformation generates out of the strain energy. As a result, the linear full integrated element is overly stiff and becomes locked, see Fig. 3.15 c). Also the edges of the reduced integrated element cannot bend to curves, but the angle α remains at 90 degrees and no artificial shear stress is introduced, see Fig. 3.15 d). The best results for bending and modal analysis are gained using quadratic elements (*Hexa20*) and full integration. Now the edges are able to bend and the angle α is correct [155].

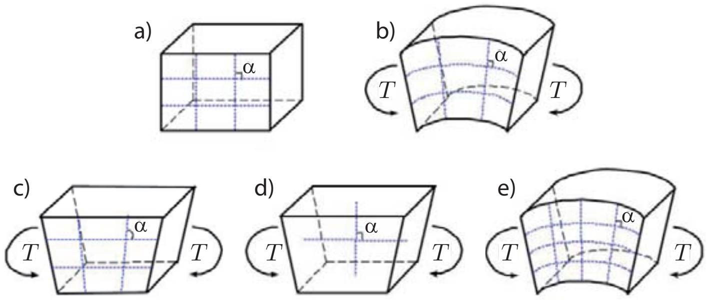

Figure 3.15.: Shear locking effect: a) unstressed element, b) shape change in reality, c) shape change of full integrated linear element, d) shape change of reduced integration linear element, e) shape change of full integrated quadratic element, adapted from [155].

The reduced integration has some advantages. It reduces computational time and therefore costs. As discussed above, it prevents shear locking. However, there are also some disadvantages. It is possible that the element has deformative modes, which are not resited by the element. The element appears to soft.

This phenomenon was first noticed in the 1960s. Because of their shape, they are historically called *hourglass* modes. Figure 3.16 shows the deformative modes of a four-node element. Thereby, E_ξ and E_η represent the expansion modes in ξ and η direction, $S_{\xi\eta}$ the shear mode, H_ξ and H_η the hourglass modes. Due to the single integration point the deformation of the hourglass modes results in no deformation energy. Consequently, they are also called *zero energy* modes. Further details on *shear locking* and *hourglassing* can be found in [20, 21, 104, 105, 114, 155].

Table A.1 in the appendix presents the results using *Abaqus* reduced integration taken into account a friction coefficient equal 0.7. Comparing the results of the same element types for different applied brake pressure shows that there is hardly any pressure influence on the calculated complex frequencies. The maximum observed frequency shift is 4 Hz. Also the unstable modes are more or less equal for high and low pressure. There is only one instability missing at approximately 1.8 kHz using *Tetra10* elements and

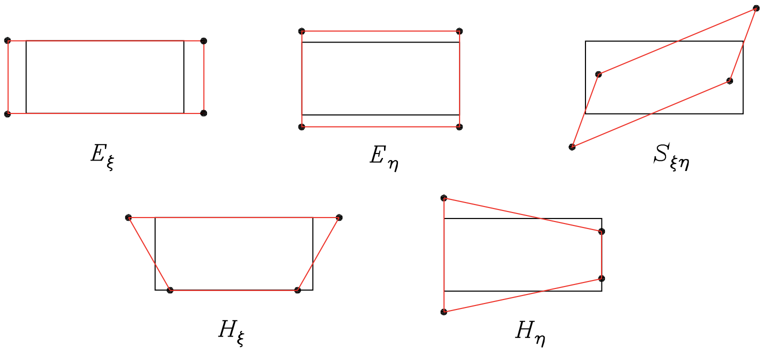

Figure 3.16.: Linear deformative modes of a four-node element[104].

8 bar brake pressure. However, a closer look into the table shows that there are two quite similar frequencies in the *Tetra10* 8 bar column in that frequency range. Hence, at 8 bar these almost double frequencies are on the verge of being unstable. Comparing the results for different element types shows that there are great differences.

In particular, the *Tetra4* elements are too stiff: the first instability is quite high at 2270 Hz. Using *Tetra10* elements the first (near) instability is already at 1804 Hz. The first calculations using *Tetra10*, *Hexa8* and *Hexa20* elements predict already approximately the two measured instabilities around 2 kHz. Most instabilities are found using the *Hexa20* elements.

Table A.2 shows the results using *Abaqus* full integration. For modal analysis using first order brick elements (*Hexa8*), this integration may be inappropriate because of the previously explained *shear locking* effect. There are no instabilities found for the calculation using *Hexa8* elements. At least there are three almost double frequencies which are on the verge of being unstable. Thus, it could be proved that fully integrated *Hexa8* elements are overly stiff because of the previously mentioned introduced incorrect artificial shear stress. Therefore, many instabilities vanish if the integration type is changed from reduced to full integration using linear elements.

Finally, Tab. A.3 presents the results for calculations using *MD Nastran*. CEA results with quadratic hexahedral elements are missing because this type of calculation is not possible with *MD Nastran*. Additionally, the CEA can only be calculated using reduced integration. It can be observed that the results of the *Tetra10* element runs are independent of the brake pressure. However, calculation with *Tetra4* and *Hexa8* elements shows significant pressure influence: due to the brake pressure some instabilities vanish, others are shifted in their frequency range and even some new unstable vibrations occur.

A complete overview is provided by Tab. A.4. On road-testing and on the test rig, squealing operation points between 9 bar and 16 bar are observed. In the experiments two main squealing frequencies at 1890 Hz and 2000 Hz were found to be dominant.

The results of the different simulations vary significantly. Some of the deviations can be explained by the improper contact definition. Hence, the contact analysis in *MD Nastran* is investigated in detail.

3.2.3. Contact Analysis in MD Nastran

To analyse the contact, the disc is modelled by linear hexahedral elements (*Hexa8*) and reduced integration is used. The reason for that is as mentioned above that this element type usually provides good results in modal analysis which could only partially be observed at the previously performed calculations. For the investigation, three different mesh types are used:

1. Basic mesh disc with basic mesh pad, about 800 pad nodes in the contact area.
2. Basic mesh disc with refined mesh pad, about 3000 pad nodes in the contact area.
3. Coincident mesh disc and pad, about 900 coincident nodes in contact area.

The refined pad mesh is achieved by splitting the basic mesh of the pad. Every hexahedral element has been replaced by eight hexahedral elements. In order to obtain the coincident mesh, it is necessary to change the mesh of the disc marginally.

The pad mesh has to be completely remeshed and additionally the geometric shape of the pad is simplified regarding the cut out at the outer radius. Figure 3.17(a) and Fig. 3.17(b) show the results for the performed contact calculations using a final brake pressure of 16 bar and a friction coefficient of 0.4. These values are observed on the test rig during squeal at a frequency around 2 kHz.

For better comparability of the Fig. 3.17(a) and Fig. 3.17(b), the colourmaps are coloured equally. It can be seen that the force distribution on the disc has got similarities. Of course, the distribution in the coincident mesh case looks smoother, but the force distribution of the pad changes significantly. The percentage of nodes which are in contact is about 60 % in case of the basic model. In the refined model, only approximately 40 % of the nodes are included in the contact. The best result can be obtained with the coincident mesh. There, about 95 % of the nodes are in contact.

The disadvantage of the coincident mesh is that now negative axial contact forces and shear forces occur at the edges of the contact area. These forces have an order of magnitude of up to 40 % of the maximal axial contact force. Figure 3.18 shows the visualised size and direction vectors of the contact force at the disc. Additionally, Fig. 3.19 shows a zoom of one relevant area. The contact force vectors of the pad look the same, but are of course inverted because of Newton's third law of motion[4].

---

[4] ”Actio est reactio”.

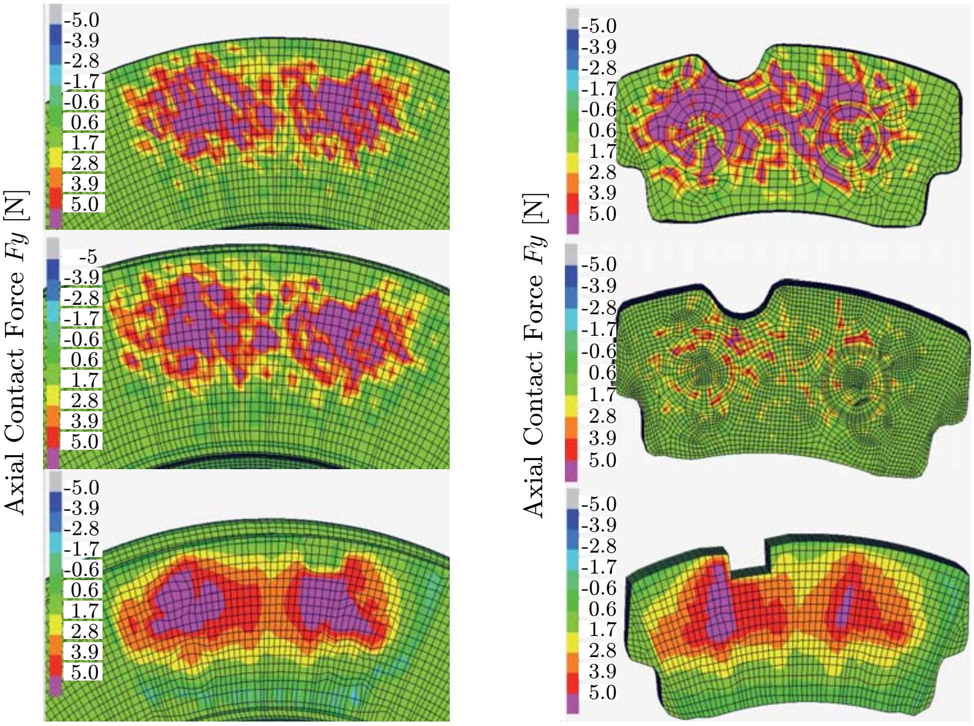

(a) Disc

(b) Pad

Figure 3.17.: Contact force distribution comparing basic mesh (upper) with pad refined mesh (middle) and mesh with coincident nodes (lower), final brake pressure 16 bar, friction coefficient equals 0.4.

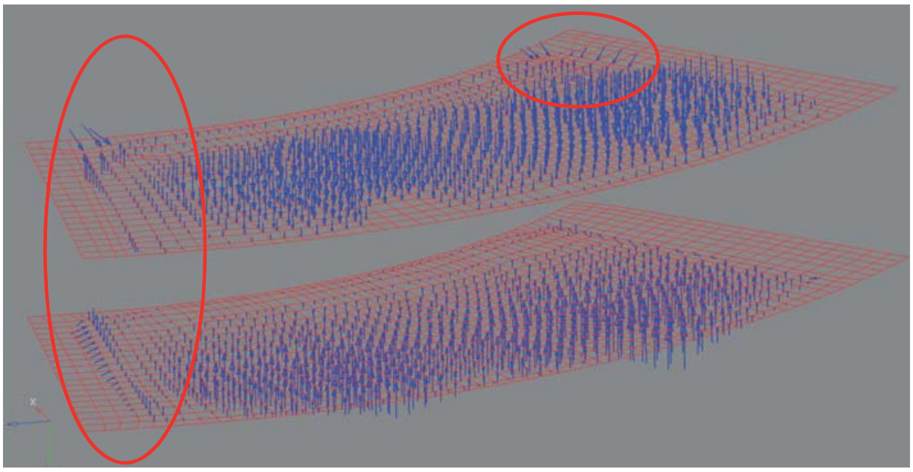

Figure 3.18.: Irregular contact force vectors for calculation using coincident brake pad/brake disc mesh, final brake pressure 16 bar, friction coefficient equals 0.4.

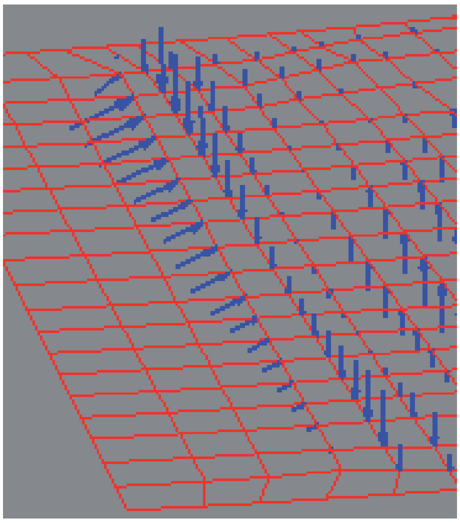

Figure 3.19.: Zoom of lower left area of Fig. 3.18.

The differences in the contact calculation lead to varying inputs in the previously mentioned skew-symmetric stiffness matrix $\mathbf{K}_F$, and this variation leads furthermore to differences in the results of the CEA. Figure 3.20 shows the results for the damping coefficient over the complex frequency for the three different meshes. Thereby, two differences can be observed:

1. Calculations with all three mesh types always show a critical frequency at about 1.9 kHz. They are marked with a circle in Fig. 3.20. From experiments, critical frequencies at around 1.9 kHz and 2 kHz are known. The magnitude of the (negative) peak indicates which unstable frequencies are first detected due to the CEA. Increasing the friction coefficient leads to a negative damping and consequently to a predicted instability (Fig. 3.11). As a result of the mesh refinement (upper and middle diagram in Fig. 3.20), the 2 kHz peak is reduced, but using the coincident mesh leads to the highest peak, even higher than the other calculated critical frequencies which could not be observed during the experiments. Thus, the prediction of the first vibration, which becomes unstable, seems to be correct if the coincident mesh is used.

2. Comparing the overall curve shape of the damping coefficient it can be seen, that the other values are not affected due to the variation of the mesh in the contact area. As a result, a variation of the contact mesh can be used to detect vibration modes of the system which are highly dependent on the contact. A squealing brake system is always excited by the contact and the mode shape of the squealing vibration depends on the contact. Consequently, the contact depending vibration modes are more important than the non contact depending vibrations modes. Such by using this method, the two kinds of vibration modes could be separated.

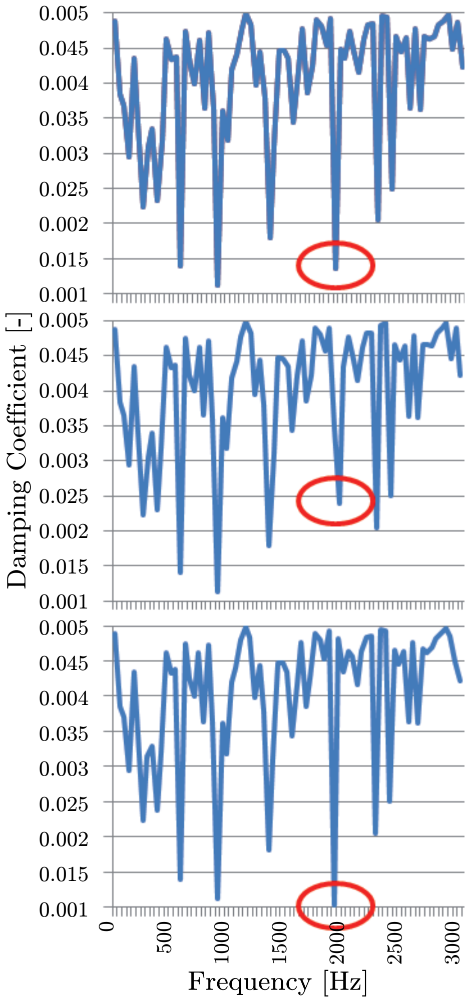

Figure 3.20.: Comparison damping coefficient for basic mesh (upper), refined mesh (middle) and coincident node mesh (lower), final brake pressure 16 bar, friction coefficient equals 0.4.

3.3. Discussion

The main method to investigate brake squeal using the FEM is the CEA. However, there are several problems when using the CEA for brake squeal prediction:

Overestimation: The CEA delivers numerous possible unstable frequencies, but only a few of them can be observed on the system in reality. Therefore, additionally experiments are necessary to determine the relevant critical frequencies and the ODS. After successful correlation of experiments and calculation, counter-measures can be developed virtually.

Limit Cycle: An instability is detected due to a negative damping coefficient, but the extent of the negative damping correlates only with the amplification rate of the system. This means that this value does not allow statements to be made relating to the reached limit cycle of the system which equals the emitted sound intensity. A calculated critical vibration with a high amplification rate may reach only a low limit cycle and no squeal can be detected. A brake squeal vibration, which increases gently, but steadily and reaches a high limit cycle, has only a low amplification rate, hence a small negative damping value, but it is much more critical. This is explained in Chap. 2, see also Fig. 2.14. The CEA delivers all frequencies, which have the *Ability* of being unstable. The experiments deliver the real *Behaviour* of the system[5].

The previously presented results show the importance of a proper contact calculation and the great influence on the subsequent performed CEA. A better contact calculation may also reduce the gap between *Ability* and *Behaviour*. Using the last state of the FEM model, hence linear hexahedral elements, reduced integration, coincident nodes in the contact area, leads to a predicted instability at 1.9 kHz. Figure 3.21 shows the determined mode shape of the brake system.

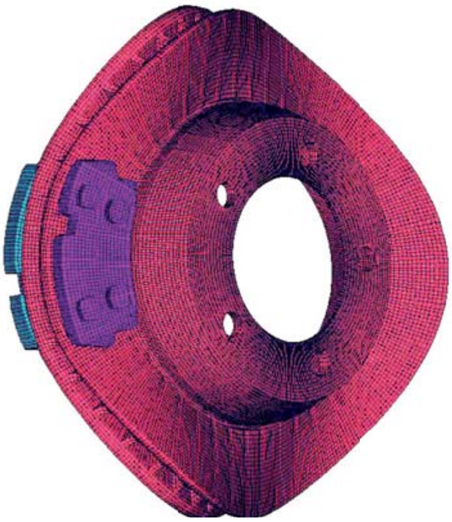

Figure 3.21.: Calculated ODS of the unstable frequency at 1.9 kHz.

Thereby, the disc vibrates in a so-called (0,3) ODS which is depicted in Fig. 3.22. Hence, there are no nodal circles and three nodal diameters. The brake pads vibrate in phase with the disc surface. Subsequently performed experimental investigations on the test rig show that the predicted mode shapes are exactly the ODS of the brake system during a squeal event. Thus, the principal suitability of the FEM regarding brake squeal prediction is investigated. Several advantages and disadvantages of the method

---

[5] The terms *Ability* and *Behaviour* are adapted from [107].

as well as weak points in the calculation method could be determined. The findings of the investigation are used for the design of a proper brake system development process, see Chap. 6.

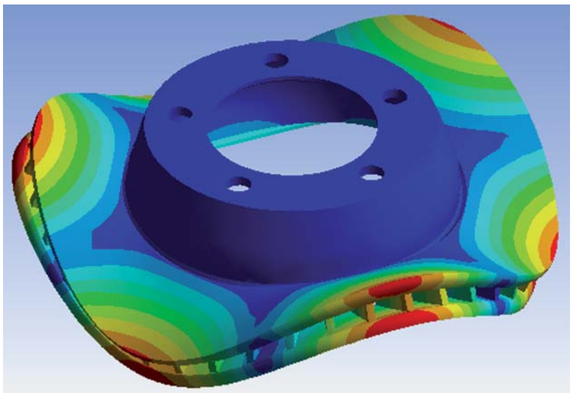

Figure 3.22.: Calculated disc mode shape (0,3) at 1.9 kHz.

4. Experimental Analyses

4.1. Literature Review

4.1.1. Test Benches and Methods

Vibrations in brake system have been investigated for many years. Already in 1938 Mills [115] conducted experiments on squealing drum brakes. One of the main results of the work was that the friction coefficient of squealing brake systems decreases with increasing velocity. The experimental works done until today fall in two broad classes:

Matrix Test Series: This kind of test is mainly carried out in industrial research and development. Thereby, the brake system is tested under various conditions. For example, the SAE J2521 (*Disc and Drum Brake Dynamometer Squeal Noise Matrix* [143]) is such a test which consists in total of 2321 brake applications. Thereby, velocity, brake pressure, temperature of the brake system as well as the direction of rotation are varied. Sound pressure and frequency of the squealing noise are measured with a single microphone. The result is a *Squeal Noise Matrix* (SNO) which provides a good overview of critical operating conditions of the brake system including information on *Sound Pressure Level* (SPL) and squeal frequency. The resulting *Squeal Noise Occurrence* (SNO) value is a suitable parameter to compare different brake systems.
Current research work is focused on a better repeatability and reduction of the variability of the tests [3, 70, 71]. To increase the comparability of the test benches and to facilitate the data exchange, the *Universal Brake Test Data Exchange Format* has been developed [23].

In-depth Investigation: In order to understand the underlaying physical processes, simplified brake systems are mounted on test benches to perform in-depth investigations or existing brake systems are investigated in detail using complex measurement systems. This is contrary to describing the effects of the physical processes as done by the matrix test series.
Dunlap et al. [46] performed parameter studies regarding brake discs stiffness and brake pads geometry. Butlin and Woodhouse [28, 29] performed sensitivity analyses regarding material characteristics and pad stiffness. Eriksson et al. [24, 49, 50, 51] investigated the influence of pad surface and humidity on squeal generation.
Ramasami et al. [141] used a simplified brake system. It consists of a simple U-shaped fixed caliper which presses two circular shaped pads against the brake disc.

This model is similar to double pin-disc models such as that developed by Earles [47]. Many research groups use simple pin-on-disc (or beam-on-disc) test set-ups [13, 15, 30, 48, 68, 93, 109, 110, 129, 148, 161], which allows a straightforward comparison with analytical or simple FEM models.

4.1.2. Brake Squeal Measurement Systems

Several measurement methods were developed to investigate brake squeal and its influencing parameters. Important parameters cannot be measured directly. Models are needed to extract them mathematically from the measurements.

One good parameter example is the friction coefficient μ of the brake system. In most of the standards for brake system testing, such as the SAE J2521 standard, this value is calculated using two measured signals (brake torque T_B and brake pressure p_{hyd}), one well-known geometrical factor (piston area A_B), one uncertain estimated value (the effective radius r_{eff}) and the brake efficiency η_B. The brake efficiency has been determined experimentally and is defined to $\eta_B = 95\,\%$ for floating caliper and to $\eta_B = 98\,\%$ for fixed caliper brakes [41]. In addition, it is assumed that the conditions for the two brake pads on either side are equal. Thus, the friction coefficient regarding the SAE J2521 standard [143] reads

$$\mu = \frac{T_B}{2(p_{\text{hyd}} - p_{\text{TH}})A_B r_{\text{eff}} \eta_B}, \tag{4.1}$$

where the brake pressure p_{hyd} declares the applied braking pressure which is multiplied by the area of the brake pistons A_B to obtain the acting normal force F_N. Multiplying this with the friction coefficient gives the friction force. This force acts at a certain effective radius r_{eff} and results in a calculated braking torque. By equating the calculated braking torque with the measured braking torque T_B, the friction coefficient is calculated. The calculated braking torque is additionally reduced by the level of efficiency η_B of the brake system. Furthermore, the threshold pressure p_{TH} is necessary to get above the reset force of the brake piston seals and therefore reduces the applied brake pressure. Regarding the SAE J2521 standard p_{TH} equals 0.5 bar.

Figure 4.1 shows a drawing of the system geometry. The effective radius r_{eff} is the distance from the centre C of the disc to the resulting friction force F_F. This acting point of F_F is usually unknown and due to this defined as centroid of the contact area [143]. The schematic depiction shows a two piston brake caliper. The piston area A_B is given by the sum of A_1 and A_2. Additionally, the inner r_I and the outer r_O radius of the brake pad are shown.

Degenstein and Fritzen [41] discussed this determination of the friction value and showed the limitations of this industrial measurement standard. For one friction combination, the measured (or rather calculated) coefficient of friction varies about ±5 %. To reduce this scattering, Dohle et al. [45] developed a measurement system for a floating

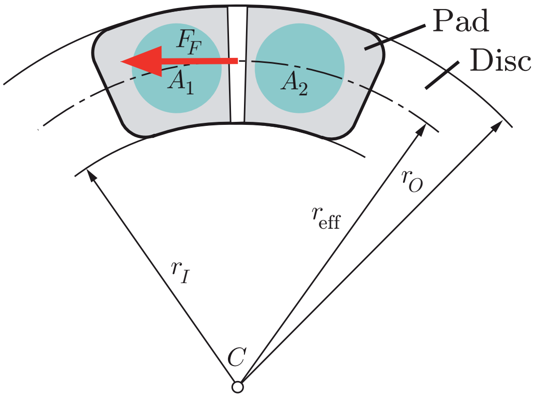

Figure 4.1.: Schematic depiction of the geometry in brake systems.

caliper brake: The friction forces are measured directly at the pad using a uniaxial force transducer. However, for the sensor implementation, it is necessary to break up the pull-push principle of the pin and to remove the pad springs. Thereby the brake system is changed significantly. Nevertheless, the variation of the measured friction coefficient could be reduced.

In addition to the friction coefficient μ also the effective radius of the friction force r_{eff} is an uncertain system parameter. Degenstein and Winner [40, 42, 43] developed a system to investigate the position of this radius. Thereby, a brake pad surface is split into four areas and below each area one slim-line piezo quartz sensor is integrated to measure the acting normal force of each area. Thus, their so-called *point of application of the load* applied by the brake pressure can be determined. Under the assumption of a constant friction coefficient, this point equals the acting point of the resulting friction force, hence r_{eff}. It can be proved that the point of application of load shifts several millimetres[1] when the braking pressure rises from 10 to 60 bar.

Also the research group around Fieldhouse investigated r_{eff} and their so-called *Centre of Pressure* (CoP) of a brake pad during a braking operation. The influence of that point on brake squeal is also studied [54, 55, 56, 58, 59]. To measure the pressure distribution at dynamic conditions, a pressure sensitive film is bound to the metal of the support plate. The sensitive film laminate is sandwiched between the friction material and the backplate of the pad. The influence of different pad abutments and application of the brake force, which was simulated by varying the contact position of piston/pad, was analysed. A small variation of the CoP during a squealing brake application, e.g. performed by gently pressing a screwdriver against the pad, can lead to a complete squeal suppression.

---

[1] Maximum measured shift equals 17 mm.

Another approach is developed for measuring the normal force between pad and pistons [74, 75, 82, 83, 92, 146, 147]. Thereby, two piezo sensors are installed at the backplate of the brake pads. Consequently, also active squeal suppression is possible. Thereby, one piezo acts as a sensor and the other as an actuator.

Beside investigations on the friction coefficient and the pad vibration, the *Operational Deflection Shape* (ODS) of the brake disc is also of interest. Thereby, it has to be noted that the squealing brake disc usually vibrates near a natural frequency and the deflection shape is steady with respect to the caliper. Hence, the vibration diameters[2] of the disc do not move with respect to the caliper. The three most commonly discussed and presented methods for measuring the ODS are:

Double-pulsed Holographic Interferometry: This optical measurement technique enables the measurement of static and dynamic displacements. The obtained images include fringe lines and therefore give detailed information on the vibration mode of the disc [57, 59, 156, 157].

Three Dimensional Scanning Vibrometer: Three two dimensional scanning vibrometers are necessary for this laser measurement technique. The system scans a given number of points on the rotating surface and evaluates the velocity of these points in all three directions [22, 61, 116].

Accelerometers: If ventilated brake discs are investigated, miniature acceleration sensors can be installed in the cooling ducts of the disc. Because of the, from an external point of view, steady disc vibration, the sensor ”scans” the ODS at every rotation. A big advantage to the previously mentioned optical and laser methods is that the ODS also in the contact area of the disc, hence below the brake caliper, can be measured [108].

Another possibility to measure the brake disc deflection are capacitive sensors. Ouyang et al. [131] used twelve capacitive sensors arranged tangentially around the brake disc at one radius and thus determined the ODS of the disc. Sarda et al. [145] used five capacitive sensors along the radial direction of the disc. However, this measurement system is used for the detection of hot spots on the brake disc which causes brake judder, and not for ODS measurement.

4.2. Developed Measuring System

As already mentioned, fixed caliper brake systems are more complex and thus more expensive than floating caliper brake systems, but they perform better in respect of braking. Due to this, they are used e.g. in expensive sport cars. However, exactly the customers of such cars are not willing to accept noisy brakes. In addition, all the previously presented measuring systems are implemented on floating caliper brake systems

---

[2] A vibrating beam has vibration nodes, a vibrating disc vibration circles and vibration diameters. These are the positions of the nodes of the standing waves.

or on simplified models of a fixed caliper brake system. These considerations lead to the decision to investigate a fixed caliper brake system in the present work.

Table 4.1 presents an overview of the demanded measurement results, the sensors used and the location of these sensors. A microphone measures the emitted noise of the brake system. The ODS of investigated parts is usually determined using acceleration sensors. To measure the ODS of the brake disc, three *Triaxial Acceleration Sensors* (TAS) are installed in the brake disc cooling ducts. Three displacement measuring *Eddy Current Sensors* (ECS) and two additional installed TASs determine the ODS of the outer brake pad. Two further TASs measure the vibration of the brake caliper.

Table 4.1.: Overview on the demanded measurement results, therefore required sensors and location of them.

SUBJECT	**SENSOR**	**LOCATION**
noise measurement	microphone	near Disc
ODS disc	three TASs	disc
ODS pad	two TASs	outer pad
ODS pad	three ECSs	caliper
vibration of caliper	two TASs	caliper
resulting friction force	strain gauges	guide pin (caliper)
pad shear strain	strain gauges	pads
disc revolution angle	incremental encoder	drive shaft
revolution impulse	incremental encoder	drive shaft
rotating speed	incremental encoder	drive shaft
torque	torque measuring sensor	drive shaft
brake pressure	pressure sensor	brake line
temperature disc	three thermocouples	disc
temperature pad	two thermocouples	pads
air temperature	thermometer	test bench ventilation
air humidity	hygrometer	test bench ventilation

The guide pins at the trailing edge, which hold the pads in position during braking, are replaced by modified guide pins. These are equipped with strain gauges to measure the friction force. Strain gauges are also mounted on the side of both brake pads to measure the shear strain. An incremental encoder measures the current revolution angle of the disc. The differentiation of this signal gives the rotating speed. Furthermore, the incremental encoder provides an impulse every rotation.

The used acceleration sensors limit the maximum temperature of the brake disc. To avoid heat damage of those sensors, several thermocouples are installed in the brake disc next to the sensors. In addition, two thermocouples are installed one millimetre below the disc surface at different radii to measure the brake disc temperature close to the friction area. Figure 4.2 shows these thermocouples. The brake pads are also equipped with thermocouples.

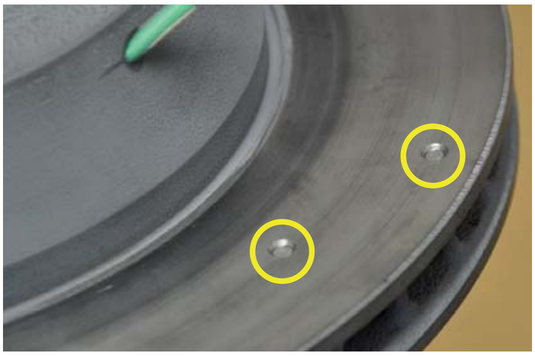

Figure 4.2.: Thermocouples at the brake disc friction surface.

A torque measuring drive shaft measures the acting torque. The brake pressure is measured in the brake line just before it is connected to the caliper. Finally, the test bench ventilation air temperature and humidity is recorded.

The friction force measuring pins and the shear strain measurements are based on strain gauges. Due to this, the suitability of strain gauges for dynamic measurements and their limitations are discussed in the following.

4.2.1. Background Strain Gauges

A reason for the application of strain gauges is, that they have hardly any retroactive effects on the measured characteristics of an object. For dynamic measurements, strain gauges are highly suitable because the transformation from a measured elongation into an electrical resistance takes place with insignificant delay. Several research studies have been conducted to estimate the limit frequency of strain gauges:

In 1950 Fink [60] investigated the results of measured shock waves in cylindrical bars and compared them with analytically calculated values. He estimated that the measuring ability for strain gauges is at least 50 kHz.

Another investigation was performed by Bagaria and Sharpe [18]. They presented the correlation of the expected measurement error and the ratio of strain gauge length L_{SG} to the wavelength λ of the measured signal. Figure 4.3 shows the results of these measurements. Thereby, measurements of repeating shock waves produced by a pendulum ram impact test machine are performed. By measuring a sinusoidal process, the worst case is that the ratio L_{SG}/λ is equal to one, because in that case the strain gauge delivers the value zero. Thus, the ratio L_{SG}/λ influences the accuracy with which the process is reproduced significant.

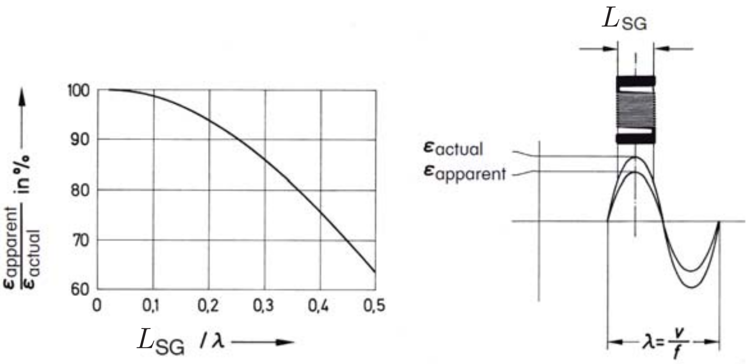

Figure 4.3.: Sensitivity reduction in relation to the ratio L_{SG}/λ for sinusoidal process. The measuring grid centre is located at the point of maximum strain [84].

The used strain gauges on the pin have a length of 1.5 mm and the pin is made of steel. Its Young's modulus $Y = 2.1 \cdot 10^{11}\,\mathrm{N/m^2}$, density $\rho = 7800\,\mathrm{kg/m^3}$ and Poisson's ratio $\nu = 0.3$ are known. The wave propagation speed, hence the speed of sound v in solids in longitudinal direction, is given by [99]

$$v = \sqrt{\frac{Y(1-\nu)}{\rho(1+\nu)(1-2\nu)}}. \tag{4.2}$$

For long rods the simplified equation holds:

$$v = \sqrt{\frac{Y}{\rho}}. \tag{4.3}$$

The physical correlation of wavelength λ, wave propagation speed v and the frequency f reads

$$\lambda = \frac{v}{f}. \tag{4.4}$$

Regarding Fig. 4.3 a ratio of $L_{\mathrm{SG}}/\lambda = 0.1$ results in a measurement error of approximately 2 %. A combination of this ratio and Equ. (4.3) and Equ. (4.4) results in

$$f_{\mathrm{CO}} = \frac{v}{\lambda} = \frac{\sqrt{\frac{Y}{\rho}}}{\frac{L_{\mathrm{SG}}}{0.1}}, \tag{4.5}$$

where the limit or cut-off frequency f_{CO} of the strain gauges is defined as a function of the measurement error. For the pins the calculated cut-off frequency for an allowed measurement error of 2 % equals 346 kHz. This highlights the fact that strain gauges are well suited for dynamic measurements up to high frequencies.

The following sections present the development of the strain gauge based friction force measuring pin and the shear strain measurement. In addition, the other measurement requirements and the therefore necessary sensors and mounting positions are discussed in detail.

4.2.2. Strain Gauge Based Measurement Devices

Friction Force Measuring Pin

One aim of the installed measurement system is to measure the resulting friction force as close as possible to the contact area. Therefore, the guide pins at the trailing edge of the caliper, which holds the pads in position, are replaced by shear force measuring pins. Figure 4.4 shows one of these pins mounted in the caliper and the strain gauges mounted at the pin for measuring.

Figure 4.4.: Modified guide pin for friction force measurement.

A CAD depiction of the location of this pin is presented in Fig. 4.5. In addition, Fig. A.7 in the Appendix shows the technical drawing of this pin. In contrast to the previously explained methods, this sensor measures directly the friction force up to high frequencies and in a high resolution.

Additionally, the modifications in the system have to be as small as possible in order to minimise their influence on the dynamics of the system. Due to this, strain gauges are used and they require a slight modification in the pin shape to mount them. The cross-section of the pin in the area of the strain gauges is shaped like an I-beam. This design leads to a greater shear strain and therefore enhances the measurement signal [84]. Figure 4.6 shows a principle depiction of such a pin.

The I-shape design leads to greater shear stress τ at the strain gauges. Additionally, the arrangement of this strain gauge results in a force measuring signal which is independent from the point of application of the measured force F by means of bending

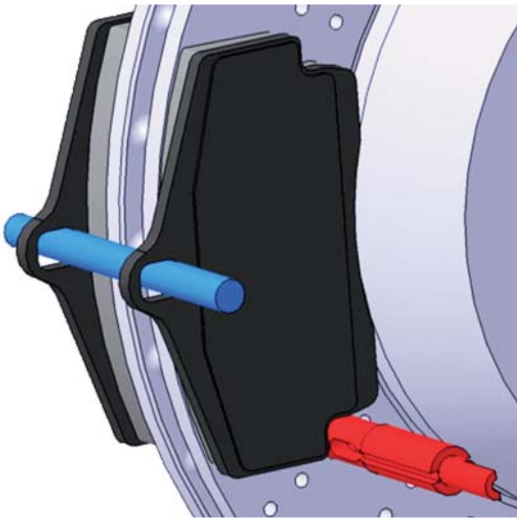

Figure 4.5.: CAD depiction friction force measuring pin.

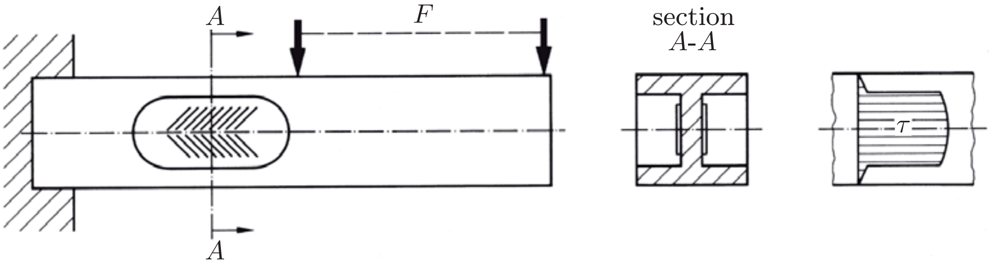

Figure 4.6.: Principle of a shear force measuring pin [84].

stress compensation. Using a second strain gauge on the other side of the pin, a full bridge circuit interconnection can be used for thermal drift compensation. Thereby, it is assumed that the strain gauges on one pin have the same temperature due to thermal radiation and heat conduction.

The friction force measuring pin can only measure the force in one direction. As a consequence, the orientation of the pin has to be considered in detail. Figure 4.7 depicts the acting forces and geometrical information of a general brake system. The brake disc rotates at a certain rotational speed ω.

The area of the friction ring depends on the geometry of the brake pad and is limited by the outer r_O and inner radius r_I of the pad. Including the aperture angle of the pad $\pm\alpha$ the contact area A of the brake pad/disc is defined by this geometrical information, see the blue marked area in Fig. 4.7.

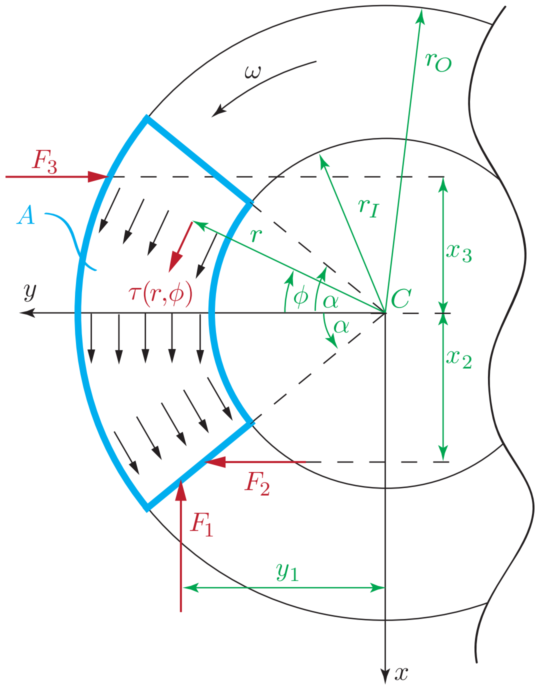

Figure 4.7.: Principal depiction of the acting forces in the brake disc/pad contact containing geometrical information of a generic brake system.

The relative motion between pad and disc induces a friction force per area unit, $\tau(r,\phi)$, in the area A. The magnitude of τ depends on the current brake pressure distribution and the currently acting friction coefficient. Furthermore, restraining forces hold the pad in position. Figure 4.7 shows these forces (F_1, F_2, F_3) and the corresponding geometry (y_1, x_2, x_3) for a generic brake system.

Considering steady state conditions, the equilibrium of forces in x- and y-direction as well as the equilibrium of forces around the disc centre C read

$$\int_A \tau(r,\phi)\cos(\phi)\mathrm{d}A - F_1 = 0, \tag{4.6}$$

$$\int_A \tau(r,\phi)\sin(\phi)\mathrm{d}A + F_2 - F_3 = 0, \tag{4.7}$$

$$-\int_A \tau(r,\phi) r\mathrm{d}A + F_1 y_1 + F_2 x_2 + F_3 x_3 = 0. \tag{4.8}$$

In addition, it is assumed that the brake pressure is equally distributed and the friction coefficient is constant inside the contact area A. Consequently $\tau(r,\phi)$ is constant at a value τ. Considering this, Equ. (4.6) can be written

$$F_1 = \tau \int_{r_I}^{r_O}\int_{-\alpha}^{\alpha} \cos(\phi) r\mathrm{d}r\mathrm{d}\phi = \tau(r_O^2 - r_I^2)\sin(\alpha). \tag{4.9}$$

From Equ. (4.7) follows

$$F_3 = \tau \int_{r_I}^{r_O} \int_{-\alpha}^{\alpha} \sin(\phi) r \mathrm{d}r \mathrm{d}\phi = \tau \frac{(r_O^2 - r_I^2)}{2} \underbrace{(\cos(-\alpha) - \cos(\alpha))}_{=0} + F_2. \tag{4.10}$$

Thus, the total forces in y-direction of the frictional contact equals zero if a constant τ is assumed and due to this F_2 equals F_3. Combining Equ. (4.8) and Equ. (4.9) it follows

$$F_2 = F_3 = \frac{\tau \int_{r_I}^{r_O} \int_{-\alpha}^{\alpha} r^2 \mathrm{d}r \mathrm{d}\phi - \tau (r_O^2 - r_I^2) \sin(\alpha) y_1}{x_2 + x_3}, \tag{4.11}$$

$$= \tau \frac{2\alpha(r_O^3 - r_I^3) - 3(r_O^2 - r_I^2)\sin(\alpha) y_1}{3(x_2 + x_3)}. \tag{4.12}$$

Figure 4.8 left shows the acting forces on the investigated brake system. Thereby, a guide pin (F_1, F_2) and a locking pin (F_3) hold the pad in position. The right side shows the resulting force F and the angle β acting on the guide pin. They are given by

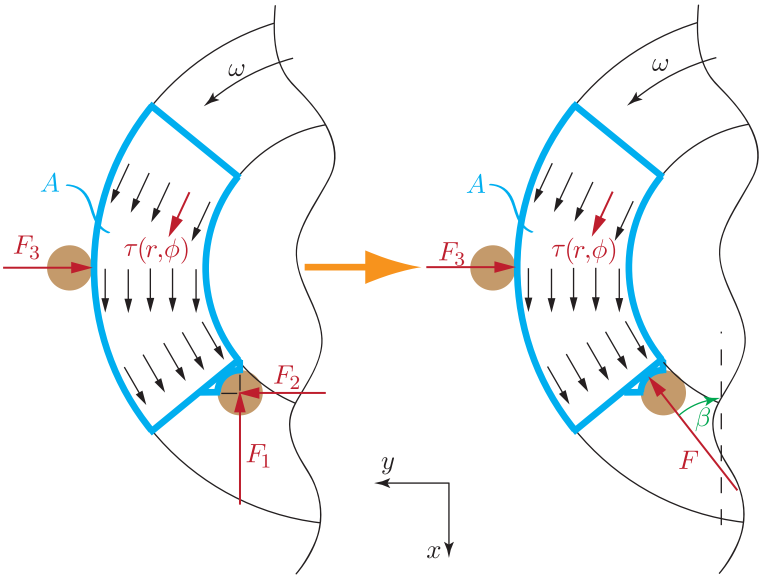

Figure 4.8.: Principal depiction of the measured force and associated geometry of the analysed brake system.

$$F = \sqrt{F_1^2 + F_2^2}, \tag{4.13}$$

$$\beta = \arctan \frac{F_2}{F_1}, \tag{4.14}$$

$$\beta = \frac{2\alpha(r_O^3 - r_I^3) - 3(r_O^2 - r_I^2)\sin(\alpha) y_1}{3(x_2 + x_3)(r_O^2 - r_I^2)\sin(\alpha)}. \tag{4.15}$$

Due to the simplifications made, β depends only on the geometry of the system. For the investigated brake system, the angle β_B equals $8.5\,^\circ$. Based on this calculation of the angle the pins are installed. The simplifications include the assumptions of constant location-independent brake pressure distribution and a constant friction coefficient. Hence, τ is a constant value.

There are uncertainties regarding these underlying assumptions. Thereby, it has to be taken into account that the investigated brake system is a fixed caliper brake system with four pistons, two on each side. As a result, a smoother brake pressure distribution can be reached compared with one piston floating caliper brake. This supports the assumption of the location independent brake pressure distribution.

Also the variation of the friction coefficient per area unit is an uncertainty. It is known that the friction coefficient depends on several parameters such as temperature, sliding velocity, contact pressure, prior charge and wear (see e.g. [128]). Additionally, there is no method known to measure the local friction force per area unit in the brake disc/pad contact area. As a consequence, the friction coefficient is usually calculated using the resulting brake torque, the applied brake pressure and some uncertain parameters, see Chap. 4.1.2.

In reality, τ depends on the brake pressure distribution and the currently acting friction coefficient. Therefore, the direction β of the resulting friction force may not be equal to the installed friction force measuring direction β_B. The impact of this angular deviation $\gamma = \beta - \beta_B$ has to be considered. Thus, the measured friction force F_M may not relate exactly to the acting friction force F, see Fig. 4.9. The relative measurement error due to the misalignment equals

$$\frac{1 - \cos\gamma}{1} 100\,\%. \tag{4.16}$$

Thus an angular deviation of $\gamma = 10\,^\circ$ results in a relative measurement error of only $1.52\,\%$. Consequently, the measurement error is acceptable small. A technical drawing of the pin can be found in the Appendix, Chap. A.3.

Pad Shear Strain

Brake pad materials are highly anisotropic materials. During squeal, the friction force shears the pad. Hence, it would be interesting to know this shear force, or at least the shear strain. Therefore, strain gauges are mounted on the side of the brake pads. As a result, information about the shear strain and the shear force during a squeal event can be gained.

The upper image in Fig. 4.10 shows the brake pad with the surface prepared for the installation of the strain gauges. The lower image in Fig. 4.10 shows the installed strain gauges. In Chap. 4.2.1 the cut-off frequencies for strain gauges are derived. For the

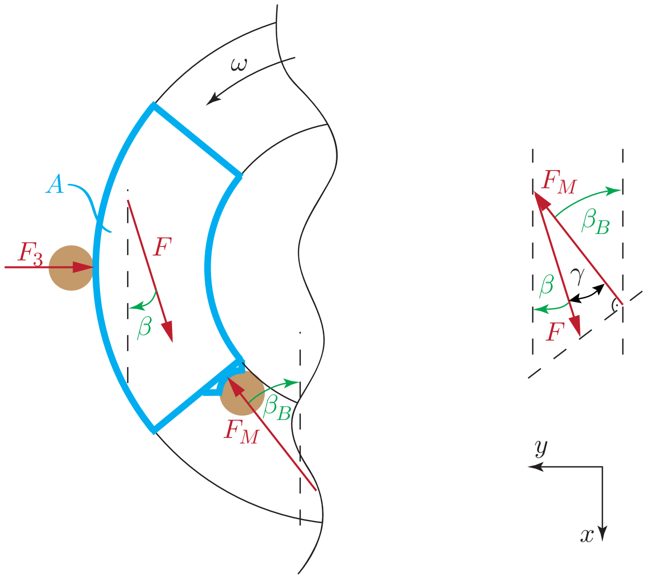

Figure 4.9.: Measurement error due to the angular deviation γ.

softer organic brake pads, the estimated limit frequencies equal 49 kHz if a measurement error of 2 % is taken into account.

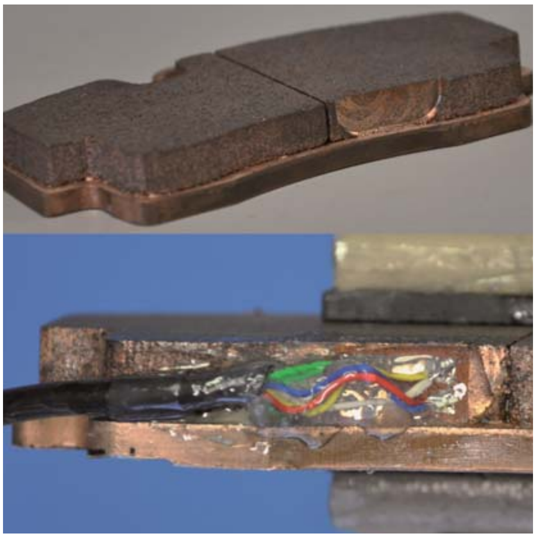

Figure 4.10.: Modified brake pads for shear force measurements.

4.2.3. Operational Deflection Shape Determination

Disc

The measurement system has to be able to determine the ODS of the brake disc. Using the approach presented by Marschner and Rischbieter [108], three miniature *Triaxial Acceleration Sensors* (TAS) are mounted in the cooling ducts of the brake disc. Two of them are mounted in one cooling duct on different radii, the third one is located in an adjacent cooling duct on the outer radius, but on the other side. Figure 4.11 shows the two TASs at the outer radius, the third one at the inner radius cannot be seen. The limit frequency of the acceleration sensors is 8 kHz. A slip ring transmits the acceleration signals out from the rotating disc.

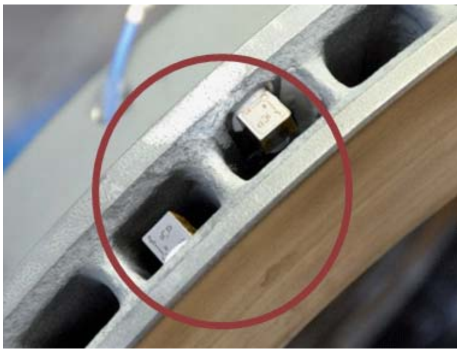

Figure 4.11.: TASs mounted in the cooling ducts of the disc.

To estimate the ODS of the disc it is necessary to know the exact position of the sensors, hence the revolution angle of the disc. For this reason, an incremental encoder is installed. Now a correlation of the rotating disc's acceleration signals to the deflection and acceleration signals of the pad is possible and the rotating speed can be measured.

Pad

In fixed caliper brakes the ODSs of the brake pads are difficult to measure. Optical methods cannot be used because the direct view of the brake pad is blocked by the caliper. The hardly available free space in the brake system limits the possibilities for the acceleration sensor application. The only possibility to mount the sensors is usually on the top (outer radius) of the pad. Using these sensors it is not possible to determine the ODS of the brake pad accurately enough to differentiate between bending and torsional mode shapes.

This lead to the development of a new measurement method. Thereby, the brake system dynamics should not be influenced. This can be done by using contact-free measuring sensors such as *Eddy Current Sensors* (ECS). The use of ECSs for that purpose is innovative. Figure 4.12 shows the three ECSs (1, 2, 3) installed on the brake caliper. The output signal is the relative displacement of the brake pad to the brake caliper.

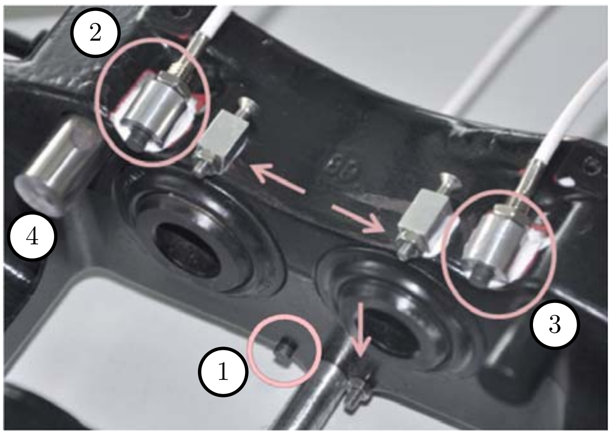

Figure 4.12.: Position of the ECSs (circles) and the adjacent stop pins (arrows) installed on the brake caliper.

To obtain the required resolution, ECSs with a very small measurement range have to be used. As a consequence, they are installed in fine thread sleeves to allow fine adjustment between the measurements. To avoid the sensors being damaged by unexpected high motions of the pad, additionally stop pins are installed, which limit the pads' movement. The limit frequency of the installed ECSs equals 25 kHz with a measurement range of 1 mm and a resolution of 0.05 µm.

Figure 4.13 shows a CAD diagram with the positions of the three ECSs related to the brake pad. One is located at the outer radius shifted from the central axes in the direction of the leading edge. The other two are installed at the inner radius, symmetrical to the pad axis at the leading and the trailing edge.

Additionally, two acceleration sensors (5, 6) are mounted on the outer radius on the top face of the pad backplate. An FEM calculation delivers the possible ODS of the pad. That ensures that the measuring points are not vibration nodes of the pads. These five sensors allow a proper ODS estimation of the pad. Figure 4.13 also shows the previously described friction force measuring guide pin (4), see Chap. 4.2.2.

4.3. Test Set-up

After the description of the developed measurement system, the set-up of the brake system as well as the used signal analysis techniques will be discussed. The brake system of a car which is available on the market is investigated using matrix test series. Additionally in-depth investigations are performed.

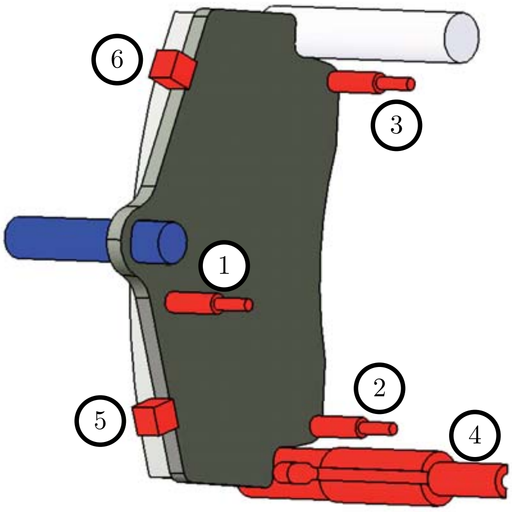

Figure 4.13.: Schematic depiction of the positions of the three ECSs (1, 2, 3), the two acceleration sensors (5, 6) and the special guide pin (4).

4.3.1. Test Bench

The investigations are performed on a brake dynamometer. To include the effects of the suspension, the complete vehicle axle is mounted on a test rack. The geometric position of the suspension supporting points on the rack equals those of the original car body. Figure 4.14 shows this test set-up. Additionally, the suspension gets prestressed. Consequently, the tested geometrical positions of the suspension parts (spring, damper) equals the operational geometrical positions of the suspension mounted in a car as it stands on the road. This proper loading is important due to the non-linearities in the suspension. Without that, the dynamic characteristics are perhaps replicated in an incorrect manner.

The chosen fixture used for mounting the brake system is also recommended by the SAE J2521 standard. The suggested fixture depends on the brake system type and the frequency range which shall be investigated:

- 2 to 17 kHz: A full suspension corner assembly for disc brake tests is not recommended. In that case only brake caliper, brake pads and brake disc are directly mounted on the test rig. Such a test set-up is depicted and discussed later in Chap. 6, see Fig. 6.1. Below the limit frequency of 2 kHz structural transmission may occur which cannot be simulated with such a small test assembly.
- 0.9 to 17 kHz: A full suspension corner assembly for disc brake tests is recommended including the suspension parts. Because the investigated brake system shows squeal frequencies around 2 kHz, it is mandatory to use this kind of test set-up.

- 0.5 to 17 kHz: Recommended frequency range for investigating drum brake systems.

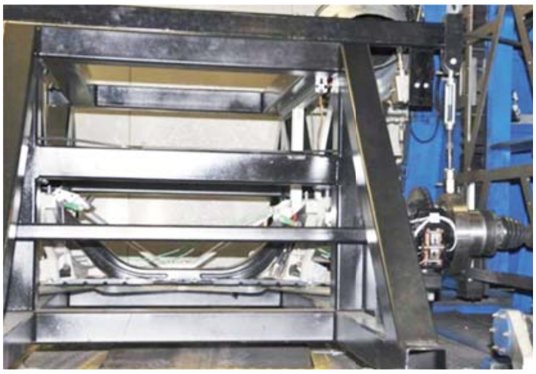

Figure 4.14.: Test set-up showing the test rack at the test bench for NVH investigations.

4.3.2. Brake Pad Material

It would be advantageous for the subsequently performed investigations to have a brake system that squeals often and loudly. As a result, it is easier to perform more precise and repeatable measurements at squealing brake conditions. Thereby, the basic brake system should be changed as little as possible. One possibility is to change the brake pad or the brake pad material respectively.

For the investigation four different brake pads with different material composition are available. Two of them consist of organic material, which is the standard material for automotive brake pads [33]. Additionally, two prototype brake pads consisting of sintered material are tested. These pads are stiffer, have a higher friction coefficient and due to this, they are mainly used in industrial and heavy duty applications. Additionally, the chosen sinter mixtures are well known to have poor squealing properties and no further measures against squeal are implemented on the sinter brake pads. Consequently, they are more likely to produce squeal.

To evaluate the acoustical behaviour of the four different brake pads, the SAE J2521 matrix test series is performed with the complete vehicle axle mounted on a rack on the test bench. Cooling air with a relative air moisture of 50 % and a constant temperature of 11 °C flows at the brake system during testing. To lower the background noise, the ventilation is switched off during every brake application.

The SAE J2521 consists of 2321 brake applications. The test results in a *Squeal Noise Matrix* (SNM) and a value for the *Squeal Noise Occurrence* (SNO) [143]. In the matrix the squealing brake conditions (brake pressure, velocity and pad temperature), the squeal frequency and maximum *Sound Pressure Level* (SPL) during squealing are recorded. The calculation method to obtain the SPL is explained in Chap. 4.3.3.

The maximum SPL value is the threshold value of the measured SPL which is trespassed by more than one percent of all squealing brake applications. In order to calculate the squeal occurrence, one needs to divide the number of squealing brake applications by the number of performed brake applications. Table 4.2 presents the SNO and the maximum SPL of these tests:

Table 4.2.: SNO and maximum SPL of the four investigated brake pads.

	SNO	Max SPL
Organic A	∼ 0.5 %	88 dB(A)
Organic B	∼ 14 %	100 dB(A)
Sinter A	∼ 48 %	110 dB(A)
Sinter B	∼ 71 %	114 dB(A)

As can be seen in Tab. 4.2, the prototype *Sinter B* brake pads provide a quite noisy brake system. Figure 4.15 shows detail results of the *Sinter B* SAE J2521 test.

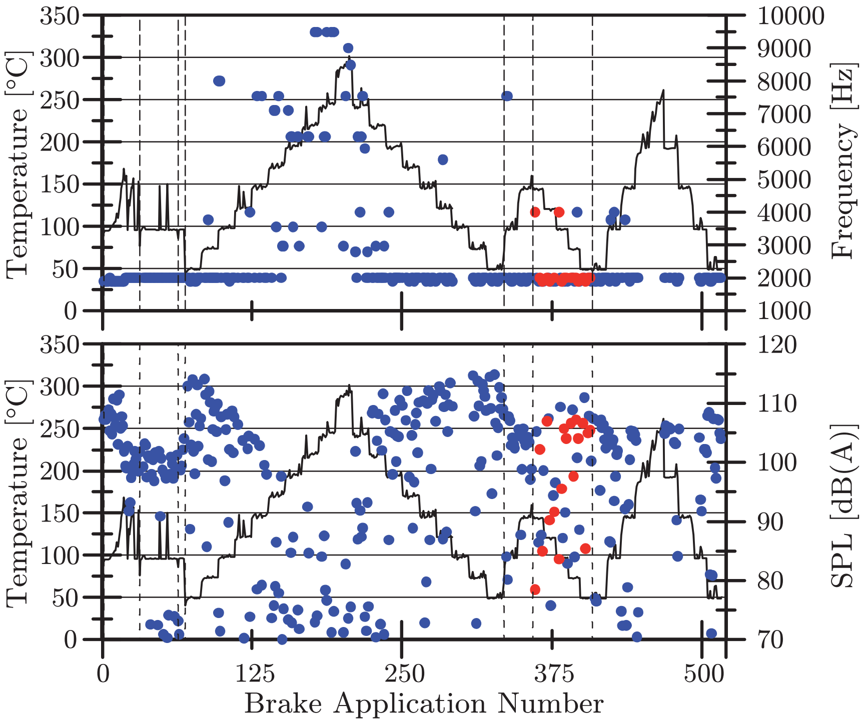

Figure 4.15.: Extract of the SAE J2521 test of the *Sinter B* brake pads.

Only the first 516 brake applications are presented. The x-axis equals the continuous brake application number. The black curve shows the current pad temperature, left y-axis. The right y-axis represents the frequency (upper plot) and SPL (lower plot) corresponding to the squealing brake applications (points). Every point indicates a squealing brake application, red points indicate a brake application in reverse direction of rotation. As can be seen, the main squeal frequency is at approximately 2 kHz and additionally the SPL is mostly above 100 dB(A).

Next, the friction coefficients of the four different brake pads are investigated. Therefore, measurements at five different constant speeds (5, 10, 20, 30 and 50 kph) and four different brake pressures (5, 10, 15 and 30 bar) are performed with all four brake pads. A total of eighty measurements are performed. Due to the friction, the brake system gets heated. For the measurements, the brake disc temperature is analysed. The start temperature of the brake disc is 50 °C and the measurement stops after 300 seconds or if a disc temperature of 350 °C is reached. Figure 4.16 presents the surface plot for a constant brake pressure of 30 bar of the *Sinter B* brake pads. The blue circles indicate measurement points. Thereby, the friction coefficient is calculated regarding the SAE J2521 standard [143], see Equ. (4.1).

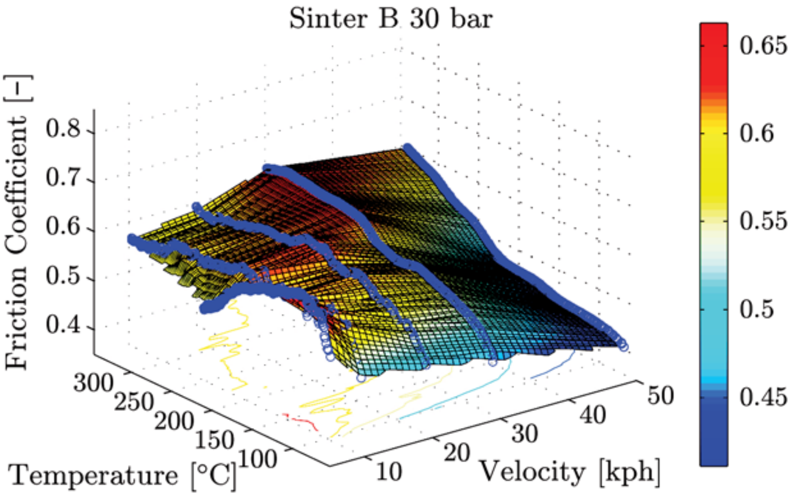

Figure 4.16.: Friction coefficient test *Sinter B* at $p_B = 30$ bar constant brake pressure.

Figure 4.17 shows one exemplary result for the four different brake pads at constant brake pressure of $p_B = 10$ bar. Two tendencies can be observed:

1. A higher velocity results in a lower friction coefficient. Thus, a negative friction velocity slope, such as mentioned in many analytical models, can be observed.
2. A higher disc temperature results in a higher friction coefficient in the observed measurement range. Because brakes squeal mainly at "cold" disc temperatures, the upper temperature is limited to 350 °C, which is less than half of the maximum obtainable temperature. At higher temperatures the effect is inverted, hence the friction coefficient reduces at higher temperatures. This also reduces the obtainable braking force and is called *brake fade* [124].

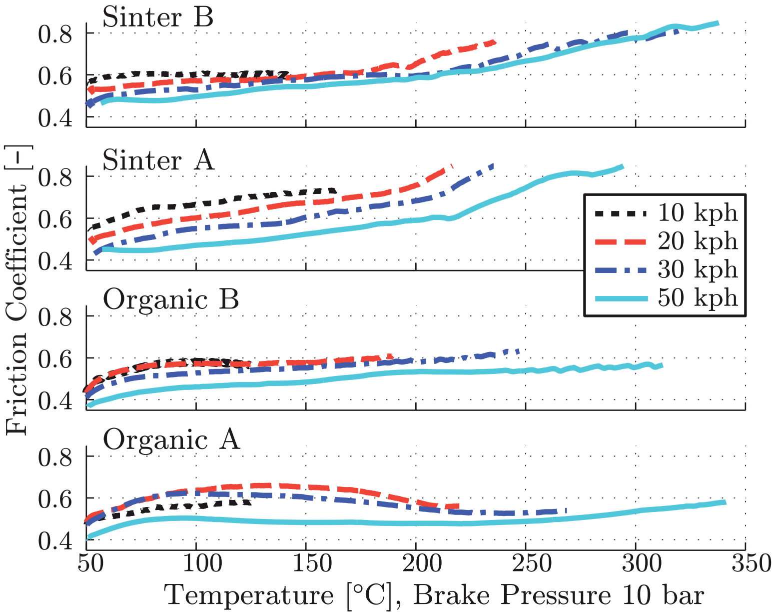

Figure 4.17.: Investigation of friction coefficient of the four analysed brake pads.

In the performed experiments all four brake pads have the tendency to a negative friction coefficient slope with velocity in several operating points. The sintered brake pads have significantly higher friction coefficients compared to the organic ones. Hence, the noisier brake pads have a higher average friction coefficient. Regarding the temperature, the sintered brake pads have an increasing friction coefficient with increasing temperature in the area below 350 °C. In contrast to this, the organic brake pads have only a weak dependency. During braking, the velocity is decreased and the temperature increased. Therefore, the noisier sintered brake pads increase their friction coefficient while braking by both effects: due to the temperature increase and due to the decreasing velocities.

At the end of the brake pad material investigation, an extremely loud squealing brake system is obtained. All the further investigations are performed using the noisy *Sinter B* brake pads. Due to the installed measuring devices and the changed stiffer brake pad material, the main squeal frequency of the systems changes slightly from 1.95 kHz to 2.1 kHz. Consequently, the resulting retroactive effects on the system dynamics because of the installed measuring system are moderate.

4.3.3. Signal Analysis

The gained signals have to be analysed and interpreted. Thereby, the measurement of oscillations has several restrictions which has to be taken into account. As a consequence, several signal analysis methods are used, the most important of which are described in the following including a discussion regarding their requirements, limitations, advantages and disadvantages.

Sampling Rate

First of all, the necessary sampling rate[3] is discussed. Figure 4.18 shows an analog cosine signal (solid line) and the discrete measuring points (thick points). A reconstruction of the cosine signal based on the discretised can result in a signal with an integer multiple frequency of the measured signal (dashed line). Regarding the *Nyquist sampling theorem*, a sampled signal can be completely determined if the original function does not include frequencies higher than half of the sampling rate. Thus, it holds

$$f_S > 2f_{\max}, \tag{4.17}$$

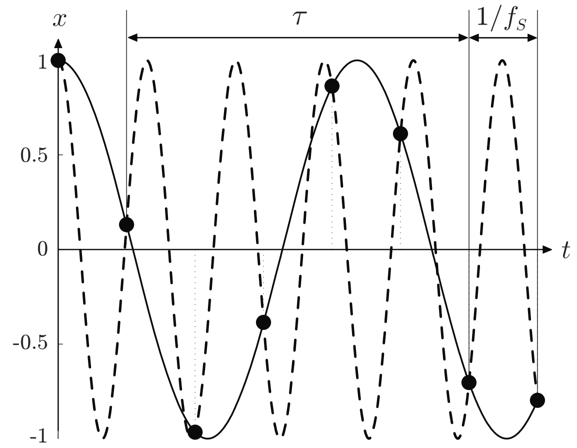

Figure 4.18.: Ambiguity of reconstruction of an analog signal, adapted from [165].

where f_S and $f_{\max}$ denote the sampling rate and the maximum frequency of the signal [165]. To avoid *Aliasing*, hence the wrong interpretation of a higher frequency signal, the sampling rate can be increased or low-pass anti-aliasing filters can be used. This filtering has to be done before the signal is sampled to ensure, that the *Nyquist sampling theorem* applies. These filters limits the evaluable frequency range from 0 Hz to $f_{\max}$.

Fourier Transform

The measured signals are in the time domain, but for the analysis they may be also investigated in the frequency domain. A transformation between these two domains can be done by using the *Fourier transform* for analog signals. Thereby, it is assumed that any signal in the time domain is the sum of sinusoidal oscillations with different frequencies, amplitudes and phases. The *Fourier transform* transforms the signal in the frequency domain and determines the amplitudes and phases according to the frequencies. The result is the spectrum of the signal.

---

[3] The *sampling rate* gives the number of sample points per second. Thus, it equals a frequency and is also called *sampling frequency*.

Due to the sampling with the sampling rate the signals are discrete signals $\mathbf{y}(n)$. As a result, a specific kind called *Discrete Fourier Transform* (DFT) has to be used. The transformation results in a discrete spectrum $\mathbf{Y}(k)$, which is a vector of complex numbers consisting of amplitudes and phases information. This is given by

$$\mathbf{Y}(k) = \sum_{n=0}^{N-1} \mathbf{y}(n) \mathrm{e}^{-j2\pi nk/N} \qquad k = 0, 1, \ldots, N-1. \tag{4.18}$$

Depending on the evaluated time range τ and sampling rate f_S, the measured signal $\mathbf{y}(n)$ consists of N time equidistant sampled values, see e.g. Fig. 4.18. Hence, the block length of the signal reads

$$N = \tau f_S. \tag{4.19}$$

The largest frequency of the obtained spectrum is given by the *Nyquist sampling theorem*. Consequently, the frequency spectrum is calculated in the range of $[-f_S/2, +f_S/2]$. The smallest frequency and the frequency resolution Δf is given by

$$f_{\mathrm{min}} = \frac{1}{\tau} = \Delta f, \tag{4.20}$$

where τ denotes the evaluated time range. A characteristic of the DFT is, that the length N of the input vector $\mathbf{y}(n)$ is equal to the length of the output vector $\mathbf{Y}(k)$. The DFT calculation results in a system of equations consisting of N^2 complex multiplications.

A special type of DFT is the *Fast Fourier Transform* (FFT). Thereby, the block length has to be a power of two. In this case, the system of equations can be rearranged which results in a number of $N \log(N)$ necessary calculations. Thus, the FFT is a fast calculation method. Additionally it has to be noted that the FFT delivers an exact solution of the DFT and is not an approximation of it, see e.g. [165].

RMS and SPL

The *Root Mean Square* (RMS) for an analogue signal over time, such as the sound pressure $\mathrm{p}(t)$, is given by

$$p_{\mathrm{RMS}} = \sqrt{\frac{1}{t_2 - t_1} \int_{t_1}^{t_2} \mathrm{p}^2(t) \mathrm{d}t}, \tag{4.21}$$

where t_1 and t_2 define the start and stop time of the evaluation. During a measurement, the analogue signal is sampled with the sampling rate f_S. This results in a vector $\mathbf{p}_M$ of discrete values with a length of N, where the size of N depends on the sampling rate and the time constant $\tau = t_2 - t_1$. Therefore, p_{RMS} can be calculated as

$$p_{\mathrm{RMS}} = \sqrt{\frac{1}{N} \sum_{i=1}^{N} p_{Mi}^2}. \tag{4.22}$$

In dynamic measurements, the RMS calculation smoothes the measured signal, see Fig. 4.19. The smoothing depends on the time constant τ. As a consequence, three time-weightings have been standardised for acoustic measurements, see e.g. [53]:

S: *Slow* signals, τ equals 1 s, e.g. noise pollution measurement.

F: *Fast* signals, τ equals 0.125 s, e.g. brake squeal measurement.

I: *Impulse* signals, τ equals 0.035 s, e.g. explosions measurement.

For the brake squeal measurements, F-time-weighting is used.

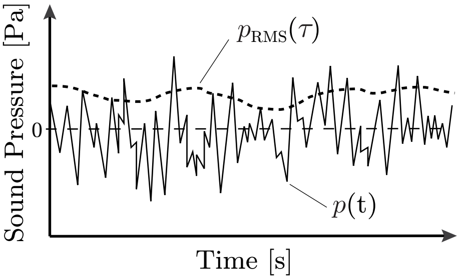

Figure 4.19.: Schematic depiction of the smoothing effect of time-weighting τ if calculating p_{RMS}, adapted from [165].

The *Sound Pressure Level* (SPL), measured in dB, is a logarithmic representation of the RMS value given as

$$\mathrm{SPL} = 10 \log \frac{p_{\mathrm{RMS}}^2}{p_{\mathrm{ref}}^2} = 20 \log \frac{p_{\mathrm{RMS}}}{p_{\mathrm{ref}}}, \tag{4.23}$$

where p_{ref} denotes a reference value which is the threshold of human hearing at 1 kHz specified as $p_{\mathrm{ref}} = 20\,\mu\mathrm{Pa}$. The human ear detects the SPL, but the sensitivity depends on the frequency and the amplitude of the noise. This is the reason why four different weight functions (A, B, C, D) exist to match the physical pressure measurement to the hearing ability of a person.

The weight function has to be chosen regarding the current loudness. Weight function A is for low noise and D for loud noise. Additionally the measured SPL depends on the distance to the emitting object. In the SAE J2521 standard the position of the microphone with respect to the centre of the disc is defined to be 10 cm outboard from wheel hub face along the centreline of the axle and 50 cm above and perpendicular to the centreline of the axle [143].

This definition results from an approximation of the commonly chosen microphone location in full vehicle evaluations and equals the edge of a vehicle wheel. For higher frequencies, where the dimension of the disc is much larger than the wavelength of the sound, a single microphone may be insufficient to fully characterise the emitted sound because the directional radiation pattern may be anticipated. Nevertheless, a standardised location is needed and experience as well as comparable results from different dynamometers showed that this location works well [158].

In the SAE J2521 standard A-weighting is specified which is usually used for SPL below 40 dB. However, squeal is specified as, already weighted, noise above 70 dB(A). Depending on the frequency at least B-weighting (C-weighting respectively) would be necessary, see e.g. [52, 117].

5. Experimental Analysis Results

With the complex measurement system, several investigations are performed. Thereby, the experiments are mainly carried out with the sintered brake pads. The main difference is that the sintered brake pads are stiffer and have a higher friction coefficient. In addition, no counter-measures are taken at the sinter brake pads. As a result, a brake system is obtained that squeals often and loudly.

The performed investigations are divided into three parts:

Selected Sensor Results: First of all, the results obtained with the most important sensors of the complex measurement system are discussed. The investigation evaluates the advantages and disadvantages as well as limitations of these sensors. This should provide a basic understanding of the used measurement system and analysing methods.

In-Depth Investigations: With the developed measurement system it is possible to investigate the brake system up to high frequencies. Such an analysis with a sampling rate of 200 kHz is presented in detail. Thereby, the strain gauge base sensors delivers further insight into the brake squeal triggering mechanism. In addition, two measurements are presented which show some interesting effects regarding their squeal behaviour.

Sensitivity Analysis: With the investigated brake system, 180 brake applications are performed. Thereby, subsequently only one parameter of the brake system is changed during the measurements. Thus, the suitability of different counter-measures is determined. In addition, the suitability of the different sensors for squeal determination is evaluated.

5.1. Selected Sensor Results

5.1.1. Triaxial Acceleration Sensors: ODS Disc

Three *Triaxial Acceleration Sensors* (TAS) are mounted in the cooling ducts of the brake disc. The axial direction equals the axis of rotation of the disc. The radial directions goes from the axis of rotation through the sensor and the tangential direction equals the direction of motion of the sensor. Using the three sensors, it is possible to determine the *Operational Deflection Shapes* (ODS) of the brake disc. An ODS consists of several nodal diameters and circles in out-of-plane[1] and in-plane[2] direction. Since

---

[1] Vibration in axial direction of the disc.

[2] Vibration in radial and tangential direction of the disc.

the investigated brake system shows dominant out-of-plane vibrations, only this type of vibration is discussed in the following.

Usually, the ODS of the disc is denoted as "(m,n)-shape", whereby m indicates the number of nodal circles and n the number of nodal diameters [68, 100]. For example in Chap. 3, Fig. 3.22 shows a (0,3) ODS of the disc calculated with the FEM.

The vibration of the brake disc is steady with respect to the caliper. As a consequence, an acceleration sensor in the disc moves during the rotation through the ODS of the disc, which is steadily seen from the outside. The number of measured points of this ODS depends on the rotation speed and the sampling rate. Figure 5.1 represents the sensor signal of one triaxial sensor in the brake disc, in axial direction, during a squealing brake application. One revolution is marked in the figure. In this case, the constant velocity during the brake application equals approximately 10 kph or 79 rpm. At a sampling rate of 200 kHz, approximately $1.52 \cdot 10^5$ points are measured per revolution.

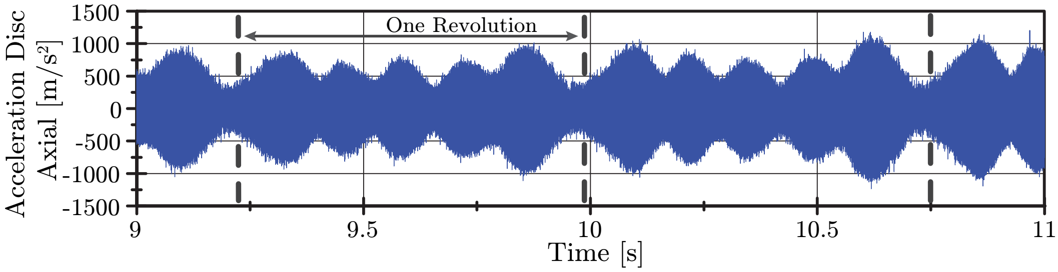

Figure 5.1.: Measurement signal in axial direction of one TAS mounted in the cooling ducts of the disc.

During a squealing brake application, this signal consists of two dominant vibrations: a higher frequency part which is equal to the squeal frequency and a lower frequency part. This part is visualised by calculating the RMS value and afterwards the envelope of the signal. Due to the positioning by the incremental encoder, the resulting signal can be plotted as a circular plot. Figure 5.2 shows such a circular plot of five rotations during a squealing brake application. Additionally, the figure shows the position of the brake pad. The centre of the pad is located at 0 °.

In Fig. 5.2 five vibration nodes are clearly visible. Every nodal diameter results in two vibration nodes, hence a (0,3) shape results in six vibration nodes and obviously six antinodes, but only five antinodes are visible. Considering the necessary symmetry, the sixth antinode has to be located at 0 °. A closer zoom at this area shows that there is a small antinode at this position. However, due to the pads which press against the disc, this antinode is almost completely suppressed.

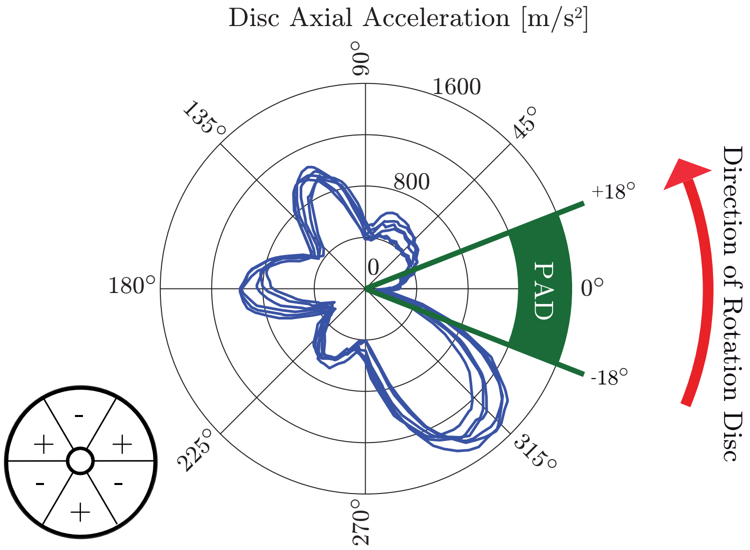

Figure 5.2.: Circular plot of the axial acceleration RMS envelope value of a sensor mounted in the cooling ducts of the disc during a squealing brake application.

As long as no nodal circles exist and the disc surfaces vibrate in phase, one acceleration sensor is enough to determine the ODS. Two sensors in the same cooling duct on different radii are needed to detect if there are any nodal circles. If there is only one nodal circle and the sensor is mounted at the inner and the outer radii the axial acceleration signals will be opposite in phase.

For a clear determination of the nodal circles, several acceleration sensors in one cooling duct are necessary. Analog to the required minimum number of sample points to measure clearly vibrations in the time domain, a disc vibration with two nodal circles would need several sensors. For space reasons this is not possible. However, FEM simulations deliver the natural modes and natural frequencies which are similar to the measured ODS and frequency. By comparing the measured signals with the calculated natural frequencies, the number of nodal circles can be estimated. Additionally, the FEM determines proper measuring points for installing the sensors.

In the investigated brake disc, two acceleration sensors are mounted in one cooling duct on the same side to estimate the nodal circles. The third one is located in an adjacent cooling duct on the other side, see Fig. 4.11. This is necessary to determine if the disc surfaces vibrate in axial direction in or opposite in phase. A vibration opposite in phase is a *pumping* (or *breathing*) vibration shape, hence the disc surface moves axial in opposite direction and the distance between the surfaces changes. In addition, a comparison of the signals in tangential direction shows if the disc surfaces vibrate in tangential direction in or opposite in phase.

Finally, the signals in axial direction deliver the out-of-plane vibration shape. The signals in tangential direction determine the in-plane vibration shape. The investigated brake disc mainly shows a dominant out-of-plane vibration, hence a vibration in axial direction in a (0,3) ODS at a frequency around 1.95 kHz if organic brake pads are used and around 2.1 kHz if sintered brake pads are used.

5.1.2. Eddy Current Sensors: Pad ODS

The *Eddy Current Sensors* (ECS) measure the relative displacement between pad and caliper. A comparison of the acceleration signals from TASs mounted on the pad and on the caliper during a squealing brake application shows the following: the vibrating acceleration amplitudes for the same measurement direction of the sensors on the pad are up to ten times greater than those on the caliper. This is because the investigated system consists of a fixed caliper brake. These calipers are designed to be rather stiff. This results in a better brake pedal feeling because the widening of the caliper due to the brake pressure is small.

Thus, the measured relative displacement is mainly due to the brake pad motion. During squealing, the ECSs measure a vibration in phase at the pad's leading and trailing edge. The vibration of the middle sensor, which is next to the central axes of the pad shifted in direction to the trailing edge, shows a vibration opposite in phase.

Figure 5.3 shows the offset-corrected measurement signal for one millisecond during squealing (left) and non squealing (right) state. During squealing, the vibration is clearly visible. The amplitude of the vibration at the leading edge is significantly higher than the vibration in the middle and at the trailing edge. If there is no squealing, the pad sensors show no vibrating motion. The two plots are from one continuous measurement of one brake application, which first squeals and then stops squealing.

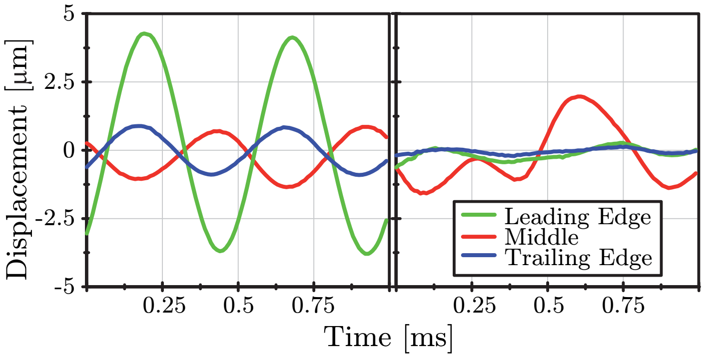

Figure 5.3.: Measurement signal obtained from the ECSs during squealing (left) and not squealing (right) state.

Comparing the measured signal during squealing with calculated mode shapes, using the FEM and the material properties of the organic brake pads leads to the assumption that the pad ODS during squeal equals the first bending mode. Figure 5.4 shows this calculated mode at an eigenfrequency of 1822 Hz. The next possible mode shape is the first twisting mode at an eigenfrequency of 2186 Hz, but in that case the measured sensor signals of leading and trailing edge have to show vibrations opposite in phase, which is not the case in the measurement. In the experiments, the determined pad ODS are independent from the used pad material, but the frequency of the vibration, which equals the squeal frequency, is increased.

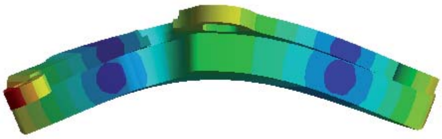

Figure 5.4.: Calculated first bending mode of the pad at 1822 Hz.

The sintered brake pads are stiffer than organic brake pads. The resulting effect caused by the higher stiffness can be explained with a simple single DoF oscillator with a mass m, a stiffness c and neglecting damping. The eigenfrequency f reads

$$f = \frac{1}{2\pi}\sqrt{\frac{c}{m}}. \tag{5.1}$$

Hence, an increase in the stiffness also increases the eigenfrequency. As a result, the first bending mode of the pad is shifted towards the squealing frequency of the disc. Due to this, mode-coupling occurs more easily which is the reason why, in addition to the higher friction coefficient, the sintered brake pads squeal more and louder than the organic brake pads. This also explains combined with a lower damping of sintered brake pads the observable frequency shift because of changing the pad material.

5.1.3. Friction Force Measuring Pins

The guide pins at the leading edge of the caliper are replaced by friction force measuring pins. Figure 5.5 shows an exemplary result obtained with these sensors. Thereby, F_O indicates the friction force measured by the pin at the outer side and F_I the pin at the inner side. The upper plots present the measured sound pressure obtained from a microphone, the lower plots show the measured friction force obtained by the friction force measuring pins. The left plots present the complete test and the right plots a zoom of the signals around 18.352 s. The test was performed with a constant rotation speed of 88 rpm which equals a velocity of 11.14 kph. Brake pressure was applied from 15.75 s to 19.75 s. Squeal occured immediately after the brake pressure was applied and stopped with the end of the brake event.

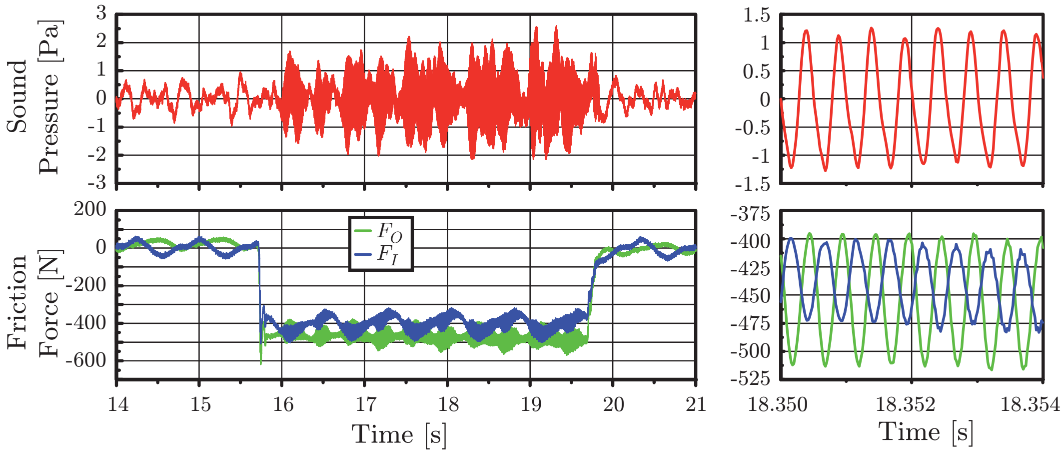

Figure 5.5.: Measurement results for a brake squeal event.

Before and after brake pressure was applied, a low frequency vibration (1.5 Hz) is visible. This frequency equals the rotation speed and the signals show the remaining forces acting on the pads. This is because the pads are not completely separated from the brake disc and a friction force acts. As a consequence of axial run-out of the disc and/or *Disc Thickness Variation* (DTV), these forces occur. This results in a forced vibration, the frequency of which depends directly on the rotation speed and this is also visible during braking. These effects are usually responsible for brake drag torque and brake judder issues.

Immediately after brake pressure application, the system starts to squeal. The pins now show a quasi-static friction force of approximately 450 N, the previously mentioned low frequency vibration with an amplitude of below 50 N and a superposed high frequency vibration is also visible. In the zoom of the signals, see Fig. 5.5 right, it can be seen that the frequency of the friction force vibration equals the measured squeal frequency of the microphone. In addition, the amplitude of the high frequency vibration equals approximately 100 N, hence about one-fifth of the quasi-static friction force.

During squeal the vibrations of the friction force are opposite in phase. The TASs determine a dominant out-of-plane vibration of the disc which acts in the same manner as a membrane of a loudspeaker and emits the noise. Thereby, the surfaces of the disc oscillate in phase. The modes of both brake pads ”ride” on this deflection shape and also oscillate in phase. However, the deflection of the disc adds additional load on one pad and reduces the load on the other pad. Thus, the normal force F_N and furthermore the friction force F_F vibrations have to vibrate opposite in phase.

Figure 5.6 shows an additionally performed FFT of the microphone and the friction force signals. Thereby, the time range of 1 s, from 17 s to 18 s is evaluated. It can be clearly seen that the high frequency vibration of the friction force equals the squeal frequency at almost 2 kHz.

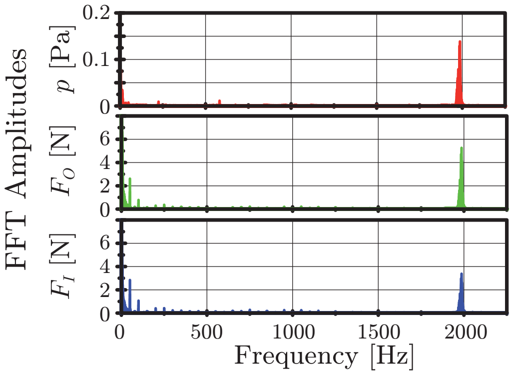

Figure 5.6.: FFT amplitudes of microphone and friction forces.

Balvadi and Gerges [19] claim that squeal noise occurs when the modes of the brake disc are coupled with those of the brake pads. In their opinion, this is the main root cause of noise. Exactly this could be proved in the experiments.

The measurements confirm the suitability of the different measurement methods to estimate the ODS of disc and pad. In addition, the friction force measuring pins verified a coupling of pad and disc vibration. Also the influence of geometric inaccuracies in the brake system, such as axial disc run-out and DTV, could be observed with the newly developed friction force measuring pins.

5.2. In-Depth Investigations

5.2.1. High Frequency Analysis

The strain gauges mounted on the pin and on the side of the brake pads allow measurements up to very high frequencies, merely limited by the sample rate. For the investigation, a sampling rate of 200 kHz is used, which allows signal analysis up to 100 kHz according to *Nyquist sampling theorem.* The measurements are performed to investigate high frequency vibrations in frictional contact with the developed sensors. The existence as well as the influence of ultrasonic vibrations can be determined. A similar analysis was performed by Wernitz and Hoffmann [168] using special calibrated acceleration sensors.

Two brake applications are performed, which only differ in the applied brake pressure and in their resulting squealing behaviour. At the squealing braking, the brake pressure equals 15 bar, at the not squealing one 10 bar are applied. The FFTs of microphone and several sensors show that the system vibrates mainly with a frequency of 2.1 kHz which is also the squealing noise frequency.

Figure 5.7 shows the sound pressure p measured by the microphone and disc axial acceleration signal $a_{d,\mathrm{axi}}$ at non squealing condition and Fig. 5.8 at squealing condition. Comparing these plots it can be seen that the amplitudes at squealing conditions are approximately three times larger.

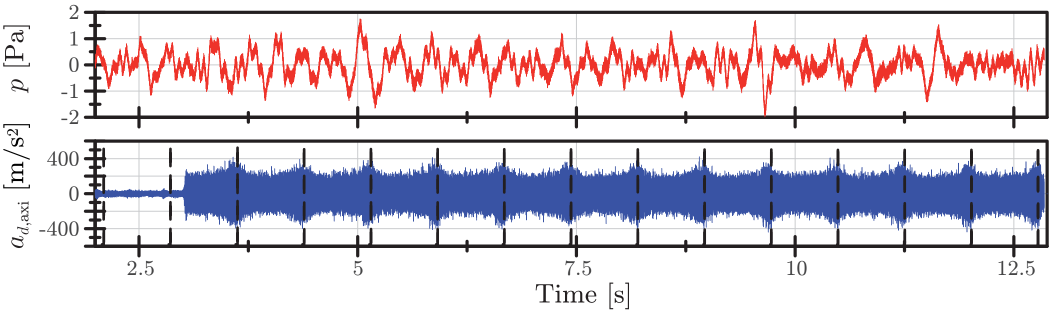

Figure 5.7.: Microphone and disc axial acceleration signal at non squealing condition.

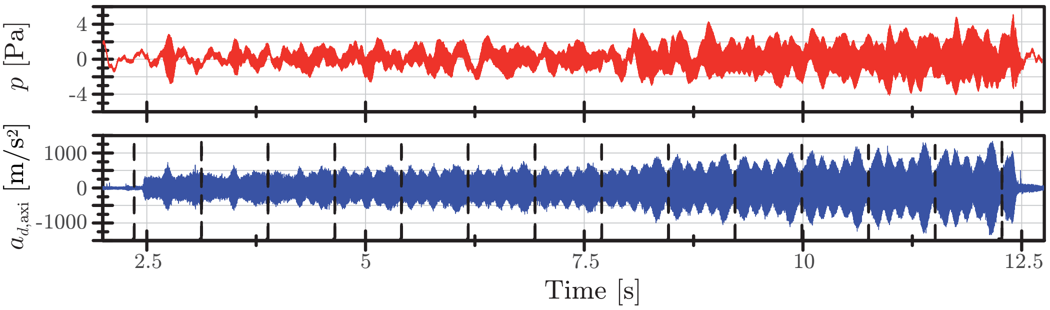

Figure 5.8.: Microphone and disc axial acceleration signal at squealing condition.

During squealing, a coupling of the vibrations can be observed: Figure 5.9 shows the vibration of the friction forces (original, unfiltered data) and the two times integrated disc axial acceleration signal $a_{d,\mathrm{axi}}$ which results in the axial displacement $x_{d,\mathrm{axi}}$.

The signals are now plotted over the signal of the incremental encoder. At 18 ° the acceleration sensor is located between the friction force measuring pins. It can be seen that the friction force sensors vibrate exactly opposite in phase with a similar amplitude. There is a very small phase shift between the disc deflection and the outer friction force of approximately 0.03 °, which is possibly caused due to the damping characteristic of the pad material or a measurement error. This measurement confirms the correlation between disc motion and friction force vibration.

Figure 5.10 shows the shear signals S_O and S_I of the strain gauges mounted on the side of the brake pads. They are digitally bandpass-filtered below 100 Hz and above 20 kHz for better visibility. These strain gauges are not calibrated. In principle, strain

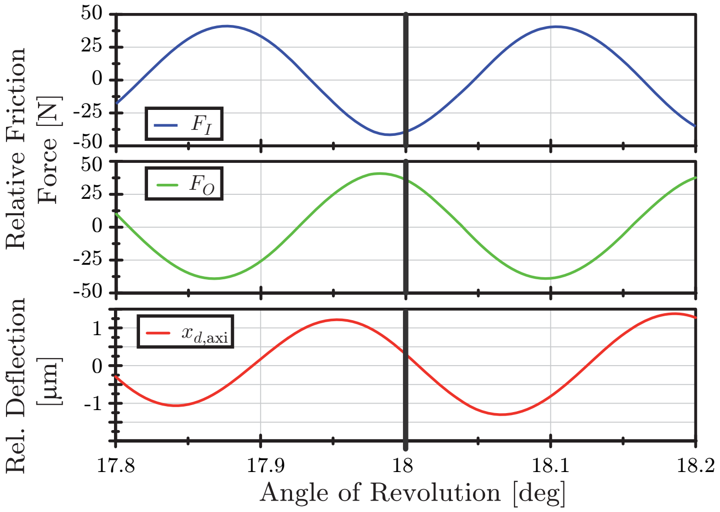

Figure 5.9.: Friction force signals and twice integrated disc axial acceleration signal during squeal.

gauges are calibrated using known forces such as done for the friction force measuring pins. However, this is not possible for the strain gauges mounted on the side of the brake pads.

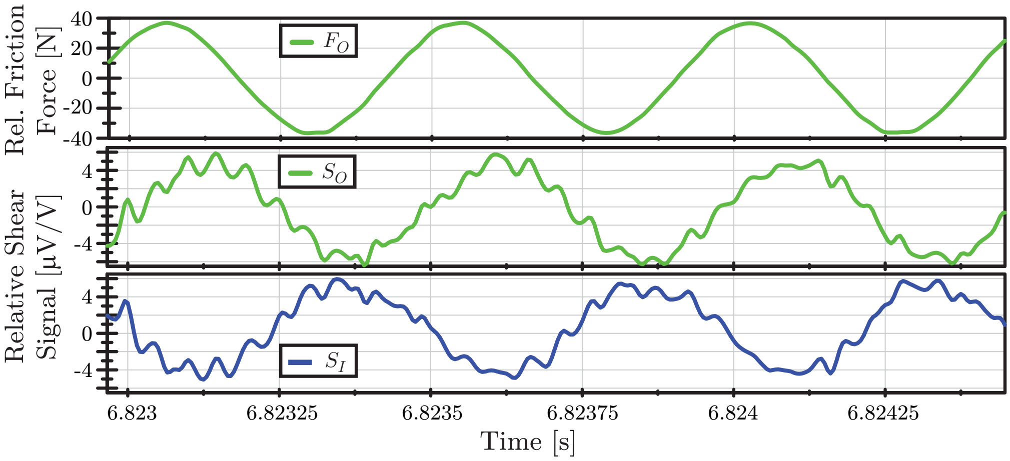

Figure 5.10.: Friction force and strain gauge signals during squeal.

Attempts to calibrate the output signal with a known force acting in the disc/pad contact area in sliding direction results in the problem that creep effects due to micro-stick-slip effects in the contact area falsify the results. In addition, an applied force in normal direction, hence brake pressure, also induces a shear strain. Nevertheless, the obtained signals provide a further insight into the frictional contact such as amplitude ratio and phase relation. Thus, only a qualitative statement about the shear strain can be made using the direct gained electrical output signal of them, which is in mV/V.

The signals of the force measuring pin and the shear measurements vibrates almost in phase. The shear signals of inner and outer side of the brake pads vibrate opposite in phase, hence in the same way as the friction forces. However, the *Signal to Noise Ratio* (SNR) of the shear signals is smaller compared to the friction force signals. The shear signals also show some high frequency vibrations with low and hardly visible amplitudes, which may result from interference frequencies and not from the friction contact. Consequently, they are not further investigated.

The FFTs of the three ECSs signals show, that each measured amplitude of the 2.1 kHz vibration increases during the brake applications. The same can be obtained for the microphone system and the disc acceleration, cf. Figure 5.8.

For further analysis, the ECSs signals are digitally bandpass-filtered below 200 Hz and above 8 kHz. Due to this, the effects of rotation speed dependent excitation (about 1.3 Hz), such as disc run-out and DTV, as well as the motion when brake pressure is applied, are excluded. Additionally, the RMS of the ECS signals for a time constant τ equals 0.1 s is calculated, see Fig. 5.11. The increasing amplitudes are now clearly visible. The sensor on the leading edge has always the largest amplitude, almost five times larger than the amplitude at the trailing edge. In addition, despite the filtering, some rotation periodic characteristic can be seen.

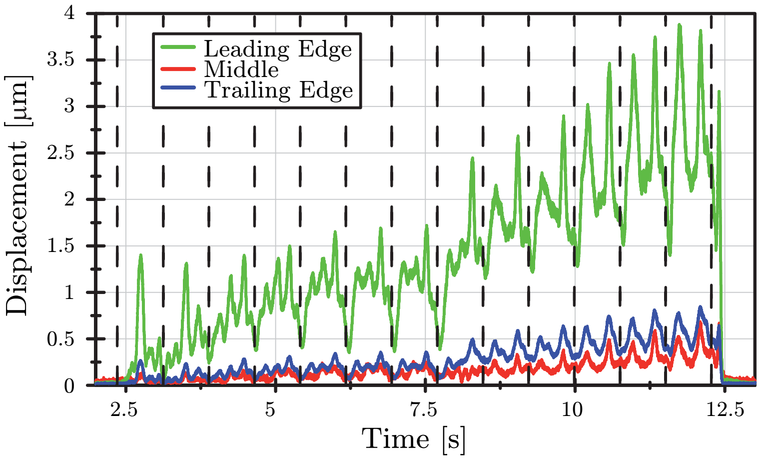

Figure 5.11.: Filtered RMS of the ECS during squeal event.

Figure 5.12 shows a zoom of three revolutions. There are at least two peaks per revolution visible at all three sensors. Because of the filtering, these increases cannot be the direct result of the disc displacement due to the geometrical inaccuracies[3] of the brake system. However, the inaccuracies effect the excitation of the system which results in a higher vibration amplitude.

---

[3] Such as disc run-out and DTV.

Hence, there is a coupling between the squeal vibration at 2.1 kHz and the vibrations due to the inaccuracies of the brake system at 1.3 Hz. The inaccuracies have a strong effect on the frictional contact and furthermore on the excitation of the system. As a result, the vibration amplitude at squeal frequency, hence the squeal behaviour, is strongly influenced by the low frequency excitation resulting from inaccuracies of the brake system just as disc run-out and DTV[4].

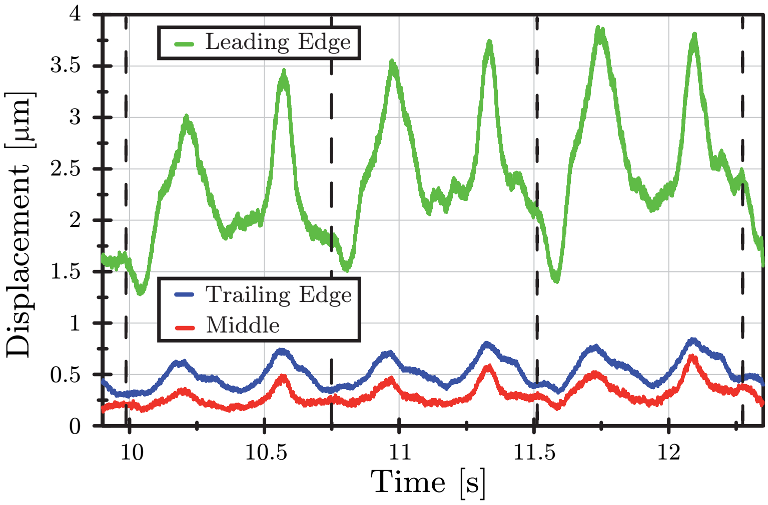

Figure 5.12.: Zoom of the filtered RMS of the ECSs over three revolutions during squeal event.

A comparison with the non-squealing measurement shows that the unfiltered but offset-corrected signals of both measurements have a similar behaviour. The low frequency displacement vibration due to disc run-out and DTV is clearly visible, but the signals of the squealing measurements show superposed the already discussed 2.1 kHz vibration, see Fig. 5.13.

Figure 5.14 shows a detailed zoom of these additionally offset-adapted signals. During squealing, the ECSs signals from trailing edge and leading edge vibrate in phase, the middle opposite in phase. The vibration amplitude at the trailing edge is significantly higher. If there is no squeal, also a vibration with a frequency of about 2.1 kHz is visible, but all three sensors vibrate in phase. This leads to the assumption that in this case the pad performs a rigid body motion. The amplitudes are also about one order of magnitude smaller compared to the squealing measurements.

For the further analyses, the time period from eight to ten seconds from both measurements, the non squealing (Fig. 5.7) and the squealing (Fig. 5.8), is used. Figure 5.15

---

[4] This effect is similar to the excitation of violin strings with a violin bow.

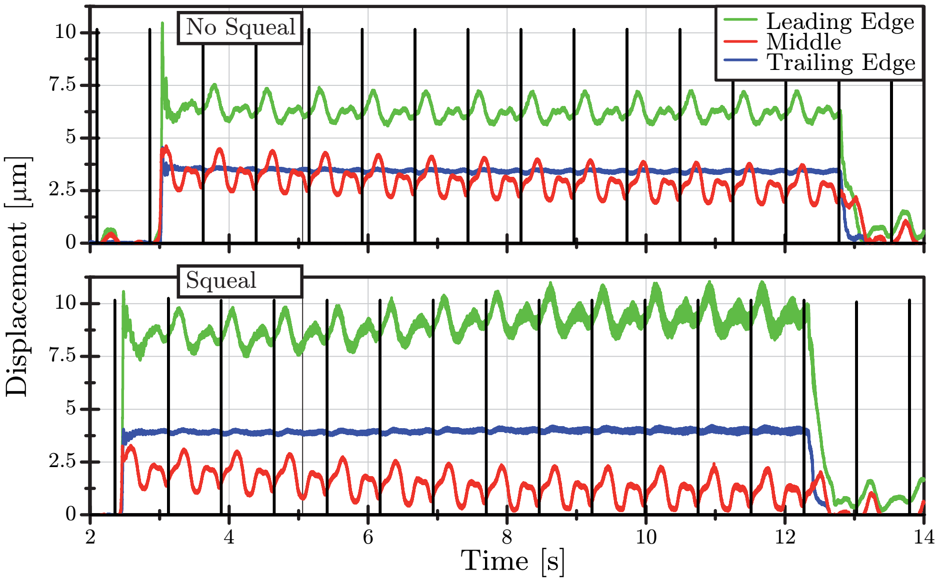

Figure 5.13.: Comparison of the offset-corrected ECSs during non squealing (upper) and squealing (lower) operation points. The vertical lines indicate a revolution.

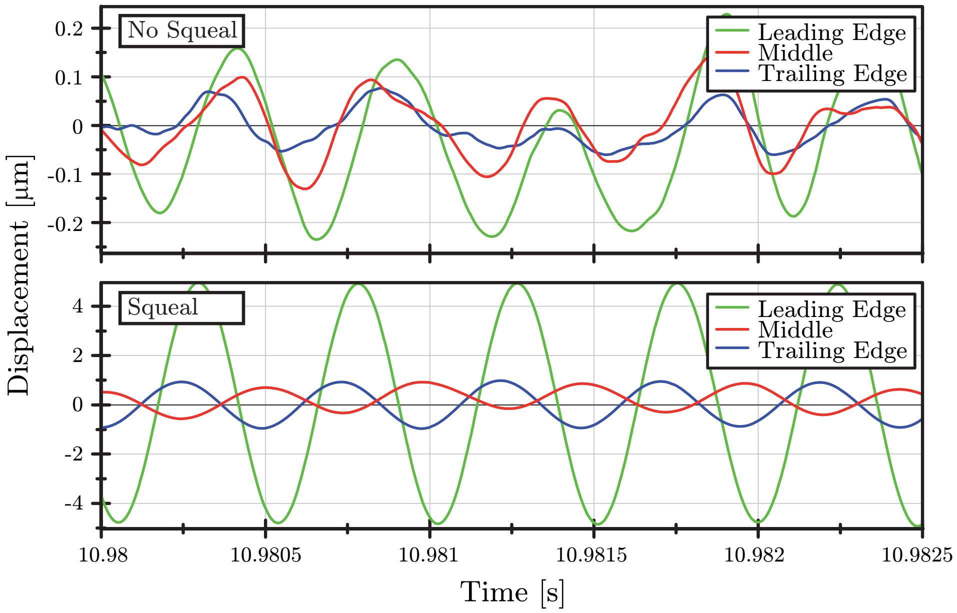

Figure 5.14.: Zoom of filtered and offset-adapted ECS signals during non squealing (upper) and squealing (lower) operation points.

left shows the FFTs of the microphone signals during this time period. For better visibility and comparability, the same ordinate scaling is chosen. As a result, the reached amplitude peak at 2.1 kHz is cut off in the plots showing the squealing situation.

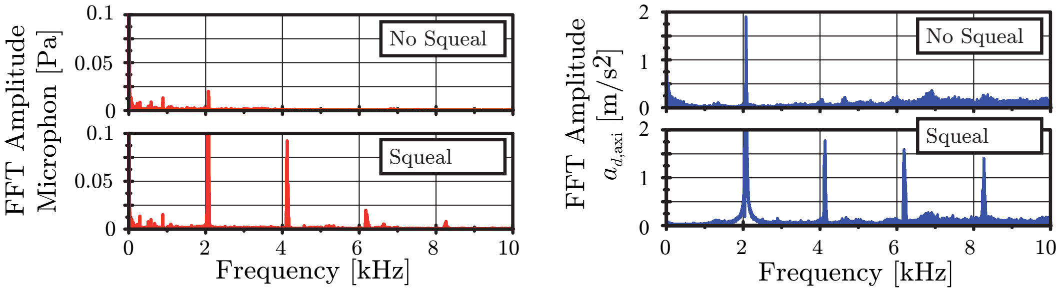

Figure 5.15.: FFTs of the microphone and disc axial acceleration signals during non squealing (upper) and squealing (lower) operation points.

The evaluated FFT amplitude of the 2.1 kHz signal is 0.8 Pa in the squealing brake case. An amplitude at 2.1 kHz is also observable when the brake is not squealing, but the amplitude is quite small. To be more precise, the amplitude at squealing conditions is approximately 32 times higher. In addition, the first, second and even the third harmonic vibrations (at 4.2 kHz, 6.3 kHz and 8.4 kHz) are only observed at the squealing operating point.

Figure 5.15 right presents a similar result, which is obtained by investigating the axial acceleration of the disc. During squealing, the evaluated FFT amplitude peak at 2.1 kHz is about 33 times higher compared with the amplitude at non squealing conditions. Again, if squeal is present, the first, second and third harmonic vibrations are visible.

The FFT analyses of the friction force and the ECSs deliver similar results: also at the non squealing measurement, a (little) amplitude at 2.1 kHz is visible, but during squealing this amplitude is significantly larger. The 2.1 kHz amplitude value of the friction force is about 26 times larger and of the ECSs about 30 times larger. The first three harmonic vibrations are also observed with the friction force pin, but at the ECSs only the first harmonic vibration can be determined, see Fig. 5.16.

The reason for this lies in the type of the measured quantity. An acceleration sensor measures the acceleration, but an ECS measures a displacement. For example, a vibration sinusoidal acceleration signal a is given by

$$a = A\sin(\omega t), \tag{5.2}$$

where A denote the amplitude, ω the circular frequency and t the time. Through integration, the velocity v and furthermore the displacement s result

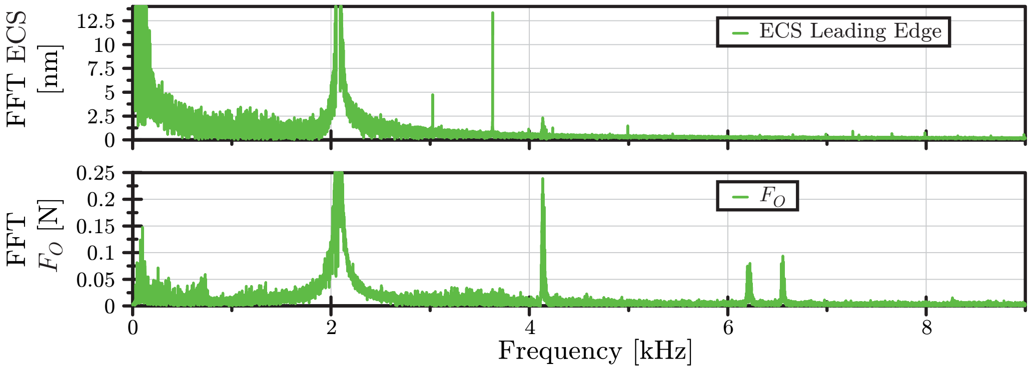

Figure 5.16.: FFTs ECS at trailing edge (upper) and outer friction force (lower).

$$v = \int a\mathrm{d}t = -\frac{A}{\omega}\cos(\omega t) + C_1, \tag{5.3}$$

$$s = \int v\mathrm{d}t = -\frac{A}{\omega^2}\sin(\omega t) + C_1 t + C_2, \tag{5.4}$$

$$s = -\frac{A}{4\pi^2 f^2}\sin(\omega t) + C_1 t + C_2. \tag{5.5}$$

The C_1 and C_2 are the integration constants. Thus, the displacement amplitude equals the acceleration amplitude divided by the square circular frequency. The resulting effect is explained with an example: a body vibrates with two oscillating frequencies at 2 kHz and 4 kHz. The measurement using accelerometers shows, that the two (acceleration) amplitudes are equal in size. However, the same vibration measured with displacement based sensors, hence ECS, results in unequal amplitudes. The amplitude at 4 kHz is due to the division with ω^2 only one-quarter of the amplitude at 2 kHz. This results in a lower *Signal to Noise Ratio* (SNR) of the ECSs at higher frequencies and due to this, the higher harmonic vibrations measured with acceleration based sensors cannot be detected using the displacement based ECSs. As a result, the limit frequency of the eddy currents sensors for this case of application is approximately 6 kHz.

In Fig. 5.16 some other frequencies are also visible. At the FFT of the ECS there are additional frequencies at about 3 kHz, 3.6 kHz and 5 kHz. The FFT of the friction force shows additional frequency at about 6.5 kHz, 19.7 kHz and 32.8 kHz. Detailed studies of these frequencies confirm that they are independent from the applied brake pressure, thus they are always present in the measurement and therefore identified as interference frequencies.

As already mentioned, the vibration at the squealing frequency (about 2 kHz) is also observed at the non squealing measurement. An explanation for this might be, that the main excitation/instability mechanism is always present. However, the feed-in energy due to the instability mechanism is not always strong enough to exhibit audible noise.

Only at certain operating points is the system excited enough and in an imperfect manner to become instable and to emit audible squealing noise.

5.2.2. Limit Cycles

Varying Limit Cycle

For the later presented sensitivity analysis, a total of 180 brake applications are performed. Thereby, an interesting phenomenon could be observed several times: immediately after brake pressure application, the system starts to squeal at a constant SPL which equals a constant limit cycle vibration. However, sometimes the SPL, hence the emitted noise, varies during one brake application. Figure 5.17 shows the microphone signal of such a measurement.

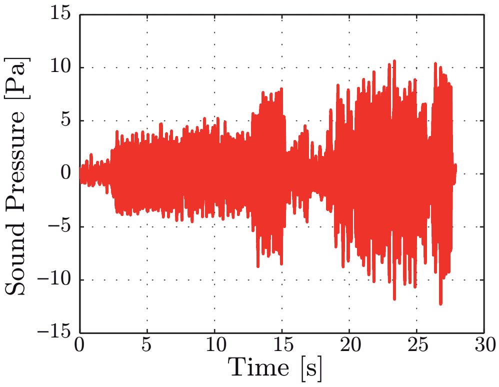

Figure 5.17.: Measured microphone signal for a varying noisy brake application.

In the presented measurement, the brake system rotates at a steady speed equal to 20 kph (2.6 rpm) and a constant brake pressure of 15 bar is applied after 2.5 s. The brake system immediately starts to squeal and after about 1.1 s reaches a constant level at approximately 107 dB. At 12.5 s the system changes abruptly to a noisier level (about 111 dB), but just for a short time to drop afterwards to a SPL below 104 dB. Finally, the system starts to squeal again on a higher level (113 dB) until the end of the brake application.

The squeal frequency equals 2060 Hz during the complete measurement. Due to the friction, the brake system heats up. Thereby, the friction coefficient changes from 0.6 to 0.8. This increase of about 30 % can also be observed with the friction force measuring pins. As a result, the excitation changes. Depending on the excitation due to the friction, certain limit cycles are reached. Thereby, a higher friction coefficient does not necessarily lead to a higher limit cycle or more noise. However, there is a tendency for this to occur.

Figure 5.18 shows the FFT of the noise signal at different time steps. The time range τ equals one second. The ordinate axes of the plots are equidistant formatted and accordingly, the changes over time can be seen. The squeal frequency as well as the first and second harmonic are marked with a dashed line.

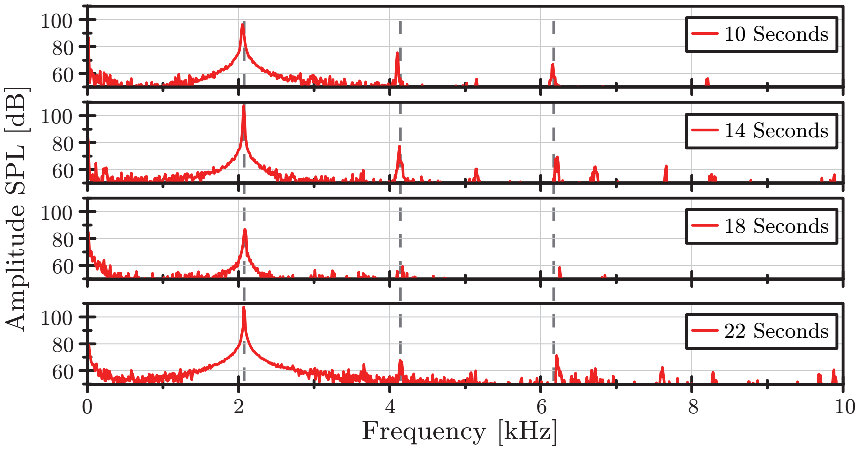

Figure 5.18.: FFTs of the microphone signal at different time steps.

The FFTs of the acceleration sensors mounted in the cooling ducts, on the caliper and on the brake pads look similar to the FFT of the microphone. However, the given limit frequency of the accelerometers equals 8 kHz. Consequently, sensors with a higher maximum frequency, such as the friction force measuring pins, are used for further investigation. The measured signals at the inner and the outer side show similar results in the frequency domain. In the time domain the signals vibrates in opposite phase. Because of this, only the results of the outer friction force measuring pin are presented in the following.

Figure 5.19 shows the FFTs of the outer friction force measuring pin at the same different time steps. For better visibility, the logarithm ($\log(F_O)$) is plotted in the figure. The (dominant) squeal frequency at 2.1 kHz as well as the first and second harmonic vibrations are marked with dotted lines. In addition, a higher frequency vibration at 13.1 kHz and the first and second harmonic vibration of it at 26.2 kHz and 39.3 kHz are visible. They are marked with dashed lines. During the measurement, the amplitudes of these vibrations hardly change.

During loud squeal, side bands (marked with dashed/dotted lines) occur next to the vibration at 39.3 kHz at a distance of 2.1 kHz, which equals the squeal frequency. There is a correlation between the amplitudes of the side bands and the squeal amplitude. Thus, a smaller squeal amplitude results in smaller side bands amplitudes. This means that the vibration at 39.3 kHz acts like a carrier frequency, which is modulated by the squeal frequency. Hence, there is some kind of interaction between those two vibrations.

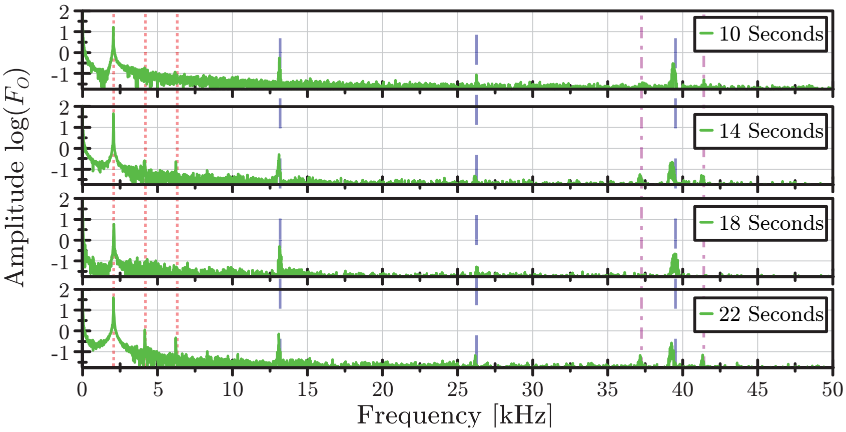

Figure 5.19.: FFTs of the outer force measuring pin at different time steps.

Further investigations show that the high frequency vibration and the harmonic vibrations belonging to it are also present if no brake pressure is applied, but at least brake drag torque is present. Figure 5.20 presents the chronological sequence of the FFT of a measurement without applied brake pressure. The velocity changes from 50 kph to 20 kph and back. The ratio of the maximum and minimum velocity equals 2.5.

It can be seen that the previously detected higher frequency vibrations are velocity dependent. The vibration with the highest amplitude and the lowest frequency changes by exactly the same ratio as the velocity, hence from 32.8 kHz to 13.1 kHz. The other two vibrations are now clearly determined as harmonic vibrations of this vibration. An extrapolation of this result shows that the lowest (main) velocity dependent frequency equals the usual obtained squeal frequency of 2.1 kHz at a velocity of approximately 3 kph. During the experiments, the investigated brake system shows a noisier behaviour at low speeds and just before the test rig (hence the vehicle) stops.

As a result, a velocity dependent vibration and their associated harmonic vibrations could be observed. During squealing, the second harmonic vibration acts as a carrier frequency and is modulated by the squeal frequency. In addition, at low speeds the frequency of the velocity dependent vibration equals the squeal frequency. The noisy behaviour of the brake system at low speeds can be explained by this effect. In addition, the squeal frequency could be also observed at non squealing measurements. This leads to the assumption that at low speeds the velocity dependent vibration and the squeal frequency are coupled which results in brake squeal.

Self-stabilising

Another measurement is performed at constant brake pressure and velocity at 15 bar and 20 kph (hence 156 rpm or 2.6 Hz). Immediately after brake pressure application at

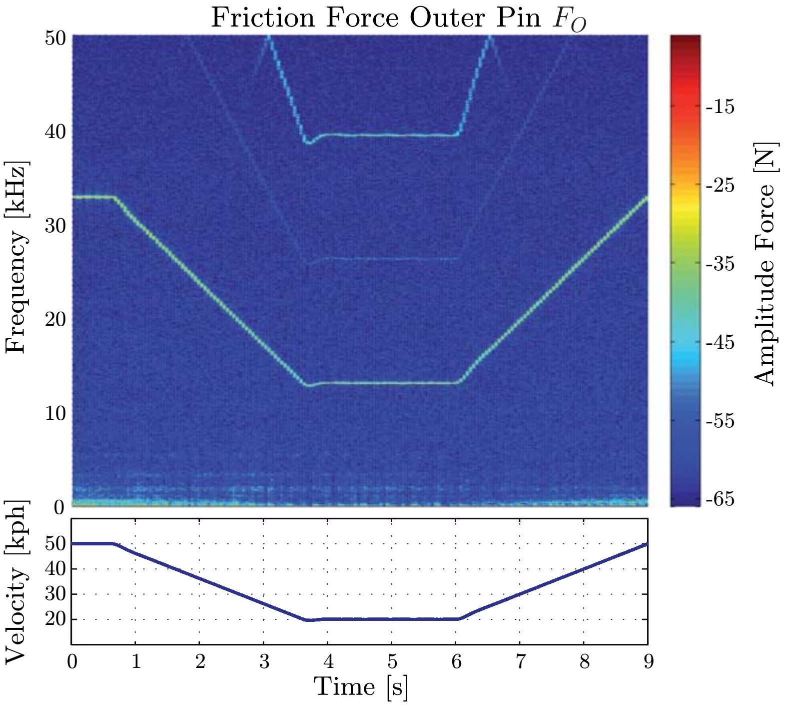

Figure 5.20.: FFT over time of the outer friction force measuring pin, no brake pressure applied, velocity varied.

1.2 s, the system starts to squeal constantly at 2.1 kHz and 100 dB(A). After 16 s the brake stops to squeal, although nothing has actively been changed. The brake stays quiet until the end of the brake application at approximately 40 s. Figure 5.21 shows the measured microphone signal p and brake pressure signal p_{hyd}.

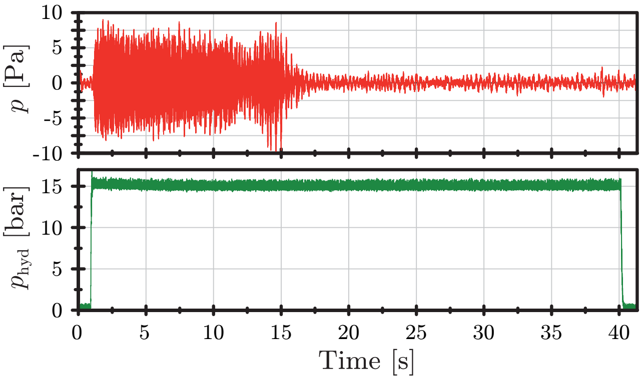

Figure 5.21.: Microphone (upper) and brake pressure (lower) signal.

Figure 5.22 depicts the FFTs of the friction force measuring guide pin at three different times. At 14 s the systems squeals at its noisiest point, at 16 s it starts already to quieten and finally at 18 s no audible squeal can be recognised. Within a time period of four seconds, the system stops to squeal during the constant brake pressure application. Figure 5.22 left shows the complete gained spectrum from 0 kHz to 50 kHz.

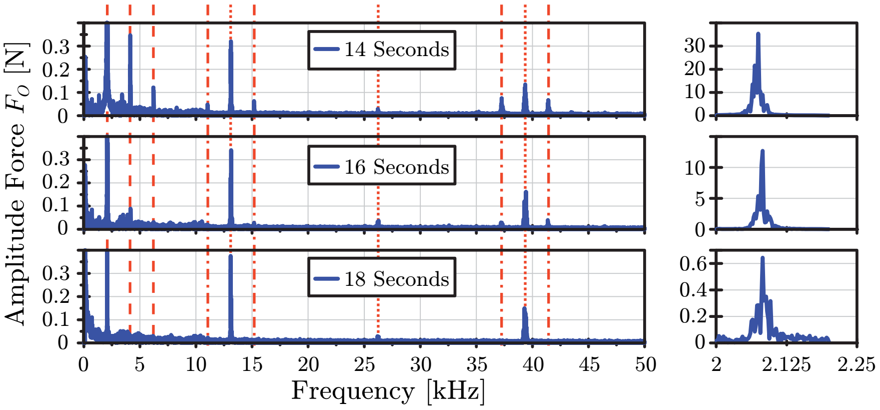

Figure 5.22.: FFTs of friction force measuring guide pin for three different times.

For better visibility the ordinates are equidistant. The dominant (squeal) frequency at 2.1 kHz as well as the first and second harmonic vibrations belonging to it are marked with dashed lines. The rotation speed dependent vibration at 13.1 kHz and again first and second harmonic vibrations are marked with dotted lines. Finally, side bands next to the vibrations at 13.1 kHz and 39.3 kHz are marked with dash-dotted lines. The side bands have a distance in the frequency domain which equals the squeal frequency. As a result, the vibrations at 13.1 kHz and 39.3 kHz act as carrier frequencies which are modulated by the squeal frequencies.

Figure 5.22 right presents the zoomed amplitude peak at 2.1 kHz at the three different time steps. Now, the ordinates are not equidistant scaled. Within the four seconds, the FFT amplitude drops from 35 N to 0.65 N. Hence, the amplitude is reduced to less than one-fifties without changing actively the system.

The development of the friction coefficient between brake disc and pad during the measurement is shown in Fig. 5.23. From brake start (which equals squeal start) until the system starts to quieten at 16 s, the friction coefficient increases. Then it remains at an almost constant level for 30 s when it begins to increase again. During braking, the temperature of both pads and the disc changes almost linear from 70 °C to approximately 130 °C.

A polar axis plot shows the development of the RMS value of the axial disc acceleration, see Fig. 5.24. Thereby, the time period from 13 s to 18 s is depicted. The location

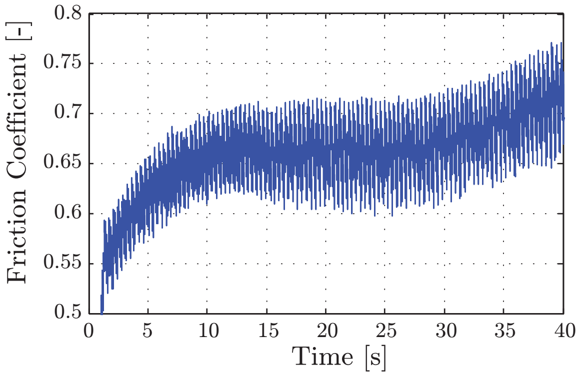

Figure 5.23.: Development friction coefficient during brake application.

of the pad is at 0 ° and the trailing and the leading edges are indicated by the lines at ±18 °. At the beginning, hence the curves with the highest RMS acceleration values, a peak every approximately 60 ° can be noted. This implies a (0,3) ODS. The largest amplitude is just before the leading edge at approximately 310 °.

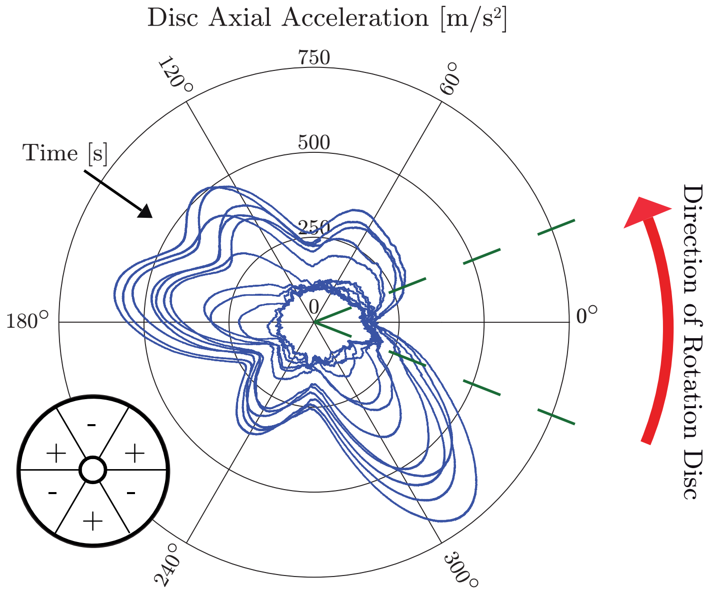

Figure 5.24.: Polar axis plot of decreasing RMS value of disc axial acceleration signal from 13 s to 18 s.

In the considered time period, the acceleration signal decreases (almost) steadily with every rotation. The vibration and its shape decrease significantly. However, the system still vibrates, but constantly along the disc and no ODS can be determined. The only exception is right after the leading edge at 342 °. There, a small peak is always visible.

The assumption is that this steady peak is due to sprag-slip effects. Thus, a continuous excitation is always present.

5.3. Sensitivity Analysis

5.3.1. Set-up

The possibilities with the newly developed sensors as well as the suitability of different counter measures is evaluated with a sensitivity analysis. Thereby, one single parameter of the brake set-up is changed between each set of brake applications. This allows the determination of the individual parameter's influence on the squeal behaviour. Hence, with every brake set-up a set of brake applications is performed. Table 5.1 provides an overview of this set.

Table 5.1.: Performed set of brake applications.

VELOCITY [kph]	BRAKE PRESSURE [bar]	WATER side
20	15	
20	20	
20	30	
50 ... 5	15	
5 ... 50	15	
20	10	inner
20	10	outer
25	25	inner
25	25	outer

To evaluate the brake pressure influence, three brake applications at constant speed equal to 20 kph are performed. Thereby, the brake pressure varies (15 bar, 20 bar and 30 bar). Furthermore, brake applications at constant brake pressure equal to 15 bar at varying speeds are performed. The system decelerates with constant $-3.3\,\mathrm{m}/\mathrm{sec}^2$ [5] from 50 kph to 5 kph for the first brake application and accelerates with constant $2.5\,\mathrm{m}/\mathrm{sec}^2$ [6] from 5 kph to 50 kph for the second. Consequently, the influences of different rotating speeds as well as accelerating and decelerating relative sliding velocities are investigated.

Additionally, the influence of a decreased friction coefficient is investigated. For this purpose, water is sprayed on the disc surface during a brake application. This is done for two different brake applications at constant speeds and constant brake pressures (20 kph/10 bar and 25 kph/25 bar).

---

[5] Equals one-third of gravitational acceleration.

[6] Equals one-quarter of gravitational acceleration.

After every set, one of the six changeable parameters of the brake set-up is varied. The possible modifications are:

Brake pad material: For the investigation the *Sinter B* and the *Organic B* pads are used. The difference of these is explained in Chap. 4.3.2.

Spring: A spring is attached at the top of the brake pads. This spring presses the pads slightly against the guide pins.

Claw Shim: These special shims are glued on the pad backplate. On these shims, claws are attached which are pressed inside the pistons of the caliper. Therefore, the pads are fixed to the pistons.

Chamfer: The sintered brake pads are manufactured without a chamfer. The available organic pads already have a chamfer. Thus, the influence of adding a chamfer is only investigated at the *Sinter B* brake pads.

Slot: The influence of cutting a slot in the friction material of the brake pads has been investigated.

Damping Shim: The available organic brake pads already have a damping shim glued onto the pad backplate. They were removed in order to study their influence.

In addition, the investigations are performed on a test rig inside a climate chamber. This allows studies at three different environmental conditions (warm and dry, normal, cold and wet).

An overview of the used sensors is presented in Tab. 4.1. Explanations about the nomenclature of the measurements and the sensors as well as the graphical depictions of the later presented results can be found in the Appendix, Chap. A.4.

5.3.2. Correlation

Sensor signals correlation is used e.g. in road testing. Thereby, two sensor signals are correlated to determine the similarity between them and, as a result, statements can be made about the connection/coupling of them. During road testing, a microphone is installed next to the driver. The microphone detects if a squealing brake application is performed. Thereby, the measurement analysis system is triggered by the applied brake pressure. Acceleration sensors are mounted on the brake caliper at each wheel of the car. To discover which of the four brake systems of the car squeals, the correlation of the acceleration sensor signals to the microphone signal is calculated.

The obtained signals from the test rig measurements are analysed regarding their correlation in the time domain. During squealing, all sensors show a dominant vibration at the squeal frequency. As a result, all signals show a strong correlation to each other and no further information can be gained.

As a consequence, the correlations of the measured sensor results (maximum and average values) of the different sensor signals for the performed brake applications are investigated. The measurement results of every sensor are written in a sensor results vector $\mathbf{S}_i$. These vectors are collected in the result matrix $\mathbf{T}$, whose rows are the performed brake applications and whose columns are the different sensor results vectors $\mathbf{S}_i$. In particular the correlation of sensor results vectors to the determined *Squeal Ratio*[7] and the microphone results vector are investigated. The correlation of the sensor signals is calculated in two steps:

1. The covariance matrix $\mathbf{C}$ of the result matrix $\mathbf{T}$ is calculated.
2. The correlation matrix $\mathbf{R}$ of the covariance matrix $\mathbf{C}$ is charged.

Consequently, the value $\mathbf{R}(i, j)$ of the symmetric correlation matrix $\mathbf{R}$ gives the correlation between the sensor results vectors $\mathbf{S}_i$ and $\mathbf{S}_j$. The resulting values are between $[-1, 1]$. A strong correlation between two sensors is indicated by a value above 0.7. A weak/low correlation is given by a value below 0.4. Negative values indicate an inverse correlation. For further information see e.g. [162].

5.3.3. Results

The influence of several system parameters as well as the suitability of different countermeasures are evaluated. To simulate a friction coefficient reduction water is sprayed on the disc surfaces. Consequently, the friction coefficient is reduced by 23 % to 39 %. In the tests, it could be observed that a squealing brake stops squealing immediately when the spraying started. In some brake applications, squealing started again after several seconds. However, the reached SPL is reduced by approximately 30 %.

Compared with the results of Chap. 2, a lowering of the friction coefficient results in a smaller amplification rate and limit cycle. Thus, the vibration of the friction force as well as the disc axial acceleration has to be smaller. Exactly this can be observed in the measurement and is marked with rectangles in Fig. A.8 and Fig. A.9.

The investigated brake disc shows a noisy behaviour at a brake pressure of 30 bar. Figure A.10 shows the measurement results for these brake applications. The upper part presents the measurement results of the *Organic B* brake pads, the lower part the *Sinter B* pads. The organic brake pads have a better squeal behaviour because they have a lower friction coefficient and are softer.

The ECS measures the displacement of the disc and the pad. Thereby, the relative values determine the relative motion of the pad due to the brake application. Consequently, a less stiff pad results in larger displacements. This is marked with an ellipse in Fig. A.10.

---

[7] Is the calculated ratio of squealing time to braking time of every brake application.

It was observed that, when using the sintered brake pads, the relative displacement of the leading edge exceeds the trailing edge. When using the organic brake pads, this effect is reversed. Hence, the angle between disc surface and pad surface is different which also influences the squeal behaviour. Similar results have been obtained by Fieldhouse et al. [56].

In addition, it can be observed that the claw shims reduce the disc axial vibration and the vibration of the friction force, marked with rectangles in Fig. A.10. There is only a minor influence on the squeal ratio, but the SPL is reduced by approximately 20 %. Thus, the claw shims mainly influence the reached limit cycle of the system.

Figure A.12 presents the correlation coefficient of the sensors. Thereby, only the sensor results of measurements performed with sintered brake pads and including claw shims are investigated. Usually, the obtained correlation plots show a high correlation of all installed TASs, see e.g. Fig. A.11.

However, if only measurements with claw shims are investigated, the gained disc tangential acceleration signals partially show a negligible correlation to the other TASs signals. This is marked in Fig. A.12 with three ellipses. The sectors of the sensor signals according to disc, pad and caliper are marked. The disc tangential acceleration signals correlate only weakly to moderately with the acceleration signals of the pad. Consequently, the claw shims decouple the tangential motions of pad and disc.

As a result of installing the claw shims, the vibration amplitudes of the ECS in the middle (”P2P EC M”) correlate moderately, but only with the disc tangential acceleration. The correlation to the vibration amplitudes of the other TASs signals (”P2P Triax”) is negligible. The other two ECS vibration amplitude signals correlate strongly with the vibration amplitudes of all TASs. This is marked with a rectangular in Fig. A.12.

The sensitivity analysis is performed to investigate the possibilities of the newly developed sensors as well as to find out proper counter-measures for the investigated brake system:

- A decrease in the friction coefficient significantly reduces the squeal behaviour regarding occurrence and SPL.

- Damping shims reduce the SPL, but no significant impact on the squeal occurrence could be determined.

- Chamfers on the pad results in a smoother lead in into the contact area. In addition, the contact area of the pad is reduced, which increases the contact force per area unit. This results because the (total) normal contact force F_N, which depends on brake pressure p_{hyd} and piston area A_B, is unchanged. As a consequence the excitation is changed which results in a lower squeal occurrence.

- Variation between sintered and organic brake pads changes the current friction coefficient and the contact stiffness. In addition, the sintered brake pads are stiffer and thus have a higher eigenfrequency. As a consequence, the eigenfrequency of the pad is shifted towards those of the caliper which results in a noisier brake.

The friction force measuring guide pins provide a further insight into the friction contact. In addition, the strain gauges on the side of the pads provide at least principle statements. It could be proved that also the friction material of the pad vibrates in the direction of the acting friction force. In addition, the developed measurement system provided not only new possibilities for in-depth investigations, but is also capable for matrix test series or sensitivity analyses.

6. Development Tool for Quiet Brake System Design

6.1. General

The results of the investigations lead to a proposal for a brake system development process. The main problem of a squealing brake system is that its negative acoustic behaviour is usually detected when the first prototype parts are available and tested. The tests take place either by means of road testing with prototype vehicles or are carried out on test benches. Because prototype parts are first available towards the end of the vehicle development process, the possible counter-measures are limited. Mostly, chassis and suspension are already optimised regarding vehicle dynamics and comfort and can no longer be modified.

In general, possible modifications are limited to the brake system, hence brake disc, brake pad and caliper. Consequently, the natural frequencies of those parts should be considered from the beginning and, if possible, similar natural frequencies avoided.

6.2. Proposed Development Process

The proposed development process starts at the latest at the moment that squeal is detected experimentally on a test rig or in a prototype vehicle. Thereby, the squeal frequencies are determined by using a microphone. Knowing the occurring squeal frequencies, the following development process is proposed. It consists of six steps:

First Step: Generation of an Appropriate FEM Model

In the beginning, a small model consisting only of brake disc, brake pads and caliper provides *Complex Eigenvalue Analysis* (CEA) results with sufficient accuracy. If possible, the brake pads and the disc should be modelled using hexahedral elements. Additionally, a coincident mesh in the contact area is recommended[1]. Slotted and/or drilled brake discs should be simplified, at least in the contact area, to have a closed contact surface.

The brake pad material is anisotropic. This means that the mechanical properties depend on the direction of loading. An example of such a material is wood. This has

---

[1] In the meantime some FEM software developers claim, that a coincident mesh is not necessary anymore.

to be taken into account using at least an orthotropic material law. Nevertheless, every part has to be separately validated using experimental modal analysis.

The calculation of the CEA usually results in too many unstable solutions. However, only those instabilities which are in the range of the measured squeal frequencies need to be considered. If there are too few instabilities, calculations with an increased friction coefficient should be performed and simulations using reduced integration because *shear locking* may have occurred. Additionally it has to be noted that, while a high negative damping is a good indicator that a frequency is important, this criteria alone is not sufficient.

Next, the brake pressure distribution should be checked. Most of the brake squeal algorithms apply the brake pressure in ten steps. This procedure is time intensive. Investigations on the current model show, that there is a negligibly small variation in the results if the brake pressure is applied in one step. However, this modification has to be checked once before implied in the calculation algorithm.

Second Step: Experiment

To check the accuracy of the calculations and to validate them, the brake system has to be tested on a brake test rig. Thereby, different test methods are possible. The simplest test set-up is a brake dynamometer[2]. Figure 6.1 shows such a test set-up which is mainly used for testing the brake performance and the brake fade of the brake system. Only brake disc, brake pad and caliper are tested.

Figure 6.1.: Brake dynamometer.

---

[2] Also known as flywheel mass test rig.

The advantage of this test is its fast and easy application on the test rig. However, the boundary conditions, hence the mounting of the disc and the caliper, are usually too stiff for acoustical investigations. Additionally, the suspension has a not negligible influence on the squeal behaviour. Consequently, the boundary stiffness of the suspension parts has to be taken into account. Thus, acoustic brake tests are usually carried out on a quarter-vehicle test bench or using a test rack including the whole vehicle axle. In this work, a complete vehicle axle was tested on a test bench, see the previous Chap. 4 and Chap. 5.

First of all, a SAE J2521 squeal noise matrix test [143] should be performed. The results of this test already provide a first insight regarding critical brake applications. The occurrence of squeal and the system parameters in this situation, hence brake pressure, velocity and pad temperature, are recorded. Knowing the squealing brake conditions, the system can be investigated in detail to validate the FEM model. Experimental modal analysis and *Transfer Path Analysis* (TPA) provide a first validation. After this it is necessary to compare the *Operational Deflection Shapes* (ODS) of the three main parts of the brake system:

Brake Disc: The ODS consists of out-of-plane and in-plane vibrations of the disc. Therefore, it is necessary to measure the displacement (or velocity or acceleration respectively) in all three directions. This can be done using double-pulsed holographic interferometry [57, 59, 156], a three dimensional scanning vibrometer [22, 61, 116] or triaxial accelerometers in the cooling ducts of the disc [108]. Since of the rather low limit frequency of accelerometers (approximately 8 kHz), they are mainly used for squealing noise below that value.

The signal transmission from the rotating part is provided by telemetry or slip-rings. Their advantage is that they can measure the ODS of the complete brake disc. In contrast to that, the optical measurement systems must be able to ”see” the entire disc, which often results in a space problem on the test bench. Additionally, the part of the disc under the caliper is never visible and the shape there cannot be determined.

Brake Caliper: Generally, several accelerometers or three dimensional scanning vibrometer determine the ODS of the caliper. Usually the determination of the brake caliper ODS is less critical compared to brake disc and pads.

Brake Pads: Typically the brake pads are difficult to access for measurements, especially at fixed caliper brake systems. Mainly accelerometers are used, if possible regarding space.

Chapter 4.1.2 provides a literature review of the various measurement systems. Furthermore, Chap. 4.2.3 presents a new method using *Eddy Current Sensors* (ECS) for absolute displacement measurement between brake pad and caliper.

In addition to the SAE J2521 standard, tests regarding different environmental conditions should be performed. Therefore, the test rig has to be inside a climate chamber. As a result, it is possible to test squeal phenomena such as *morning squeal*, which occurs in wet and cold conditions. Morning squeal is caused by geometrical changes in the system due to different materials (thermal expansion) and by light surface corrosion (rust formation).

Third Step: Comparison FEM and Experiment

The FEM simulation shows the modes which are able to vibrate instable. Contrary to this, the experiments show the behaviour of the system, hence the actual vibrating modes, which have to be treated. Measurement delivers the frequencies and ODS of the critical vibrations. These have to be compared with those of the CEA. Consequently, it is possible to identify the relevant and thus important complex eigenvalues.

If the results from FEM and experiments differ too much, the FEM model has to be expanded. Also the suspension parts (wheel carrier, trailing arm, steering rod, etc.) should be included in the model. The expansion leads to a more accurate model because the boundary conditions are now included in more detail. After validation of the model the brake squeal counter-measures can be first tested in virtual form before being implemented in practice on the test rig.

Fourth Step: Counter-measures

In the current work one brake system was investigated in detail, also regarding counter-measures. The suitability for the investigated brake system is presented in Chap. 5.3. Because every brake system has its own characteristics, no general statement as regard the usability of one counter-measure or any sort of ranking can be made. Nevertheless, the most common and most successful used counter-measures should be briefly mentioned and discussed:

Reduce friction coefficient: Since friction is the main exciting mechanism this counter-measure almost always reduces squeal. However, the reduction also influences the brake performance, hence the resulting brake torque is reduced. In order to balance this, the friction area or the radius of the brake disc has to be increased. Both result in a larger brake system, which is heavier and more expensive.

Increase damping: The most frequently used counter-measure is to increase the damping of the pad by adding a damping shim on the backplate of the pad. Knowing the ODS of the pads helps in the choice of an applicable shim design, see e.g. [44, 62, 66, 67].
Lubricants are added to the mixture of the friction material to soften it which thus increases the damping. This leads to a softer ”pedal feeling” and increases the wear of the pad, cf. [33].

Change excitation: The design of the brake pad can be varied to change the excitation. For this reason, chamfers are used which induced a better lead into the disc/pad contact at a macro level, but they also reduce the contact area. Another possibility is to add slots in the pad. However, this can also worsen the behaviour and should always be tested on a test rig, see e.g. [154]. For example Hiller [79] presents the results of a sensitivity analysis regarding different brake pad materials and pad shapes.

Separate natural frequencies: If the components which are coupled are known, their eigenfrequencies can be shifted. Some added extra mass on the caliper acts as a dynamic vibration absorber (Tilger) and shifts its natural frequency, see e.g. [135]. Another possibility is to stiffer the brake disc which could be done by changing the shape of the cooling ducts. Figure 1.3 shows three different cooling ducts designs. Regarding Spelsberg-Korspeter [151, 152, 153] a positive effect to reduce brake squeal is also obtained if the symmetries of the brake disc are broken.

Chapter 5.3 presents the results of the sensitivity analyses. The friction coefficient is reduced by spraying water on the brake disc. Thereby, the system stops squealing immediately. The damping effects are investigated by adding and removing damping shims. This results in a lowering of the emitted noise. Chamfers on the pads change the excitations on the system. The softer lead-in of the pad reduces the squeal occurrence. The organic and the sintered brake pads differ in their material properties. As a consequence of the higher stiffness of the sintered pads, the eigenfrequency is higher. Thus, the eigenfrequencies of pad are shifted towards the eigenfrequency of the caliper which results in a noisier brake system.

Fifth Step: Proof of the Counter-measures

The FEM model can test the different counter-measures in virtual form. Thereby, a change of the damping coefficients has to be considered. A proper counter-measure will decrease the value of the negative damping coefficient. After definition of appropriate counter-measures, these have to be tested on the test bench. Thereby, in-depth investigations of previously determined squealing brake conditions are used to evaluate the impact of the counter-measure on the system. However, for final release of a brake system, a matrix test such as the SAE J2521 should be performed. This is because the modifications may introduce new instabilities.

Sixth Step: Ensure Robustness

Sometimes, squeal issues can be successfully solved until the *Start of Production* (SOP), but after months of production a squeal problem arises. This is because of scattering in the production. Due to e.g. wear of the tools or small changes in material composition the characteristics of the brake system parts are changed which may lead again to instabilities [2].

6.3. Outlook

In order to explain some possible and recommended further work, the following statements should be considered. Generally a noisy brake system consists of a vibrating disc and an accompanying oscillating pad. As a result of the pad oscillation, the friction force vibrates inducing an in-plane vibration which mainly leads to an out-of-plane vibration of the brake disc. The amplitude depends on the structure of the brake system such as the stiffness of caliper or damping of the shims. Additionally, there is an influence due to the abutment of the pads.

Independent from the brake system design, the brake pad has to be able to move normal to the disc. In the investigated brake system, the pads slide along the guide pins. The friction between pad and pin may also influence the squeal behaviour. According to Fieldhouse et al. [56] a high abutment interface friction coefficient may lead to squeal because a higher offset of the normal pad motion is possible and thus a higher sprag angle occurs. However, this abutment interface friction also introduces some frictional damping into the system.

Finally, the two general observable main effects on brake squeal can be explained:

1. Noise usually appears at low brake pressures. Increasing the brake pressure results in a noise dissipation. The reason for that is that the pad vibration is suppressed. Thus, no friction force vibration is obtained and furthermore no squeal can be observed.

2. Brake shims work, at least for squeal issues at high frequencies. In that case the shims damp the pad vibration as well as the oscillating friction force.

Knowing these effects, proper counter-measures can be developed which have to be tested experimentally. Therefore, suitable measurement methods are necessary. In this work, several new and innovative measurement methods are developed, which are able to support the brake development process.

Computational power will further increase in the next years and the same applies to the possibility of virtual numerical methods regarding brake squeal. Nevertheless it can be expected, that a combination of simulation and testing will be still necessary due to the enormous complexity of the problem. The squeal behaviour can be predicted virtually but should be verified experimentally. Beside this, brake system engineers are faced with new challenges:

The development of more environmentally performing vehicles leads to new drive concepts such as hybrid or electric vehicles. These driving concepts recuperate electric energy during braking, which is used afterwards for driving. As a result, the frictional brake system will be used less and in addition mainly at low speeds and low brake pressures [16, 98, 142]. Finally, the new car concepts will have a lower general noise level which intensifies the brake noise problem. All these aspects make a robust brake design more difficult and increases the importance of this topic.

In 2009 Cantoni et al. [31] wrote in their comprehensive review of brake squeal as first sentence in the conclusion:

> *"Brake vibration and/or noise has been studied for almost 80 years with minor practical results."* [31]

This is considered as quite strictly formulated and only partially true. Much work has already been done which leads to a better understanding of the brake squeal triggering mechanism and to more reliable quiet brake systems. The "easy" problem of solving a pad sliding on a disc leads to non-linearities in the differential equations and all associated (mathematical and numerical) problems. Hence, there is still much research work to do in order to solve the *brake squeal* issue completely one day.

One new approach to ensure the acoustic robustness of a brake system are fuzzy logic methods. Thereby, the parameters do not have exact values, but are subject to uncertainties [77]. This can also be applied to brake system simulations and was e.g. done by Haag et al. [73]. As a result, it is possible to investigate the influence of those uncertainties and the possibility of designing a robust brake system regarding squeal is increased. Also this direction is worth to be continued.

7. Summary

The squealing of friction brake systems is an issue which has been investigated for several decades. The noise emitted by the brake system has a negative effect not only on the passengers, but also on the environment. This leads to high warranty costs for car manufacturers because customers are not willing to accept noisy brakes. As an outcome from an academic-industrial research cooperation, the present work deals with several experimental and numerical methods to investigate squealing brake systems.

Chapter 1 introduces the topic by presenting background information about the development process in automotive engineering, the design of brake systems as well as the state of the art in brake development regarding acoustics.

During braking, the velocity of the car is reduced by converting the kinetic energy into heat by friction. This process may excite the brake system in an imperfect manner and it starts to squeal. A squealing brake is considered as the result of a self-excited vibration due to one or more instability mechanisms. The frictional contact causes the brake system to become dynamically unstable and the result is noise.

Chapter 2 provides an overview of these different instability mechanisms and explains the declaring simplified analytical minimal models in detail. Such a simple model is easier to understand and gives a basic insight into the mechanisms. Most of the known minimal models consist of a mass supported by springs and dampers, which slides on a conveyor belt. Several theories for instability mechanisms exist which are categorised in the following:

Stick-slip: The static friction usually exceeds the sliding friction. For example, a mass sliding on a conveyor belt may perform alternately a sliding or a sticking motion on it. This mechanism is responsible for *moan* and *groan*, which appear if a vehicle stands downhill and the brakes are released gently. During brake squeal stick-slip effects on the micro-level may occur in the contact area.

Negative friction velocity slope: In classical friction laws, the sliding friction coefficient is assumed to be independent of the velocity. However, in the brake disc and pad combination, a negative friction velocity slope can be observed. Hence, a velocity reduction results in a higher friction coefficient. Consequently, the system may be excited into an unstable motion.

Mode-coupling: Due to the friction, two vibration modes in different directions may be coupled. For example, a brake pad can vibrate in axial and tangential direction of the brake disc. The pad is also supported in axial and tangential direction.

These mountings can be interpreted as visco-elastic ones and thus the pad has an eigenfrequency in axial and tangential direction. The resulting two modes of vibration may be coupled by the friction in an improper manner which results in instability.

Flutter instability: The resulting friction force acts in the contact area of brake disc and pad. If disc and pad vibrate, the direction of the friction force has to vary to follow the deflections of those. Thus, these forces are called *follower forces*. As a result, the friction force is not constant which may result in an excitation of the brake system.

Sprag-slip: This type of vibration is similar to stick-slip. It is usually described by a pin sliding on a conveyor belt. The pin may lock on the conveyor belt and it is deformed until the reacting force of the deformation exceeds the friction force. Then the pin no longer sprags, lift-off occurs and it relaxes until it is in contact again.

The main disadvantage of the minimal models is that they are usually designed to describe only one excitation mechanism and/or the influence of one single parameter. To obtain these minimal models, significant simplifications are made. The resulting models have little in common with a real brake system. Nevertheless, they are very useful to gain a basic understanding of brake squeal triggering mechanisms.

Additionally, an existing model is expanded to include two instability mechanisms which are *sprag-slip* and *negative friction velocity slope*. Furthermore, a quite realistic model of a brake system is investigated in detail and its simplifications made are critically discussed.

Chapter 3 discusses the *Finite Element Method* (FEM) which is used for brake modelling and to numerically investigate brake squeal. For brake squeal investigation, the complex eigenvalues of the FEM model of the brake system are of interest. The required calculations are usually performed in two steps. Firstly, a non-linear contact analysis calculates the brake pressure distribution in the contact area. Secondly, the *Complex Eigenvalue Analysis* (CEA) is done, but for this the system has to be linearised around a certain steady state.

The main problem of the CEA is that the simulation delivers all possible critical modes (eigenvalues) and their damping coefficients. Critical eigenvalues are indicated by a negative damping coefficient. However, the value of this coefficient is not sufficient for an indication for a critical squealing mode. A self-excited vibration can be described by the frequency, the amplification rate and the reached limit cycle. The negative damping coefficient equals the amplification rate.

The more important parameter for brake squeal is the reached limit cycle which equals the emitted *Sound Pressure Level* (SPL), hence noise. Consequently, a high limit cycle is more critical than a high amplification rate, but the CEA only delivers the amplification rate of a brake system. Investigations regarding the influences of a proper contact calculation and the chosen element type are performed. It can be summarised that contact calculation has a significant influence on the results of the CEA.

The CEA is a suitable indicator for the squeal *Ability* of brake systems. All possible critical modes are obtained using this virtual numerical calculation method. In contrast, experiments deliver the squeal *Behaviour*, hence how the system reacts in reality. Therefore, comprehensive matrix test series such as the SAE J2521 *"Disc and Drum Brake Dynamometer Squeal Noise Matrix"* test are performed. The SAE J2521 consists of 2321 different brake applications under varying operating conditions regarding velocity, brake pressure and pad temperature. The result of this test is a *squeal noise matrix* (SNM) and a *squeal noise occurrence* (SNO).

Chapter 4 presents different test methods to investigate brake squeal and explains the developed measurement system in detail. To test different brake pad materials SAE J2521 tests are performed by means of a disc brake of a passenger car. After such a matrix test series, critical brake conditions are known and the system can be investigated in detail.

Such in-depth investigations need an appropriate measurement system like it was developed in the present work. One requirement for examining the instability mechanisms is to measure vibrations as closely as possible to the contact area. This lead to the development of a friction force measuring guide pin. Owing to optimal design, this pin is qualified to measure the friction force in high resolution. Consequently, it is possible to measure a superposed vibration of the friction force which typically occurs during squealing.

The measuring method of this sensor is based on strain gauges. Strain gauges are also mounted on the side surface of the brake pads. This allows the shear strain of the brake pads to be measured. The measured strain also shows a similar high frequency vibration during squealing.

Further requirements concerning the measurement system are the determination of the *Operational Deflection Shape* (ODS) of brake disc and brake pad. Therefore, triaxial acceleration sensors are mounted in the cooling ducts of the brake disc. A slip ring transmits the signals out from the rotating disc. In addition, an incremental encoder ensures a precise location of the sensors. For measurement of the brake pad ODS, three contact-free measuring eddy current sensors are used. This allows a measurement of the relative displacement between brake pad and brake caliper. For proper ODS determination, additionally two acceleration sensors are mounted on the top of the brake pad.

Chapter 5 presents the results obtained from this measurement system. For instance, the friction force of the two pads vibrate opposite in phase during a squealing brake application. The motion of the brake pad is more or less random until squeal starts. At this time, all sensors of the pad show a vibration in squeal frequency. Investigating the motion of the pad, it can be noticed that the highest amplitude is always at the brake pad edge were a rotating point on the disc gets first in contact with the brake pad. A similar result can be seen on the accelerometers mounted in the cooling ducts of the disc. The antinode just in front of the contact area has the highest amplitude.

In addition, sensitivity analyses of the brake system are performed. Thereby, not only parameters of the brake system such as pad material, damping shim, chamfer, pad-spring, claw shims and adding a slot in the friction material, but also the environmental conditions are investigated.

To study the influence of a reduced friction coefficient, water is sprayed on the disc. This reduces the friction coefficient by approximately 30 %. Therefore, the excitation is reduced and in most cases no squeal occurs. If squeal does occur, the *Sound Pressure Level* (SPL) is reduced significantly (about 30 %). Furthermore, the brake system takes a longer time to reach a limit cycle. Hence, the reduced friction coefficient also clearly reduces the amplification rate of the system. The experiments confirm that there is a strong correlation between friction coefficient, reached limit cycle and amplification rate.

Additionally, it was observed by the strain gauges installed at the side surface that the brake pads vibrate significantly if the brake system squeals. An obvious vibration of the friction material in tangential direction of the disc can be noted. Mode-coupling, in which tangential and axial vibration of the pad are coupled, results in an unstable motion. Thus, it is proved that a vibration in sliding direction exists which influences (or is influenced by) the friction contact.

Claw shims are glued on the pad backplates and they claw into the pistons of the caliper. With the help of these claw shims, the vibration of disc, pad and caliper are decoupled and squeal occurrence as well as the reached SPL can be reduced significantly. An explanation for this is that the motion of the pad is reduced and additionally damped.

Finally, Chapter 6 presents a proposed development process to achieve reliably quiet brake systems avoiding trial and error corrections. Thereby, the findings of the previous chapters are taken into account. The proposed process consists of numerical and experimental methods. The obtained results from the virtual development have always to be validated with experiments.

This work presents a scientific investigation on brake squeal. Different approaches are introduced and discussed in detail. Among others, the development of a novel complex measurement system, including measuring points which are as close as possible to the contact/friction area, leads to a proposed development process.

By means of simulations and reproducible measurements, the influence of the different instability mechanisms can be determined. Considering this leads to concepts, as to how the system has to be changed to inhibit friction induced vibrations. As a result, this work presents a valuable contribution towards reliably quiet brake systems.

A. Appendix

A.1. Braking Dynamics

Ideal Brake Force Distribution

Figure A.1 shows a simplified depiction of a braking single-track model. In the illustration F_N represents the normal force and F_L the longitudinal force of a tyre (axle). The force acts on the front (index F) and on the rear axle (index R). The force of gravity G acts at the centre of gravity C_G. The vehicle drives with the velocity v and brakes with the dimensionless deceleration z, which is given by

$$z = \frac{\ddot{x}_{\text{veh}}}{g}, \tag{A.1}$$

where $\ddot{x}_{\text{veh}}$ is the deceleration and g represents the acceleration of gravity. The axes x_{veh} and z_{veh} determine the vehicle coordinate system with the origin at C_G. The variable H defines the distance between C_G and the road. The wheelbase is defined by L and L_F equals the distance from the front wheel to the force of gravity.

The following considerations are made under the assumption that only inertia forces and forces transmitted by the tyres are taken into account. The influences of air drag, suspension, engine and gear box on the brake force distribution are neglected. Con-

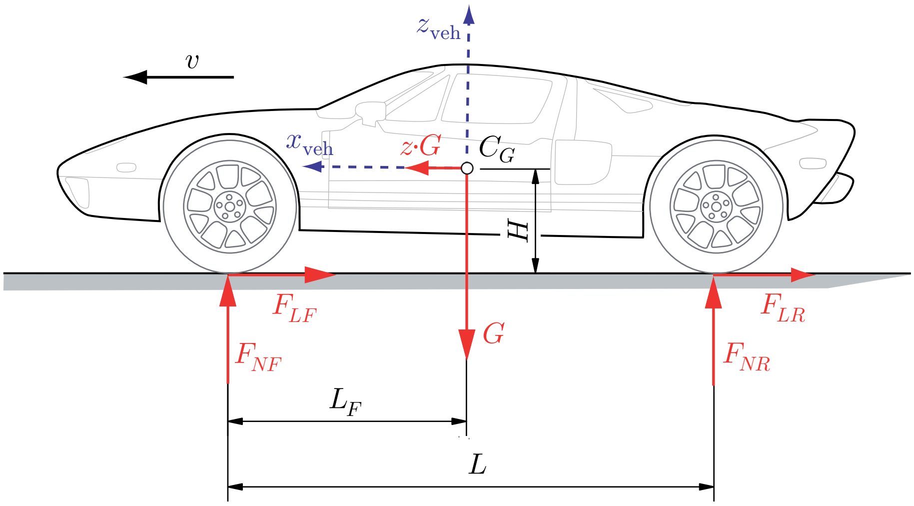

Figure A.1.: Acting forces at a braking vehicle.

sequently, also the inertia mass of the rotating parts is neglected. Furthermore, it presupposes that the position of the vehicle and thus the C_G does not change during braking. The linear momentum in longitudinal direction reads

$$z = \frac{F_{LF}}{G} + \frac{F_{LR}}{G}. \tag{A.2}$$

During driving at constant velocity and at standstill the static axle loads on front G_F and rear G_R are given by

$$G_F = G \cdot \frac{L - L_F}{L}, \tag{A.3}$$

$$G_R = G \cdot \frac{L_F}{L}, \tag{A.4}$$

$$G = G_F + G_R. \tag{A.5}$$

For further derivation it is helpful to introduce dimensionless parameters. The static load distribution Ψ is calculated by

$$\Psi = \frac{G_R}{G} = \frac{L_F}{L}, \tag{A.6}$$

where G_R and G denote the static rear axle load and the total vehicle weight, L_G and L the distance from the front wheel to the force of gravity and the wheelbase. In addition, the ratio χ is defined as

$$\chi = \frac{H}{L}, \tag{A.7}$$

where H and denotes the gravity height. During braking the position of C_G leads to a dynamic axle loading distribution $\pm\Delta G$. The front axle gets additional load while the rear axle gets less load. Using the equilibrium of moments around the rear wheel contact point (quasi-static state), the current normal force of the front axle F_{NF} reads

$$F_{NF} = G \cdot \left(\frac{L - L_F}{L} + z \cdot \frac{H}{L} \right) = G_F + \Delta G. \tag{A.8}$$

Similarly, the normal force on the rear axle F_{NR} reads

$$F_{NR} = G \cdot \left(\frac{L_F}{L} - z \cdot \frac{H}{L} \right) = G_R + \Delta G. \tag{A.9}$$

Equation (A.8) and Equ. (A.9) can be simplified using Equ. (A.6) and Equ. (A.7) and now read

$$\frac{F_{NF}}{G} = 1 - \Psi + z \cdot \chi, \tag{A.10}$$

$$\frac{F_{NR}}{G} = \Psi - z \cdot \chi. \tag{A.11}$$

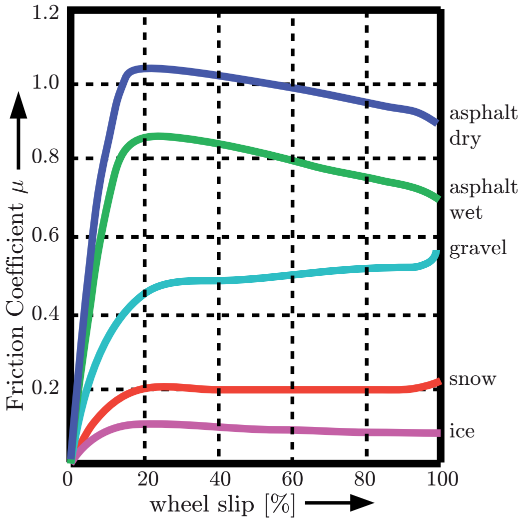

Figure A.2.: Course of friction coefficient μ between tyre and road for different road surfaces [172].

The normal F_N and longitudinal forces F_L of the tyre are coupled regarding *Coulomb's law* and are specified as

$$F_{LF} = \mu_F \cdot F_{NF}, \tag{A.12}$$

$$F_{LR} = \mu_R \cdot F_{NR}, \tag{A.13}$$

where μ_F and μ_R are the current friction coefficients at front and rear axle which depend on tyre and road. Figure A.2 presents courses of the friction coefficient for different road surfaces or conditions respectively. In consideration of Equ. (A.10) and Equ. (A.11), it holds:

$$\frac{F_{LF}}{G} = \mu_F \frac{F_{NF}}{G} = \mu_F(1 - \Psi + z \cdot \chi), \tag{A.14}$$

$$\frac{F_{LR}}{G} = \mu_R \frac{F_{NR}}{G} = \mu_R(\Psi - z \cdot \chi). \tag{A.15}$$

In the ideal case, the friction coefficient at front and rear axle are equal ($\mu = \mu_F = \mu_R$). Taking into account the previous simplifications made, hence neglecting the external forces, and assuming that the dimensionless deceleration z equals the friction coefficient μ, a parametric representation of the optimal ideal brake force distribution is defined as

$$\frac{F_{LF}}{G} = z \cdot (1 - \Psi + z \cdot \chi), \tag{A.16}$$

$$\frac{F_{LR}}{G} = z \cdot (\Psi - z \cdot \chi). \tag{A.17}$$

Eliminating z by combining these equations gives

$$\frac{F_{LR}}{G} = \sqrt{\frac{(1-\Psi)^2}{4 \cdot \chi^2} + \frac{1}{\chi} \cdot \frac{F_{LF}}{G}} - \frac{1-\Psi}{2 \cdot \chi} - \frac{F_{LF}}{G}. \tag{A.18}$$

This curve equals a parabola and is called the *parabola of the ideal brake force distribution*, see the red line in Fig. A.3 [27, 69, 102].

Installed Brake Force Distribution

After discussing the *external dynamic* during braking, the *internal dynamic* will now be presented. Thereby, only the brake system is investigated and influences of the powertrain are neglected, which are mainly the inertia of rotating parts and the rolling resistance of the tyre. The contact pressing force of the brake pads is the product of the hydraulic brake pressure p_{hyd} and the piston area A_B. The friction force F_F at the brake disc results according to *Coulomb's Law* by multiplying the friction coefficient between brake disc and pad μ_B with the contact pressing force. The result has to be multiplied by two because there are brake pads on either side of the disc. Thus F_F reads

$$F_F = A_B \cdot p_{\text{hyd}} \cdot \mu_B \cdot 2. \tag{A.19}$$

This force acts at the effective friction radius r_{eff} which results in a torque at the axle. To obtain the longitudinal force acting in the wheel contact point, this torque has to be divided by the dynamic roll radius of the tyre, r_{dyn}. Furthermore, there are two tyres per axle, so the result has to be multiplied by two. For better visibility, the brake coefficient B is introduced. The assumption is that the brake pressure is equal at front and rear axle and thus longitudinal forces are given by

$$F_{LF} = p_{\text{hyd}} \cdot \underbrace{\frac{2}{r_{\text{dyn}}} \cdot A_{BF} \cdot r_{\text{eff},F} \cdot 2 \cdot \mu_{BF}}_{B_F}, \tag{A.20}$$

$$F_{LR} = p_{\text{hyd}} \cdot \underbrace{\frac{2}{r_{\text{dyn}}} \cdot A_{BR} \cdot r_{\text{eff},R} \cdot 2 \cdot \mu_{BR}}_{B_R}. \tag{A.21}$$

Furthermore a brake force distribution coefficient f_B is defined as

$$f_B = \frac{F_{LR}}{F_{LF}} = \frac{p_{\text{hyd}} \cdot B_R}{p_{\text{hyd}} \cdot B_F} = \frac{B_R}{B_F}. \tag{A.22}$$

By defining a rear axle brake force proportion ϕ as

$$\phi = \frac{B_R}{B_R + B_F} = \frac{f_B}{1 + f_B}, \tag{A.23}$$

and combining Equ. (A.16) and Equ. (A.17), the brake force proportion reads

$$f_B = \frac{\phi}{1 - \phi} = \frac{z \cdot (\Psi - z \cdot \chi)}{z \cdot (1 - \Psi + z \cdot \chi)}. \tag{A.24}$$

Finally, the intersection of the installed and the ideal brake force distribution is given by

$$z_{\text{cri}} = \frac{\Psi - \phi}{\chi}, \tag{A.25}$$

where z_{cri} denotes the critical deceleration. As long as the friction coefficient between tyre and road is less than z_{cri}, the wheels at the front axle will lock first. Otherwise the rear axle will lock first and the vehicle will react in an unstable manner. Because of this, the critical deceleration is also described as *critical friction coefficient*. Figure A.3 shows the z_{cri} diagram.

The coordinate axes correspond to the longitudinal brake forces. The red line indicates the ideal brake force distribution (Equ. (A.16), Equ. (A.17) and Equ. (A.18)). To achieve this line, the distribution of the brake force (f_B an thus ϕ and z_{cri}) has to be changed depending on the deceleration z. However, vehicles usually have a fixed brake force distribution and therefore fixed values for f_B, ϕ and z_{cri}.

The black line is an example for a vehicle having a z_{cri} equal 0.9. If there is a tyre to road friction coefficient equal to 0.7, e.g. wet conditions, the black line first touches the orange $\mu_F = 0.7$ line (first magenta circle). Consequently, the front axle locks first, but there would still be potential at the rear axle which is unused. Due to this, a maximum deceleration of approximately $z = 0.6$ (blue dashed lines) can be reached with the fixed installed brake force distribution.

However, if the tyre to road friction coefficient equals 1.1 (very good and dry road conditions), the installed brake force distribution touches the green $\mu_R = 1.1$ line first, third magenta circle. In that case the rear axle would lock first and the car would react in an unstable manner.

Driving safety systems such as the *Anti-lock Brake System* (ABS) prevents wheels locking, so the driver retains control. In addition, modern ABS changes the brake pres-

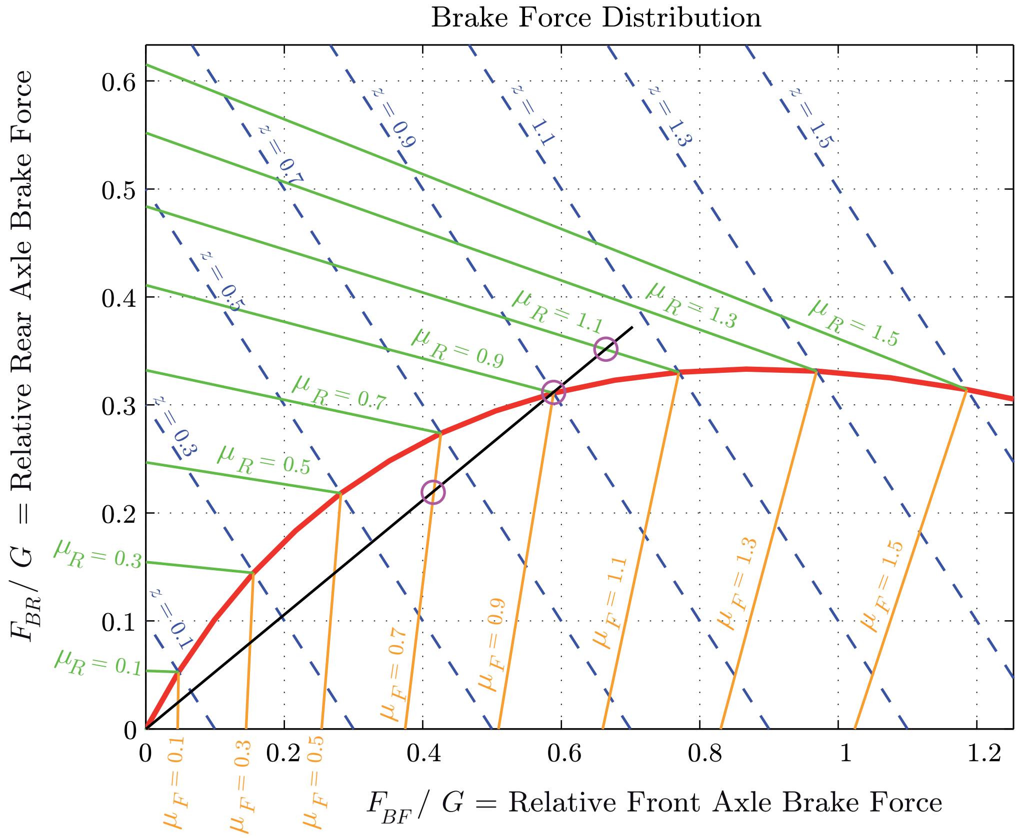

Figure A.3.: Ideal and installed brake force distribution, z_{cri} diagram.

sure for every wheel separately[1]. As a result in case of an emergency stop the vehicle can reach the maximum possible deceleration (the ideal brake force distribution line) independent from the installed distribution. Nevertheless, a proper installed distribution is important for a good driving sensation.

---

[1] Old ABS controlled the front wheels separately and the rear wheels together.

A.2. FEM

Element Order and Shape Functions

Figure A.4 shows the difference regarding the element order for the tetrahedral elements and Fig. A.5 for the hexahedral elements. The quadratic elements have additionally nodes at the middle of the edges. Therefore, the shape functions are quadratic instead of linear. Because of their basic element shape and numbers of nodes, the elements are called *Tetra4*, *Tetra10*, *Hexa8* and *Hexa20*.

The shape functions are necessary to continuously approximate the potential curve across the element. These functions have the characteristic to be one in their current node and zero in the other nodes. In addition, the shape functions have to be continuous functions. For a linear tetrahedral element, such as depicted in Fig. A.6 the following linear shape functions apply

$$\mathrm{N}_{L1} = 1-\xi-\eta-\zeta, \tag{A.26}$$
$$\mathrm{N}_{L2} = \zeta, \tag{A.27}$$
$$\mathrm{N}_{L3} = \eta, \tag{A.28}$$
$$\mathrm{N}_{L4} = \xi, \tag{A.29}$$

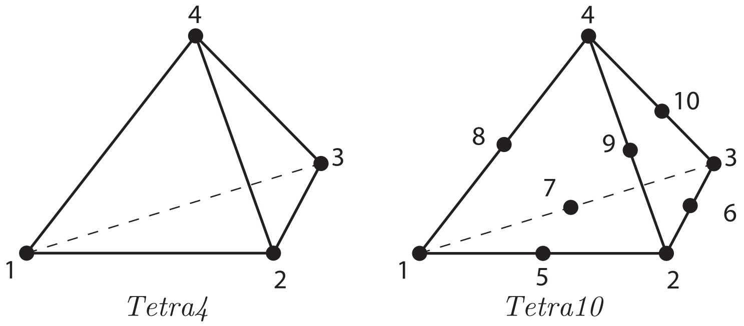

Figure A.4.: Difference *Tetra4* and *Tetra10* elements.

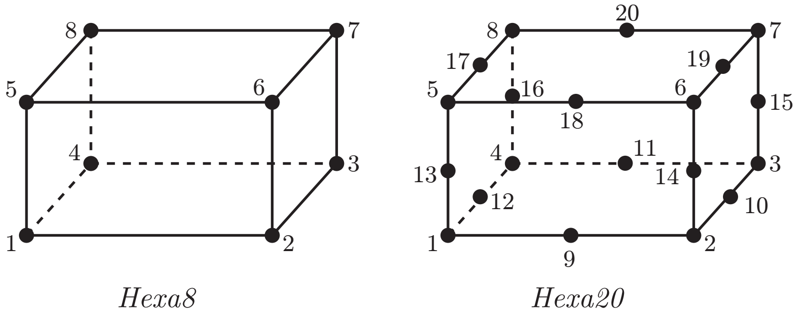

Figure A.5.: Difference *Hexa8* and *Hexa20* elements.

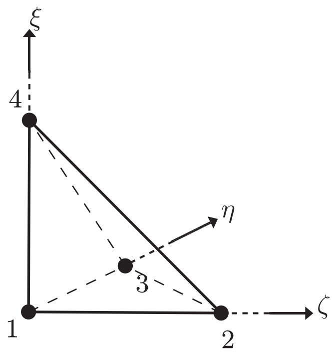

Figure A.6.: Basis function *Tetra4* element.

where ξ, η and ζ are the coordinate axles of the element. For the quadratic element in addition to the four quadratic shape functions N_{Qi} of the four corner nodes, six quadratic shape functions for the middle nodes are necessary. The shape functions read

$$\mathrm{N}_{Q1} = \mathrm{N}_{L1}(2\mathrm{N}_{L1} - 1), \tag{A.30}$$
$$\mathrm{N}_{Q2} = \mathrm{N}_{L2}(2\mathrm{N}_{L2} - 1), \tag{A.31}$$
$$\mathrm{N}_{Q3} = \mathrm{N}_{L3}(2\mathrm{N}_{L3} - 1), \tag{A.32}$$
$$\mathrm{N}_{Q4} = \mathrm{N}_{L4}(2\mathrm{N}_{L4} - 1), \tag{A.33}$$
$$\mathrm{N}_{Q5} = 4\mathrm{N}_{L1}\mathrm{N}_{L2}, \tag{A.34}$$
$$\mathrm{N}_{Q6} = 4\mathrm{N}_{L2}\mathrm{N}_{L3}, \tag{A.35}$$
$$\mathrm{N}_{Q7} = 4\mathrm{N}_{L1}\mathrm{N}_{L3}, \tag{A.36}$$
$$\mathrm{N}_{Q8} = 4\mathrm{N}_{L1}\mathrm{N}_{L4}, \tag{A.37}$$
$$\mathrm{N}_{Q9} = 4\mathrm{N}_{L2}\mathrm{N}_{L4}, \tag{A.38}$$
$$\mathrm{N}_{Q10} = 4\mathrm{N}_{L3}\mathrm{N}_{L4}, \tag{A.39}$$

and include now quadratic terms of ξ, η and ζ [20].

Results

Table A.1.: Complex frequencies calculated with *Abaqus*, reduced integration, instable frequencies (double frequencies) marked yellow, frequencies on the verge of being unstable marked green, friction coefficient equals 0.7.

160bar				8bar			
Tetra4	**Tetra10**	**Hexa8**	**Hexa20**	**Tetra4**	**Tetra10**	**Hexa8**	**Hexa20**
835	690	678	657	835	690	678	657
946	741	721	702	945	741	721	702
982	855	837	840	982	855	837	840
1142	993	933	940	1141	992	932	939
1179	1057	979	992	1179	1057	978	992
1258	1131	1079	1077	1257	1131	1079	1077
1430	1143	1143	1143	1429	1141	1141	1141
1890	1745	1726	1746	1890	1745	1725	1746
2109	1804	1729	1752	2108	1803	1729	1751
2158	1804	1767	1775	2158	1804	1767	1775
2242	1894	1801	1801	2242	1894	1800	1801
2270	1930	1822	1842	2269	1930	1822	1842
2270	2229	2102	2138	2269	2229	2102	2138
2354	2241	2109	2141	2352	2241	2108	2140
2657	2247	2246	2246	2656	2246	2245	2245
2679	2358	2352	2351	2679	2356	2349	2349
3232	2747	2598	2666	3232	2747	2598	2666
3417	2789	2707	2725	3415	2788	2707	2724
3446	2877	2793	2785	3446	2877	2791	2785
3832	3360	3233	3200	3832	3368	3232	3198
3832	3499	3341	3291	3832	3499	3341	3290
3882	3589	3427	3516	3882	3591	3428	3517
3929	3827	3692	3780	3929	3829	3692	3780
4022	3841	3817	3823	4022	3840	3817	3824
4085	3893	3817	3837	4088	3893	3817	3837
4296	3930	3856	3866	4296	3937	3863	3876
4374	3955	3907	3925	4374	3957	3907	3925
4422	3999	3929	3955	4422	3999	3931	3956
4573	4082	4012	4040	4576	4083	4018	4045
4623	4180	4073	4106	4623	4181	4077	4109
4745	4242	4096	4106	4745	4247	4097	4109
4965	4732	4480	4557	4965	4732	4480	4557
5084	4799	4626	4690	5086	4800	4627	4693
5402	4946	4676	4716	5401	4948	4679	4717
5720	5027	4700	4718	5719	5028	4700	4718
5753	5105	4751	4891	5752	5105	4752	4892
5806	5182	5073	5077	5807	5183	5074	5080
5935	5403	5400	5402	5935	5402	5399	5401
6002	5729	5525	5689	6002	5730	5525	5689
6275	5877	5576	5689	6286	5878	5577	5689
6340	5922	5743	5748	6340	5922	5742	5747
6340	6131	5743	5882	6340	6132	5742	5882
6600	6134	5850	5938	6602	6132	5850	5938
6827	6271	6066	6072	6826	6282	6066	6073
6828	6317	6070	6077	6829	6317	6070	6077
7013	6371	6226	6256	7008	6373	6227	6257
7036	6463	6237	6273	7042	6462	6240	6280
7171	6642	6330	6342	7172	6641	6337	6343
7264	6663	6357	6342	7263	6664	6355	6343
7264	6777	6462	6417	7263	6777	6462	6417

Table A.2.: Complex frequencies calculated with *Abaqus*, full integration, instable frequencies (double frequencies) marked yellow, frequencies on the verge of being unstable marked green, friction coefficient equals 0.7.

160bar				8bar			
Tetra4	**Tetra10**	**Hexa8**	**Hexa20**	**Tetra4**	**Tetra10**	**Hexa8**	**Hexa20**
845	696	712	670	845	696	711	669
961	745	758	713	960	745	758	713
985	867	860	851	985	866	860	850
1151	1006	976	947	1150	1005	975	956
1190	1075	1039	1015	1189	1075	1039	1015
1276	1133	1135	1087	1275	1133	1135	1087
1435	1153	1153	1152	1435	1151	1151	1151
1890	1745	1790	1753	1890	1745	1790	1754
2128	1805	1809	1774	2126	1805	1808	1773
2161	1822	1835	1786	2161	1821	1835	1786
2251	1902	1854	1813	2251	1902	1854	1813
2282	1971	1926	1888	2281	1970	1925	1887
2308	2242	2179	2149	2307	2241	2179	2149
2379	2247	2187	2158	2376	2247	2187	2158
2668	2256	2254	2254	2667	2255	2253	2253
2686	2381	2379	2376	2686	2378	2377	2374
3298	2798	2787	2724	3298	2797	2786	2723
3468	2826	2881	2778	3468	2825	2881	2777
3498	2894	2902	2811	3496	2894	2900	2812
3908	3443	3393	3295	3905	3441	3391	3293
3952	3503	3450	3317	3952	3503	3450	3317
4260	3673	3687	3599	4260	3672	3688	3600
4299	3907	3911	3857	4299	3905	3909	3857
4354	3937	3941	3909	4355	3936	3940	3909
4383	3986	3977	3920	4383	3987	3977	3922
4460	4012	4008	3978	4461	4012	4008	3978
4582	4285	4189	4130	4581	4289	4191	4132
4589	4412	4379	4356	4590	4413	4380	4357
4737	4521	4482	4431	4736	4521	4482	4432
4849	4539	4563	4546	4849	4538	4563	4547
4883	4631	4604	4579	4883	4632	4618	4580
4968	4733	4721	4615	4968	4733	4723	4615
5335	4883	4761	4720	5335	4882	4761	4720
5527	5062	4941	4847	5527	5062	4946	4853
5831	5146	4949	4872	5831	5146	4949	4875
5900	5181	5134	5014	5900	5181	5135	5014
5957	5383	5338	5323	5957	5382	5338	5323
6124	5531	5517	5511	6124	5530	5517	5512
6319	5898	5913	5755	6317	5899	5914	5758
6340	6075	5963	5858	6340	6074	5963	5860
6349	6133	6147	6028	6348	6133	6148	6027
6689	6133	6153	6039	6699	6133	6153	6040
6788	6304	6170	6089	6785	6302	6170	6089
6836	6347	6183	6090	6836	6348	6183	6089
6866	6365	6310	6314	6863	6365	6308	6314
7267	6581	6373	6314	7268	6581	6373	6314
7267	6618	6396	6348	7268	6621	6396	6349
7429	6698	6640	6424	7423	6702	6640	6424
7491	6698	6690	6494	7485	6702	6700	6494
7659	6776	6797	6514	7653	6776	6797	6514

Table A.3.: Complex frequencies calculated with *MD Nastran*, reduced integration, instable frequencies (double frequencies) marked yellow, frequencies on the verge of being unstable marked green, friction coefficient equals 0.7.

160bar			**8bar**		
Tetra4	**Tetra10**	**Hexa8**	**Tetra4**	**Tetra10**	**Hexa8**
910	5	765	547	5	689
1049	7	786	83	7	763
1120	761	892	928	761	843
1387	761	1025	1066	761	885
1592	797	1025	1127	797	999
1597	1009	1196	1384	1009	1085
1960	1009	1298	1924	1009	1242
2128	1138	1810	2199	1138	1331
2140	1190	1841	2205	1190	1808
2214	1724	1868	2226	1724	1829
2267	1741	1868	2265	1741	1857
2271	1825	1904	2270	1825	1858
2404	1829	2209	2379	1829	1923
2643	1829	2209	2591	1829	2160
2644	1922	2250	2629	1922	2177
2838	1922	2371	2778	1922	2216
3745	2129	2764	3729	2129	2261
3749	2241	2856	3732	2241	2300
3771	2241	2872	3844	2241	2812
3820	2244	3327	3844	2244	2871
4023	2770	3457	4209	2770	2883
4240	2865	3635	4286	2865	2948
4302	2910	3847	4377	2910	3346
4382	2910	3922	4377	2910	3455
4415	2939	3959	4462	2939	3482
4462	3471	4016	4508	3471	3586
4545	3598	4086	4580	3598	3898
4703	3599	4183	4717	3599	3911
4959	3600	4266	4963	3600	3950
5030	3746	4379	5155	3746	4002
5036	3810	4494	5159	3810	4020
5139	3937	4695	5202	3937	4040
5413	3944	4774	5452	3944	4380
5582	3947	4804	5627	3947	4583
5582	4015	4868	5836	4015	4693
5896	4015	5071	6309	4015	4782
6320	4735	5178	6310	4735	4807
6346	4773	5402	6407	4773	4994
6474	5006	5554	6618	5006	5007
6474	5006	5729	6618	5006	5284
6622	5137	5873	6834	5137	5492
6800	5137	6058	6835	5137	5603
6800	5243	6112	6836	5243	5737
6847	5421	6155	7104	5421	5981
7038	5495	6156	7106	5495	6001
7231	5768	6165	7393	5768	6083
7232	5939	6378	7472	5939	6122
7284	6091	6396	7588	6091	6130
7438	6091	6577	7706	6091	6169
7707	6096	6761	7709	6096	6173

Table A.4.: Overview of the instable frequencies in Hz, measured brake pressure during squeal event on the test rig ranged between 9 bar and 16 bar, measured friction coefficient during squeal event on test rig ranged between 0.3 and 0.5, final brake pressures in the simulations are 8 bar and 160 bar, frequencies on the verge of being unstable are written in italics, friction coefficient for all simulation equals 0.7.

Test Rig	Nastran					ABAQUS							
	tetrahedral			hexahedral		tetrahedral		hexahedral		tetrahedral		hexahedral	
	linear		quadratic	linear		linear	quadratic	linear	quadratic	linear	quadratic	linear	quadratic
	reduced		reduced	reduced		reduced		reduced		full		full	
9-16	8	160	8 & 160	8	160	8 & 160	8 & 160	8 & 160	8 & 160	8 & 160	8 & 160	8 & 160	8 & 160
			761										
		1597	1009		1025								
1890			1829	*1857*	1868		1804	*1727*	*1748*				
2000			1922										
	2200	*2271*	2241		2209	2269	*2243*	*2105*	*2138*		*2243*	*2183*	*2153*
	2268												
		2644	2910										
	3732	*3749*	*3598*			3832		3817					
	3844		*3945*										
	4377		4015						4107				
									4717	*4585*		*4947*	
	5157	*5036*	5006										
		5582	5137					5743	5689				
			6091	*6125*	*6155*		*6132*	*6067*	*6074*		6133	*6150*	6089
	6310	6474		*6170*		6340			6343	*6344*			6314
	6618	6800									6698		
	6836					***6827***	6776						
	7106	*7232*				7264				7267			
	7709												
13400													

A.3. Friction Force Measuring Pin

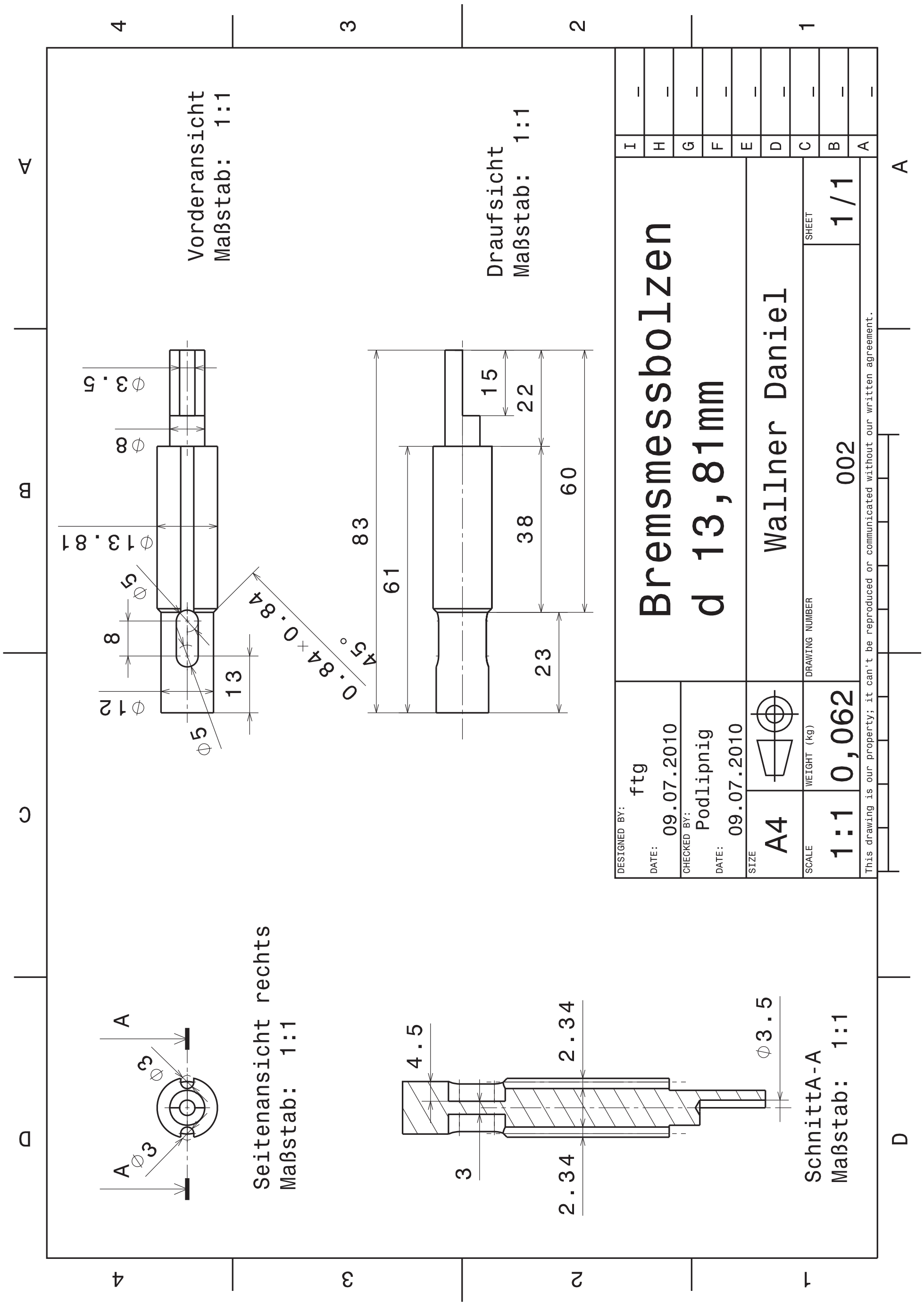

Figure A.7.: Technical drawing friction force measuring pin.

A.4. Sensibility Analysis

Nomenclature Measurements

Every brake application measurement has a unique code with 26 characters. For an easier understanding one exemplary code is separated into 15 Blocks:

Example:	23 _	O_	S	C	c	s	d	_v	5>50	_p	15	_c	c	_w	n
Block #:	1	2	3	4	5	6	7	8	9	10	11	12	13	14	15

Block 1: The parameter set number. Brake applications with the same number have equal parameter sets.
Block 2: Used brake pad material: ”S” *Sinter B* or ”O” *Organic B*.
Block 3: Attached spring ”S”, or not ”_”.
Block 4: Attached claw shims ”C”, or not ”_”.
Block 5: Chamfers on pad ”c”, or not ”_”.
Block 6: Slot in the friction material ”s”, or not ”_”.
Block 7: Attached damping shims d”, or not ”_”.
Block 8: Constant prefix for indicating the following velocity.
Block 9: The constant velocities ”20” and ”25”, or the deceleration ”50>5” and acceleration ”5>50”, given in kph.
Block 10: Constant prefix for indicating the following brake pressure.
Block 11: Applied constant brake pressure ”10”, ”15”, ”20”, ”25” and ”30” bar.
Block 12: Constant prefix for indicating the following climate chamber setting.
Block 13: Current climate chamber setting: warm ”w”, normal ”n” and cold ”c”.
Block 14: Constant prefix for indicating if and where water is sprayed.
Block 15: Water sprayed on the disc at the outer side ”o”, inner side ”i” or not ”n”.

Nomenclature Sensors

The nomenclature of the sensors is explained in order of their appearance on the axis of abscissas in the results plots. The prefix ”P2P” indicates, that the *Peak-to-Peak* values during brake application are evaluated. The suffix ”rel” indicates that the relative value is evaluated. Hence, the difference between the value before brake application to the value during the brake application. Otherwise the absolute obtained values during the brake application are evaluated. The *Triaxial Acceleration Sensors* (TAS) are explained explicitly:

Label	Measured Value
"Speed"	Rotational speed.
"Pressure"	Applied brake pressure.
"Climate"	Environmental conditions (three possibilities: hot, normal or cold).
"Water"	Defines if water is sprayed (three possibilities: not, inner side, outer side).
"Squeal Ratio"	The calculated ratio of squealing time to braking time.
"Friction Coefficient"	Calculated regarding SAE J2521, Equ. (4.1).
"Mic"	Microphone.
"Pin"	Friction force measuring pin ("OS" outer side, "IS" inner side)
"shear"	Pad shear strain ("OS" outer side, "IS" inner side)
"Torque"	Brake torque
"EC"	Eddy current sensor ("LE" leading edge, "M" middle, "TE" trailing edge)

The TASs are named regarding their position. The suffix indicates the measurement direction, which is for all sensors fixed equally. The axial direction "AXI" equals the axis of rotation of the disc. The radial direction "RAD" goes from the axis of rotation/centre of the disc through the sensor and the tangential direction "TAN" has to be perpendicular to the other two directions.

Part	Acronym	Location
Disc	"OR"	Outer Radius
	"IR"	Inner Radius
	"OFF"	Offset (adjacent cooling duct)
Pad	"OS TE"	Outer Side Trailing Edge
	"OS LE"	Outer Side Leading Edge
Caliper	"Cal"	Next brake line connection
	"OS Cal"	Outer side between the ECSs

For all sensor signals the maximum and the average values are evaluated and visualised in results plots. As a consequence of the partial significantly different measured values from the various sensors, each sensor results vector $\mathbf{S}$ is scaled regarding its maximum value:

$$\mathbf{S}_s = \frac{\mathbf{S}}{\max(\mathbf{S})}. \tag{A.40}$$

The used maximum value of every scaled sensor results vector $\mathbf{S}_\mathbf{S}$ is written at the end of the sensor nomenclature in every results figure. As a consequence, the plotted values are between $[0, 1]$.

Results

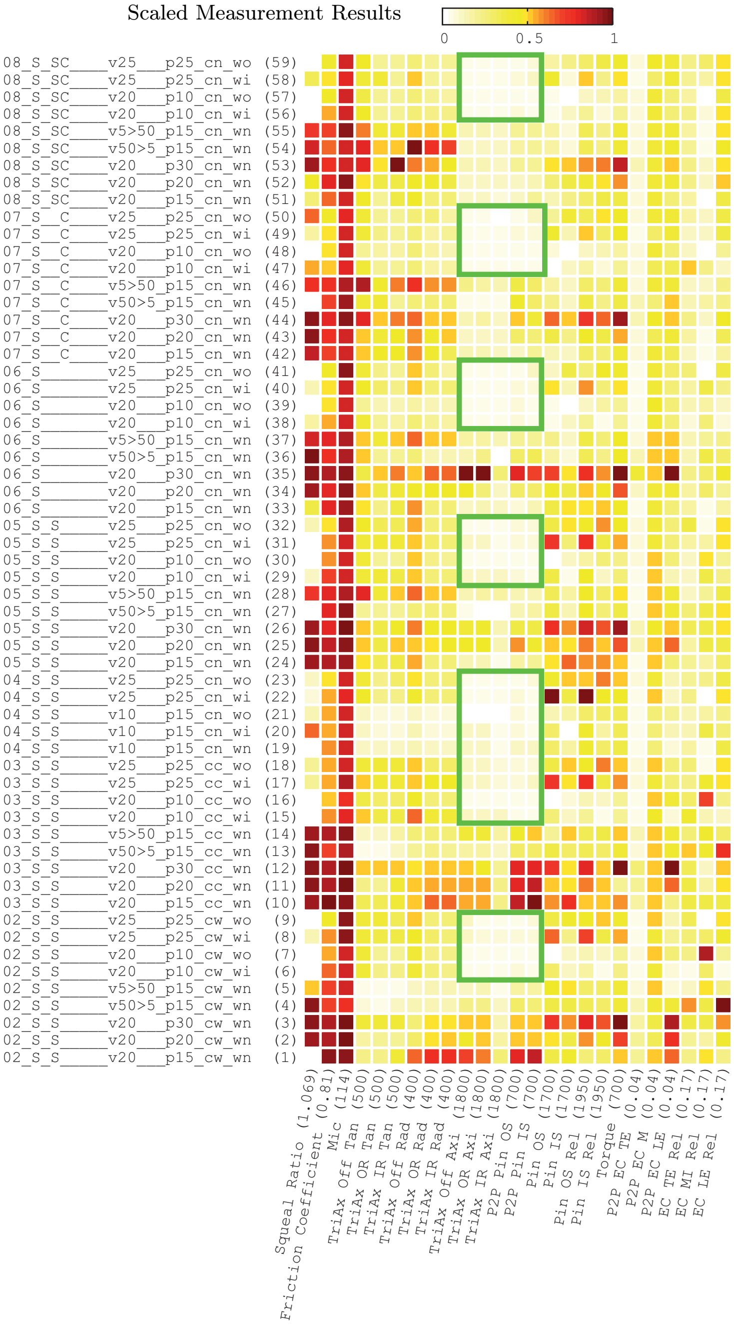

Figure A.8.: Measured average signals using the *Sinter B* brake pads, part 1.

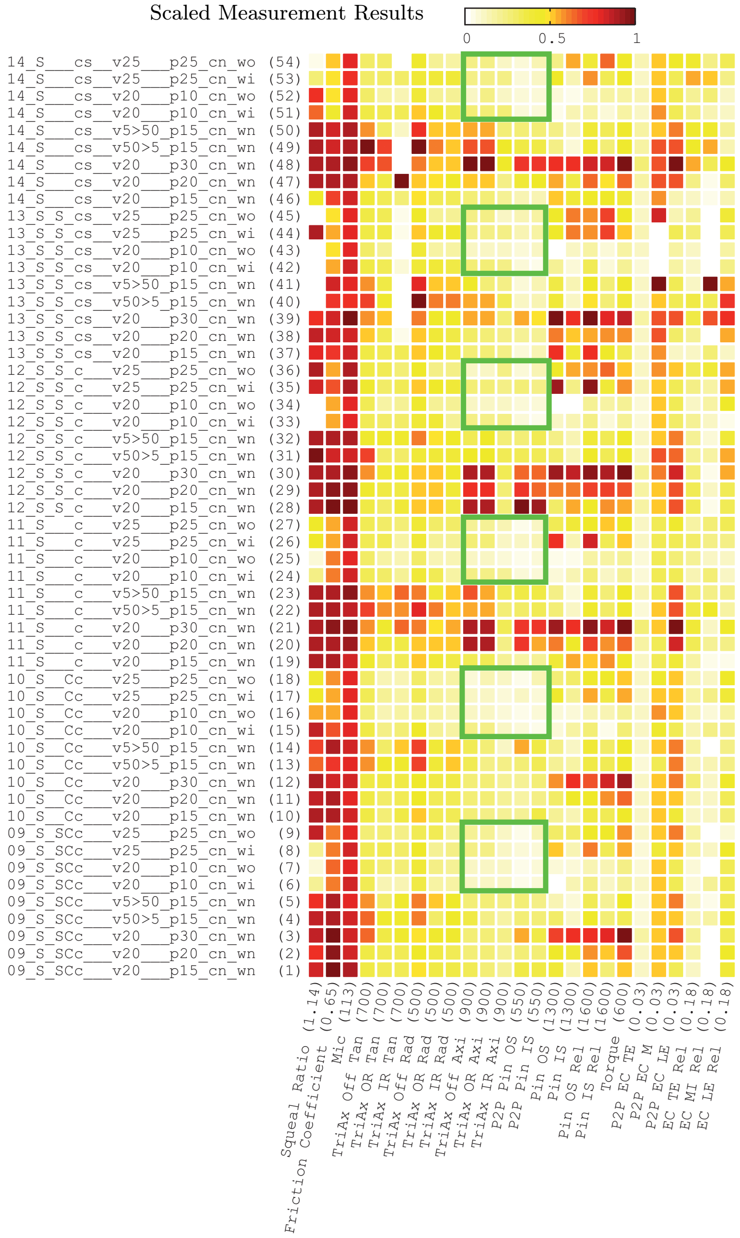

Figure A.9.: Measured average signals using the *Sinter B* brake pads, part 2.

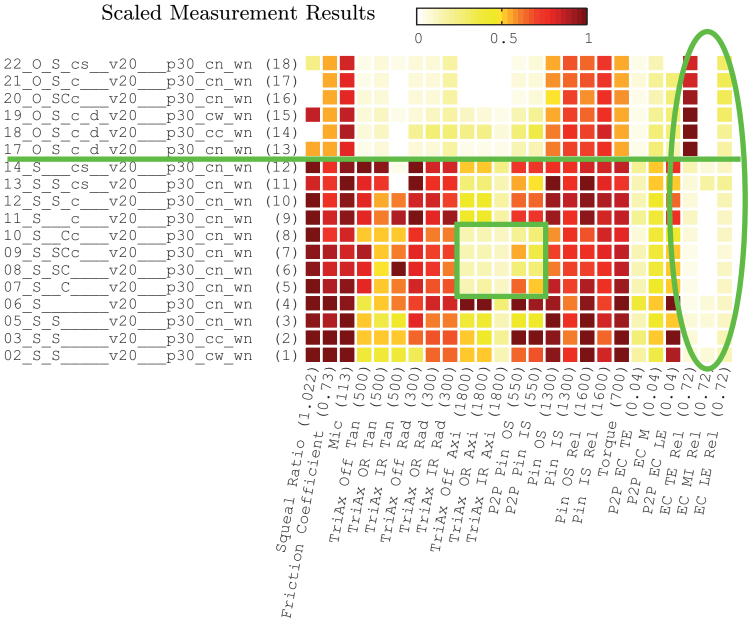

Figure A.10.: Measured average signals of measurements with brake pressure 30 bar.

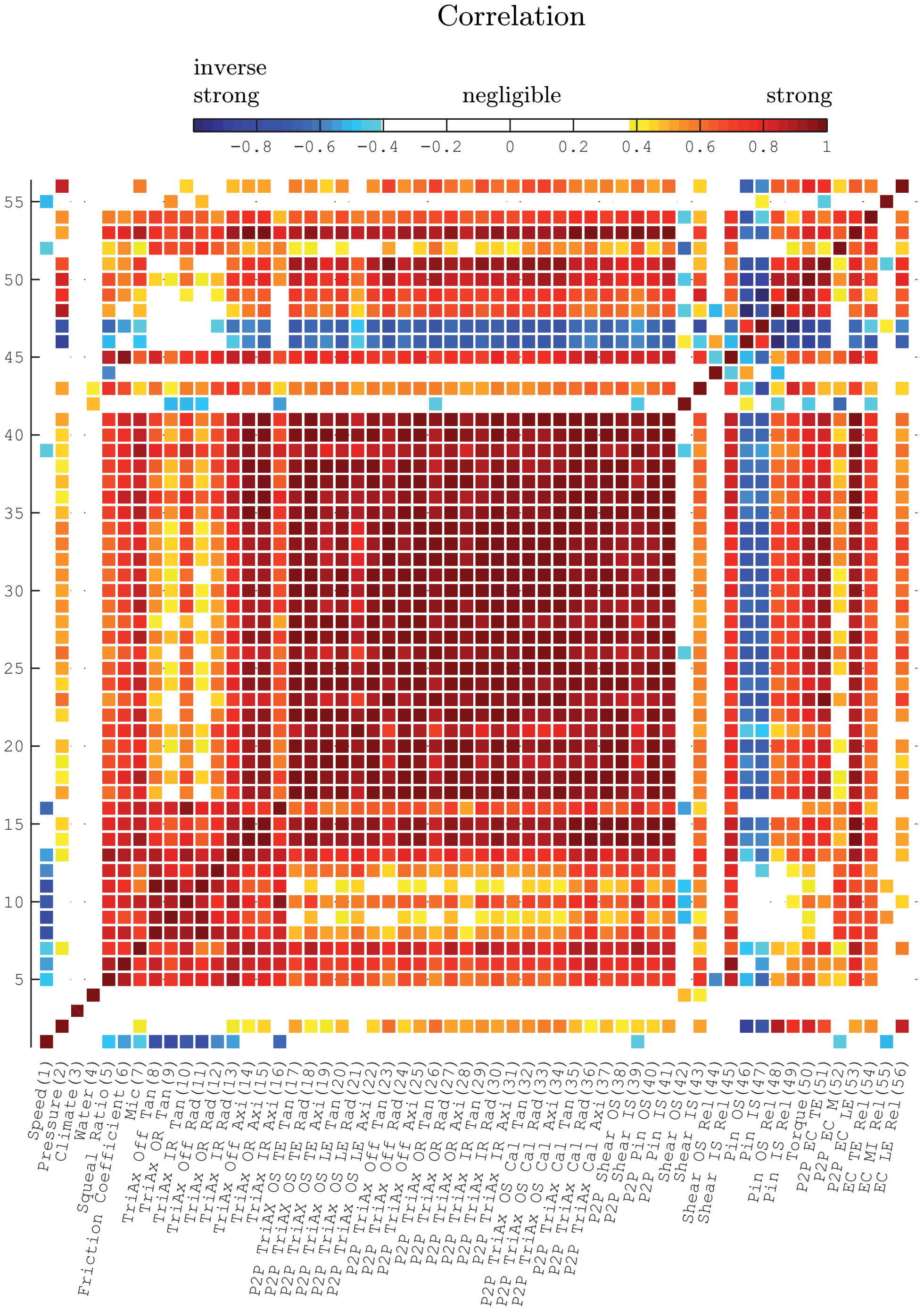

Figure A.11.: Correlation coefficients of average signals, only measurements including *Sinter B* brake pads with chamfers are taken into account.

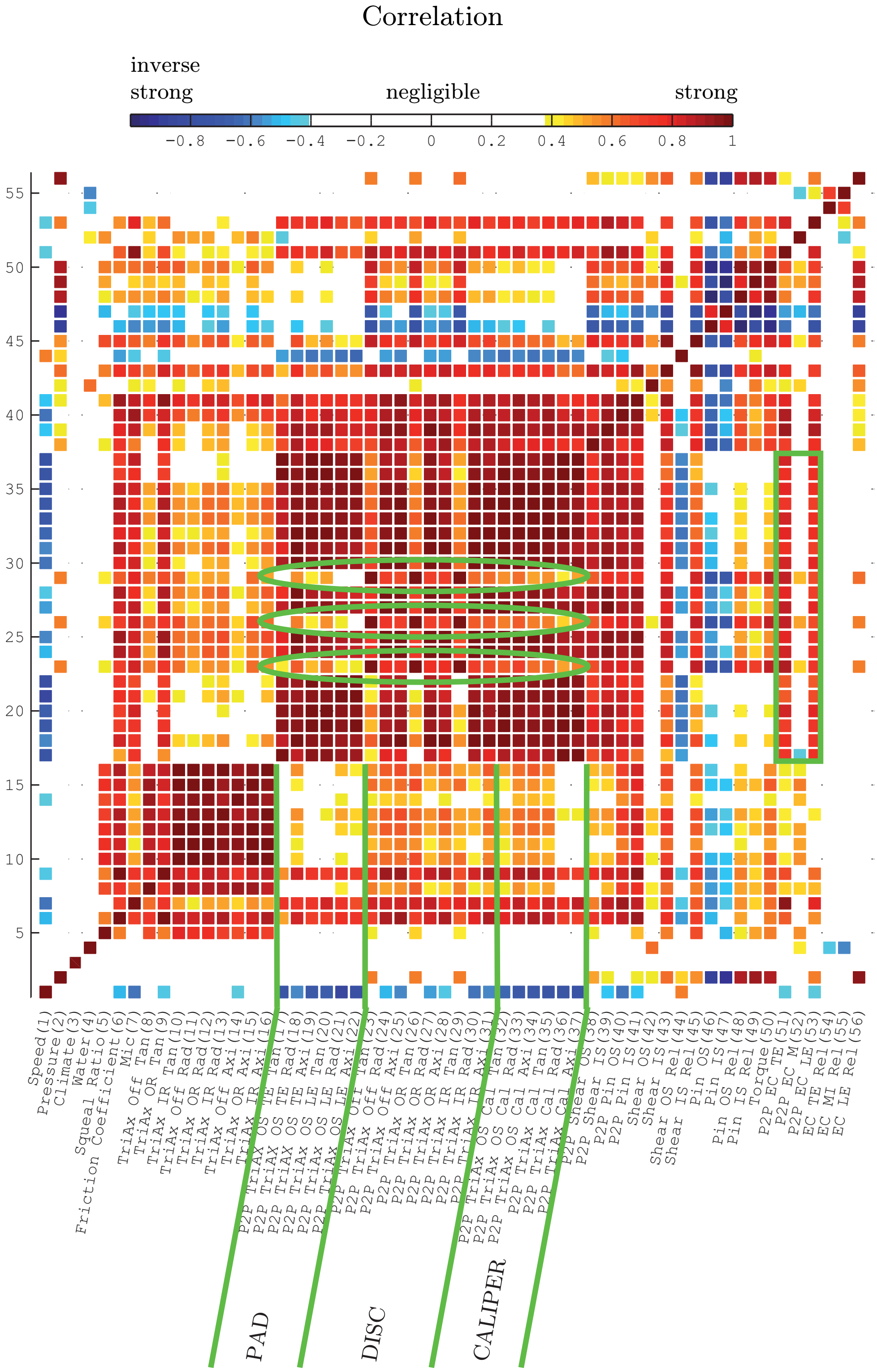

Figure A.12.: Correlation coefficients of average signals, only measurements including *Sinter B* brake pads and claw shims are taken into account.

Bibliography

[1] Abaqus. *http://www.3ds.com/products/simulia/overview/*, Accessed on 22/06 2012.

[2] M. K. Abdelhamid. Filling the Gaps in Brake NVH Development. *SAE Technical Paper*, 2010-01-1684, 2010.

[3] H. Abendroth, M. Haverkamp, W. Hoffrichter, P. Blaschke, G. Mauer, and B. Wernitz. Current and New Approaches for Brake Noise Evaluation and Rating. *SAE International Journal of Passenger Cars- Mechanical Systems*, 2(2):23–45, 2010.

[4] H. Abendroth and B. Wernitz. The Integrated Test Concept: Dyno - Vehicle, Performance - Noise. *SAE Technical Paper*, 2000-01-2774, 2000.

[5] A. R. AbuBakar, M. K. AbdulHamid, M. Mohamad, A. Dzakaria, and B. AbdGhani. Numerical analysis of disc brake squeal considering temperature dependent friction coefficient. In *Conference on Natural Resources Engineering and Technology*, Putrajaya, Malaysia, 2006.

[6] A. R. AbuBakar, M. K. AbdulHamid, M. Mohamad, A. Dzakaria, and B. AbdGhani. Stability analysis of disc brake squeal considering temperature effect. *Jurnal Mekanikal*, 22:26–38, 2006.

[7] A. R. AbuBakar, L. Li, S. James, H. Ouyang, and J. E. Siegel. Wear simulation and its effect on contact pressure distribution and squeal of a disc brake. In *International Conference on Vehicle Braking Technology*, St. William's College, York, UK, 2006.

[8] A. R. AbuBakar and H. Ouyang. Complex eigenvalue analysis and dynamic transient analysis in predicting disc brake squeal. *International Journal Vehicle Noise and Vibration*, 2:143–155, 2006.

[9] A. R. AbuBakar and H. Ouyang. Wear prediction of friction material and brake squeal using the finite element method. *Wear*, 264(11-12):1069–1076, 2008.

[10] A. R. AbuBakar, H. Ouyang, S. James, and L. Li. Finite element analysis of wear and its effect on squeal generation. *Proceedings of the Institution of Mechanical Engineers, Part D: Journal of Automobile Engineering*, 222(7):1153–1165, 2008.

[11] A. R. AbuBakar, A. Sharif, M. Z. A. Rashid, and H.Ouyang. Brake Squeal: Complex Eigenvalue versus Dynamic Transient Analysis. *SAE Technical Paper*, 2007-01-3964, 2007.

[12] A. Akay. Acoustics of friction. *Journal of the Acoustical Society of America*, 111(4):1525–1548, 2002.

[13] A. Akay, O. Giannini, F. Massi, and A. Sestieri. Disc brake squeal characterization through simplified test rigs. *Mechanical Systems and Signal Processing*, 23(8):2590–2607, 2009.

[14] R. Allgaier. *Experimentelle und numerische Untersuchungen zum Bremsenquietschen*. PhD thesis, University of Stuttgart, 2001.

[15] R. Allgaier, L. Gaul, W. Keiper, K. Willner, and N. P. Hoffman. A Study on Brake Squeal using a Beam-On-Disc Model. In *International Modal Analysis Conference - IMAC-XX*, Los Angeles, California, USA, 2002.

[16] D. B. Antanaitis. Effect of Regenerative Braking on Foundation Brake Performance. *SAE Technical Paper*, 2010-01-1681, 2010.

[17] J. Awrejcewicz and P. Olejnik. Analysis of Dynamic Systems With Various Friction Laws. *Applied Mechanics Reviews*, 58(6):389–411, 2005.

[18] W. J. Bagaria and W. M. Sharpe. Temperature and Rise-Time Effects on Dynamic Strain Measurements. In *SESA Spring Meeting*, Detroit, MI, USA, 1974.

[19] A. M. Balvedi and S. N. Y. Gerges. Squeal noise in disc brakes and the influence of damping on the system dynamic stability. *Acta Acustica united with Acustica*, 94(2):254–264, 2008.

[20] K.-J. Bathe. *Finite Element Procedures*, chapter 5 Formulation and Calculation of Isoparametric Finite Element Matrices, pages 338–484. Prentice-Hall, 1996.

[21] T. Belytschko, J. S.-J. Ong, W. K. Liu, and J. M. Kennedy. Hourglass control in linear and nonlinear problems. *Computer Methods in Applied Mechanics and Engineering*, 43(3):251 – 276, 1984.

[22] K. Bendel, M. Fischer, and M. Schüssler. Vibrational Analysis of Power Tools Using a Three Dimensional Scanning Vibrometer. In *Sixth International Conference on Vibration Measurements by Laser Techniques: Advances and Applications*, Ancona, Italy, 2004.

[23] A. Bender, K. Haesler, C. Thomas, and J. Grochowicz. Development of Universal Brake Test Data Exchange Format and Evaluation Standard. *SAE Technical Paper*, 2010-01-1698, 2010.

[24] F. Bergman, M. Eriksson, and S. Jacobson. The effect of reduced contact area on the occurrence of disc brake squeals for an automotive brake pad. *Proceedings of the Institution of Mechanical Engineers, Part D: Journal of Automobile Engineering*, 214(5):561–568, 2000.

[25] B. Breuer and K. H. Bill, editors. *Bremsenhandbuch*, chapter 22 Schwingungen und Geräusche, pages 327–333. Vieweg, 2006.

[26] A. Buck. *Simulation von Bremsenquietschen (Brake Squeal).* PhD thesis, Technische Universität München, 2008.

[27] M. Burckhardt. *Fahrwerktechnik: Bremsdynamik und PKW Bremsanlagen*, chapter 3 Bremsdynamik, pages 73–128. Vogel Verlag, 1991.

[28] T. Butlin and J. Woodhouse. Studies of the Sensitivity of Brake Squeal. In *6th Internaional Conference on Modern Practice in Stress and Vibration Analysis*, University of Bath, UK, 2006.

[29] T. Butlin and J. Woodhouse. Friction-induced vibration: Quantifying sensitivity and uncertainty. *Journal of Sound and Vibration*, 329:509–526, 2010.

[30] T. Butlin and J. Woodhouse. A systematic experimental study of squeal initiation. *Journal of Sound and Vibration*, 330(21):5077–5095, 2011.

[31] C. Cantoni, R. Cesarini, G. Mastinub, G. Rocca, and R. Sicigliano. Brake comfort - a review. *Vehicle System Dynamics*, 47(8):901–947, 2009.

[32] Q. Cao, H. Ouyang, M. I. Friswell, and J. E. Mottershead. Linear eigenvalue analysis of the disc-brake squeal problem. *International Journal for Numerical Methods in Engineering*, 61(9):1546–1563, 2004.

[33] D. Chan and G. W. Stachowiak. Review of automotive brake friction materials. *Proceedings of the Institution of Mechanical Engineers, Part D: Journal of Automobile Engineering*, 218(9):953–966, 2004.

[34] F. Chen. Automotive disk brake squeal: an overview. *International Journal of Vehicle Design*, 51(1/2):39–72, 2009.

[35] G. Chevallier, F. Renaud, S. Thouviot, and J.-L. Dion. Complex Eigenvalue Analysis for Structures with Viscoelastic Behavior. In *Proceedings of the ASME 2011 IDETC/CIE*, Washington, DC, USA, 2011.

[36] N. Coudeyras, S. Nacivet, and J.-J. Sinou. Periodic and quasi-periodic solutions for multi-instabilities involved in brake squeal. *Journal of Sound and Vibration*, 328(4-5):520–540, Dec. 2009.

[37] N. Coudeyras, J.-J. Sinou, and S. Nacivet. A new treatment for predicting the self-excited vibrations of nonlinear systems with frictional interfaces: The Constrained Harmonic Balance Method, with application to disc brake squeal. *Journal of Sound and Vibration*, 319(3-5):1175–1199, Jan. 2009.

[38] C. A. Coulomb. Die Theorie einfacher Schwingungen. *Memoires de mathematique et de physique de l'Académie des Sciences*, 10:161–331, 1785.

[39] Y. Dai and T. C. Lim. Suppression of brake squeal noise applying finite element brake and pad model enhanced by spectral-based assurance criteria. *Journal of Applied Acoustics*, 69(3):196–214, 2008.

[40] T. Degenstein. *Kraftmessung in Scheibenbremsen.* PhD thesis, Technische Universität Darmstadt, 2007.

[41] T. Degenstein, A. Dohle, A. Elvenkemper, and J. Lange. The μ - value - Friction Determination in Brake Systems. In *XXVI International μ Symposium*, Bad Neuenahr, Deutschland, 2006.

[42] T. Degenstein and H. Winner. Dynamic Measurement of the Forces in the Friction Area of a Disc Brake during a Braking Process. In *FISITA 2006, World Automotive Congress*, Yokohama, Japan, 2006.

[43] T. Degenstein and H. Winner. New methods of force and temperature measurement in a wheel brake during the braking process. In *XXVII International μ Symposium*, Bad Neuenahr, Deutschland, 2007.

[44] E. Denys and J. K. Thompson. The Development of a Brake Insulator Damping Measurement Procedure. *SAE Technical Paper*, 2010-01-1685, 2010.

[45] A. Dohle and C.-P. Fritzen. Investigation of model based friction coefficient measurements part I. In *International Conference on Vehicle Braking Technology*, St. William's College, York, UK, 2009.

[46] K. B. Dunlap, M. A. Riehle, and R. E. Longhouse. An Investigative Overview of Automotive Disc Brake Noise. *SAE Technical Paper*, 1999-01-0142, 1999.

[47] S. W. E. Earles and P. W. Chambers. Disc brake squeal - some factors which influence its occurrence. *Proceedings of the Institution of Mechanical Engineers, Part C: Journal of Mechanical Engineering Science*, 454:39–46, 1988.

[48] M. N. A. Emira. Friction-induced oscillations of a slider: Parametric study of some system parameters. *Journal of Sound and Vibration*, 300(3-5):916–931, 2007.

[49] M. Eriksson. *Friction and Contact Phenomena of Disc Brakes Related to Squeal.* PhD thesis, Uppsala University, 2000.

[50] M. Eriksson and S. Jacobson. Friction behaviour and squeal generation of disc brakes at low speeds. *Proceedings of the Institution of Mechanical Engineers, Part D: Journal of Automobile Engineering*, 215(12):1245–1256, 2001.

[51] M. Eriksson, A. Lundqvist, and S. Jacobson. A study of the influence of humidity on the friction and squeal generation of automotive brake pads. *Proceedings of the Institution of Mechanical Engineers, Part D: Journal of Automobile Engineering*, 215(3):329–342, 2001.

[52] H. Fastl and E. Zwicker. *Psychoacoustics: Facts and Models*, chapter 8 Loudness, pages 203–238. Springer, 2007.

[53] J. Feldmann. *Messtechnik der Akustik*, chapter 2 Schallpegelmesstechnik und ihre Anwendungen, pages 55–114. Springer, 2010.

[54] J. D. Fieldhouse and N. Ashraf. Observations of the disc/pad interface pressure distribution during variable braking conditions and its influence on brake noise. In *XXVII International μ Symposium*, Bad Neuenahr, Deutschland, 2007.

[55] J. D. Fieldhouse, N. Ashraf, and C. J. Talbot. Measurement of the Dynamic Center of Pressure of a Brake Pad During a Braking Operation. *SAE Technical Paper*, 2006-01-3208, 2006.

[56] J. D. Fieldhouse, D. Bryant, and C. J. Talbot. The Influence of Pad Abutment on Brake Noise Generation. *SAE Technical Paper*, 2011-01-1577, 2011.

[57] J. D. Fieldhouse and T. P. Newcomb. Double Pulsed Holography Used to Investigate Noisy Brakes. *Journal of Optics and Lasers in Engineering*, 25:455–494, 1996.

[58] J. D. Fieldhouse and W. P. Steel. A study of brake noise and the influence of the centre of pressure at the disc/pad interface, the coefficient of friction and calliper mounting geometry. *Proceedings of the Institution of Mechanical Engineers, Part D: Journal of Automobile Engineering*, 217(11):957–974, 2003.

[59] J. D. Fieldhouse, W. P. Steel, and C. J. Talbot. The measurement of the absolute displacement of a noisy disc brake. *Proceedings of the Institution of Mechanical Engineers, Part D: Journal of Automobile Engineering*, 222(7):1121–1140, 2008.

[60] K. Fink. Eine dynamische Eichung von Dehnungsmessstreifen. *Archiv für Eisenhüttenwesen*, 21:137–142, 1950.

[61] M. Fischer and K. Bendel. Hot on the trail of squealing brakes. *Polytec LM INFO: laser measurement systems*, 1:8–9, 2004.

[62] J. Flint, A. Chinnasamy, and A. Stikvoort. New Method to Identify Dynamic Normal Stiffness and Damping of Shims for CAE Modeling. *SAE Technical Paper*, 2010-01-1711, 2010.

[63] J. Flint and J. Hulten. Lining-deformation-induced modal coupling as squeal generator in a distributed parameter disc brake model. *Journal of Sound and Vibration*, 254:1–21, 2002.

[64] J. Flint, J. G. McDaniel, X. Li, A. Elvenkemper, A. Wang, and S.-E. Chen. Measurement and Simulation of the Complex Shear Modulus of Insulators. *SAE Technical Paper*, 2004-01-2799, 2004.

[65] R. A. C. Fosberry and Z. Holubecki. Disc brake squeal: its mechanism and suppression. Technical report 1961/1, Motor Industry Research Association, 1961.

[66] G. Fritz, J.-J. Sinou, J.-M. Duffal, and L. Jézéquel. Effects of damping on brake squeal coalescence patterns - application on a finite element model. *Mechanics Research Communications*, 34(2):181–190, 2007.

[67] G. Fritz, J.-J. Sinou, J.-M. Duffal, and L. Jézéquel. Investigation of the relationship between damping and mode-coupling patterns in case of brake squeal. *Journal of Sound and Vibration*, 307(3-5):591–609, 2007.

[68] O. Giannini and F. Massi. Characterization of the high-frequency squeal on a laboratory brake setup. *Journal of Sound and Vibration*, 310(1-2):394–408, 2008.

[69] T. D. Gillespie. *Fundamentals of Vehicle Dynamics*, chapter 3 Braking Performance, pages 45–78. SAE International, 1992.

[70] J. Grochowicz, C. Agudelo, A. Reich, K.-H. Wollenweber, and H. Abendroth. Brake Dynamometer Test Variability Part 2 - Description of the Influencing Factors. *SAE Technical Paper*, 2011-01-2374, 2011.

[71] J. Grochowicz, K.-H. Wollenweber, C. Agudelo, and H. Abendroth. Brake dynamometer test variability - analysis of root causes. *SAE Technical Paper*, 2010-01-1697, 2010.

[72] L.-O. Gusig and A. Kruse, editors. *Fahrzeugentwicklung im Automobilbau*, chapter 3 Definitionsphase, pages 39–88. Hanser Verlag, 2010.

[73] T. Haag, S. C. González, and M. Hanss. Model validation and selection based on inverse fuzzy arithmetic. *Mechanical Systems and Signal Processing*, 2011.

[74] P. Hagedorn. Modeling disk brakes with respect to squeal. In *17th International Congress of Mechanical Engineering (COBEM)*, Sao Paulo, Brazil, 2003.

[75] P. Hagedorn and U. von Wagner. Smart pads: A new tool for the suppression of brake squeal? In *XXIV International μ Symposium*, Bad Neuenahr, Deutschland, 2004.

[76] C. Halder. Die Rekuperationsbremsung in Elektro- und Hybridfahrzeugen. In *VDI-Fachkonferenz Innovative Bremstechnik*, Stuttgart, Deutschland, 2011.

[77] M. Hanss. *Applied Fuzzy Arithmetic - An Introduction with Engineering Applications.* Springer-Verlag, 2005.

[78] J. Hartley, A. Day, I. Campean, R. G. McLellan, and J. Richmond. Braking System for a Full Electric Vehicle with Regenerative Braking. *SAE Technical Paper*, 2010-01-1680, 2010.

[79] M. B. Hiller. *Correlation between Parameters of the Tribosystem and Automotive Disc Brake Squeal*. PhD thesis, Universität Paderborn, 2006.

[80] M. Hirz. *Advanced Computer Aided Design in Conceptual Automotive Development*, chapter 1 Introduction to automotive development, pages 36–56. Habilitation Thesis, Graz, Austria, 2011.

[81] M. Hirz. An approach of multi disciplinary collaboration in conceptual automotive development. *International Journal of Collaborative Enterprise*, 2011.

[82] D. Hochlenert. *Selbsterregte Schwingungen in Scheibenbremsen: Mathematische Modellbildung und aktive Unterdrückung von Bremsenquietschen*. PhD thesis, Technische Universität Darmstadt, 2006.

[83] D. Hochlenert and P. Hagedorn. Control of Disc Brake Squeal - Modelling and Experiments. *Journal Structural Control and Health Monitoring*, 13(1):260–276, 2006.

[84] K. Hoffmann. *An Introduction to Measurements using Strain Gages*, chapter 3 Selection criteria for strain gages, pages 34–107. Hottinger Baldwin Messtechnik GmbH, 1989.

[85] N. Hoffmann, M. Fischer, R. Allgaier, and L. Gaul. A minimal model for studying properties of the mode-coupling type instability in friction induced oscillations. *Mechanics Research Communications*, 29:197–205, 2002.

[86] N. Hoffmann and L. Gaul. Effects of damping on mode-coupling instability in friction induced oscillations. *Zeitschrift für Angewandte Mathematik und Mechanik*, 83(8):524–534, 2003.

[87] N. Hoffmann and L. Gaul. A sufficient criterion for the onset of sprag-slip oscillations. *Archive of Applied Mechanics*, 73(9-10):650–660, 2004.

[88] M. Horn and N. Dourdoumas. *Regelungstechnik*, chapter Stabilität, pages 85–114. Pearson Studium, 2004.

[89] S. A. Hornig and U. Von Wagner. Experimental Identification of Brake Lining Material Properties Subjected to Combined Static and High Frequency Loading - A Step Towards a Better Prediction of Disc Brake Squeal? *SAE Technical Paper*, 2011-01-2353, 2011.

[90] H. Jacobsson. Aspects of disc brake judder. *Proceedings of the Institution of Mechanical Engineers, Part D: Journal of Automobile Engineering*, 217(6):419–430, 2003.

[91] T. Jearsiripongkul. *Squeal in floating caliper disk brakes: a mathematical model*. PhD thesis, Technische Universität Darmstadt, 2005.

[92] T. Jearsiripongkul and D. Hochlenert. Disk brake squeal: Modeling and active control. In *2006 IEEE Conference on Robotics, Automation and Mechatronics*, Bangkok, Thailand, 2006.

[93] N. H. Kim, D. Won, D. Burris, B. Holtkamp, G. R. Gessel, P. Swanson, and W. G. Sawyer. Finite element analysis and experiments of metal/metal wear in oscillatory contacts. *Wear*, 258(11-12):1787–1793, 2005.

[94] N. M. Kinkaid, O. M. O'Reilly, and P. Papadopoulos. Automotive disc brake squeal. *Journal of Sound and Vibration*, 267(1):105–166, Oct. 2003.

[95] S. Kirchner, J. Sendler, and K. Augsburg. Brake Pedal Feeling of Decoupled Braking Systems for Electric and Hybrid Electric Vehicles. In *Eurobrake*, Dresden, Deutschland, 2012.

[96] S. Kruse, J. Münchhoff, F. Guckeisen, H. S.-E., and N. Hoffmann. The influence of axle components on brake squeal. In *2nd International Munich Chassis Symposium*, Munich, Deutschland, 2011.

[97] S. Kruse, B. Zeumer, P. Reuß, and N. Hoffmann. Detection of critical instabilities in brake squeal based on nonlinear joint characteristics. In *Eurobrake*, Dresden, Deutschland, 2012.

[98] U. Kuhn. E-mobile Vehicle Architectures - Challenges for the Brake System. In *XXX International μ Symposium*, Bad Neuenahr, Deutschland, 2011.

[99] K. Lüders and G. von Oppen. *Bergmann-Schaefer: Lehrbuch der Experimentalphysik*, chapter 14.2 Schallwellen, Schallausbreitung, pages 525–537. Walter de Gruyter, 12 edition, 2008.

[100] H. Lee and R. Singh. Sound radiation from a disk brake rotor using a semi-analytical method. *SAE Technical Paper*, 2003-01-1620, 2003.

[101] G. D. Liles. Analysis of disc brake squeal using finite element methods. *SAE Technical Paper*, 891150, 1989.

[102] R. Limpert. *Brake Design and Safety*, chapter 7 Single Vehicle Braking Dynamics, pages 293–360. SAE International, 1999.

[103] P. Liu, H. Zheng, C. Cai, Y. Y. Wang, C. Lu, K. H. Ang, and G. R. Liu. Analysis of disc brake squeal using the complex eigenvalue method. *Applied Acoustics*, 68(6):603–615, 2007.

[104] S. Lopez and G. L. Sala. A finite element approach to statical and dynamical analysis of geometrically nonlinear structures. *Finite Elements in Analysis and Design*, 46(12):1093 – 1105, 2010.

[105] R. MacNeal. *Finite Elements: Their Design and Performance*, chapter 6 Interpolation Failure: Locking and Shape Sensitivity, pages 203–260. Marcel Dekker, 1993.

[106] S. K. Mahajan, Y. Hu, and K. Zhang. Vehicle disc brake squeal simulation and experiences. *SAE Technical Paper*, 1999-01-1738, 1999.

[107] H. Marschner. Reliably Quiet - New Ways towards Low Noise Brakes. In *XXX International μ Symposium*, Bad Neuenahr, Deutschland, 2011.

[108] H. Marschner and F. Rischbieter. Three-dimensional operational deflection shape analysis of squealing disc brakes. *SAE Technical Paper*, 2004-01-2796, 2004.

[109] F. Massi, L. Baillet, and O. Giannini. Experimental analysis on squeal modal instability. In *International Modal Analysis Conference - IMAC-XXIV*, Saint Louis, MO, USA, 2006.

[110] F. Massi, L. Baillet, O. Giannini, and A. Sestieri. Brake squeal: Linear and nonlinear numerical approaches. *Mechanical Systems and Signal Processing*, 21:2374–2393, 2007.

[111] T. Matsushima, S. Nishiwaki, S. Yamasaki, K. Izui, and M. Yoshimura. An optimal design method for reducing brake squeal in disc brake systems. In *ASME International Design Engineering Technical Conferences & Computers and Information in Engineering Conference (IDETC/CIE)*, Las Vegas, NV, USA, 2007.

[112] MD Nastran. *www.mscsoftware.com*, Accessed on 22/06 2012.

[113] M. Meyer. Recuperation and effects on the brake system. In *XXX International μ Symposium*, Bad Neuenahr, Deutschland, 2011.

[114] M. Meywerk. *CAE-Methoden in der Fahrzeugtechnik*, chapter 8 Finite-Elemente-Vernetzungen, pages 123–140. Springer, 2007.

[115] H. R. Mills. Brake squeak. Technical Report Technical Report 9000 B, Institution of Automobile Engineers, 1938.

[116] F. Moser, M. Fischer, and W. Rumold. *Reibung und Schwingungen in Fahrzeugen, Maschinen und Anlagen*, chapter Dreidimensionale Messung von Betriebsschwingformen quietschender Scheibenbremsen, pages 71–84. VDI-Bericht 1736, 2002.

[117] M. Möser. *Technische Akustik*, chapter 1 Wahrnehmung von Schall, pages 1–18. Springer, 2007.

[118] M. Mueller and G. Ostermeyer. Cellular automata method for macroscopic surface and friction dynamics in brake systems. *Tribology International*, 40(6):942 – 952, 2007.

[119] W. V. Nack. Friction induced vibration: Brake moan. *SAE Technical Paper*, 951095, 1995.

[120] W. V. Nack and S.-E. Chen. *Disc Brake Squeal*, chapter 4 Complex Modes: Analysis and Design, pages 79–94. SAE International, 2006.

[121] L. I. Nagy, J. Cheng, and Y. K. Hu. A new method development to predict brake squeal occurrence. *SAE Technical Paper*, 942258, 1994.

[122] L. I. Nagy, J. Cheng, and Y.-K. Hu. A new method development to predict brake squeal occurrence. In *MSC World User Conf.*, Lake Buena Vista, Florida, USA, 1994.

[123] M. R. North. Disc brake squeal. *Institution of Mechanical Engineers*, C38/76:169–176, 1976.

[124] W. C. Orthwein. *Clutches and Brakes*, chapter 1 Friction Materials, pages 1–16. Marcel Dekker, 2004.

[125] G. P. Ostermeyer. On tangential friction induced vibrations in brake systems. *SAE International Journal of Passenger Cars- Mechanical Systems*, 1:1251–1257, 2008.

[126] G. P. Ostermeyer. Dynamic Friction Laws and their Impact on Friction Induced Vibrations. *SAE Technical Paper*, 2010-01-1717, 2010.

[127] G. P. Ostermeyer and K. Bode. On the dynamic adaptation of the friction layer in the low-frequency range. In *6th European Conference on Braking JEF 2010*, Lille, France, 2010.

[128] G. P. Ostermeyer and K. Bode. Towards a Control Theory Interpretation of Material Ingredients' Impact on Friction Performance. *SAE Technical Paper*, 2010-01-1671, 2010.

[129] G. P. Ostermeyer and N. Perzborn. Dynamic Friction Measurements, Especially for High Power Applications. *SAE Technical Paper*, 2011-01-2373, 2011.

[130] H. Ouyang, L. Baeza, and S. Hu. A receptance-based method for predicting latent roots and critical points in friction-induced vibration problems of asymmetric systems. *Journal of Sound and Vibration*, 321(3-5):1058–1068, 2009.

[131] H. Ouyang, Q. Cao, J. E. Mottershead, and T. Treyde. Vibration and squeal of a disc brake: modelling and experimental results. *Proceedings of the Institution of Mechanical Engineers, Part D: Journal of Automobile Engineering*, 217(10):867–875, 2003.

[132] H. Ouyang, W. Nack, Y. Yuan, and F. Chen. On Automotive Disc Brake Squeal Part II: Simulation and Analysis. *SAE Technical Paper*, 2003-01-0684, 2003.

[133] H. Ouyang, W. Nack, Y. Yuan, and F. Chen. Numerical analysis of automotive disc brake squeal: a review. *International Journal Vehicle Noise and Vibration*, 1:207–231, 2005.

[134] A. T. Papinniemi, J. C. S. Lai, and J. Zhao. Vibro-acoustic studies of brake squeal. In *Acoustics*, Queensland's Gold Coast, Australia, 2004.

[135] S. Park, W. Jeong, and K. Park. Improvement of Brake Squeal Using Shape Optimization Based on Frequency Separation. In *Eurobrake*, Dresden, Deutschland, 2012.

[136] H. Parkus. *Mechanik der festen Körper*, chapter 8 Lagrangsche Gleichungen, pages 137–159. Springer, 2005.

[137] K. Popp, M. Rudolph, M. Kröger, and M. Lindner. *Reibung und Schwingungen in Fahrzeugen, Maschinen und Anlagen*, chapter Mechanisms to generate and to avoid friction induced vibrations, pages 1–15. VDI-Bericht 1736, 2002.

[138] M. Putz, B. Faul, C. Wunsch, and J. E. Morgan. The VE Elektro Mechanical Brake with Fully Integrated Actuators in a SUV Class Vehicle. In *Eurobrake*, Dresden, Deutschland, 2012.

[139] M. H. Putz. VE Mechatronic Brake: Development and Investigations of a Simple Electro Mechanical Brake. *SAE Technical Paper*, 2010-01-1682, 2010.

[140] M. H. Putz, C. Wunsch, and J. E. Morgan. Wheel Optimized Brake Torque at the VE Mechatronic Brake. *SAE Technical Paper*, 2011-01-2358, 2011.

[141] D. N. Ramasami, J. F. Brunel, P. Dufrénoy, G. Rejdych, and T.Chancelier. Correction Between Modeling and Experiments of a Simplified Disc Brake System for Squeal Analysis. In *Eurobrake*, Dresden, Deutschland, 2012.

[142] P. Rieth. Trends in Antrieb und Fahrwerk - Auswirkungen auf das Bremssystem. In *VDI-Fachkonferenz Innovative Bremstechnik*, Stuttgart, Deutschland, 2011.

[143] SAE International Surface Vehicle Recommended Practice. Disc and Drum Brake Dynamometer Squeal Noise Matrix. *SAE Standard*, J2521, Rev. Jan. 2006.

[144] P. G. Sanders. Friction Material Elastic Property Round Robin Study. *SAE Technical Paper*, 2007-01-3940, 2007.

[145] A. Sardá, M. Haag, H. Winner, and M. Semsch. Experimental Investigations of Hot Spots and Thermal Judder. *SAE Technical Paper*, 2008-01-2544, 2008.

[146] S. Schlagner and U. von Wagner. Evaluation of automotive disk brake noise behavior using piezoceramic actuators and sensors. *Proceedings in Applied Mathematics and Mechanics*, 7, 2007.

[147] S. Schlagner and U. von Wagner. Fast characterization of brake squeal behavior. *SAE Technical Paper*, 2009-01-3006, 2009.

[148] R. Schroth, N. Hoffmann, and R. Swift. Mechanism of Brake Squeal - from Theory to Experimentally Measured Mode Coupling. In *International Modal Analysis Conference - IMAC-XXII*, Dearborn, Mi, USA, 2004.

[149] K. Shin, M. J. Brennan, J.-E. Oh, and C. J. Harris. Analysis of disk brake noise using a two-degree-of-freedom model. *Journal of Sound and Vibration*, 254(5):837 – 848, 2002.

[150] D. Sinclair. Frictional vibrations. *Journal of Applied Mechanics*, 77:207–213, 1955.

[151] G. Spelsberg-Korspeter. Breaking of symmetries for stabilization of rotating continua in frictional contact. *Journal of Sound and Vibration*, 322:798 – 807, 2009.

[152] G. Spelsberg-Korspeter. Structural optimization for the avoidance of self-excited vibrations based on analytical models. *Journal of Sound and Vibration*, 329(23):4829 – 4840, 2010.

[153] G. Spelsberg-Korspeter, D. Hochlenert, and P. Hagedorn. Non-linear investigation of an asymmetric disk brake model. *Proceedings of the Institution of Mechanical Engineers, Part C: Journal of Mechanical Engineering Science*, 225(10):2325–2332, 2011.

[154] D. Stanef, A. Papinniemi, and J. Zhao. From Prototype to Production - The Practical Nature of Brake Squeal Noise. *SAE Technical Paper*, 2006-01-3217, 2006.

[155] E. Q. Sun. Shear Locking and Hourglassing in MSC Nastran, ABAQUS and ANSYS. In *In MSC Software Corporation's 2006 Americas Virtual Product Development Conference: Evolution to Enterprise Simulation*, Phoenix, AZ, USA, 2006.

[156] C. Talbot and J. D. Fieldhouse. Investigations of in plane disc vibration using laser holography. *SAE Technical Paper*, 2002-01-2607, 2002.

[157] C. Talbot and J. D. Fieldhouse. Fourier analysis of holographic data from a noisy disc brake and its implication for modelling. *Proceedings of the Institution of Mechanical Engineers, Part D: Journal of Automobile Engineering*, 217(11):975–983, 2003.

[158] J. K. Thompson. *Brake NVH - Testing and Measurements*, chapter 4 Laboratory Testing, pages 55–86. SAE International, 2011.

[159] A. Tonchev. *Co-Simulation von Fahrzeugbremsen unter Berücksichtigung des thermischen Verhaltens.* PhD thesis, Technische Universität Graz, 2008.

[160] A. Tonchev, W. Hirschberg, W. Sextro, Z. Major, and J. Neges. Modellierung der Hysterse- und Adhäsionseffekte zwischen Bremsbelag und Bremsscheibe. In *27th μ Symposium*, Bad Neuenahr, Deutschland, 2007.

[161] W. W. Tworzydlo, O. N. Hamzeh, W. Zaton, and T. J. Judek. Friction-induced oscillations of a pin-on-disk slider: Analytical and experimental studies. *Wear*, 236(1-2):9–23, 1999.

[162] P. P. J. van den Bosch and A. C. van der Klauw. *Modeling, Identification and Simulation of Dynamical Systems*, chapter 3 Black-box model representations, pages 43–70. CRC Press, 1994.

[163] G. Vermot Des Roches, E. Balmes, P. Thierry, and R. Lemaire. Time simulation of squeal phenomena in realistic brake models. In *International Conference on Noise and Vibration Engineering*, Leuven, Belgien, 2008.

[164] U. von Wagner, D. Hochlenert, and P. Hagedorn. Minimal models for disk brake squeal. *Journal of Sound and Vibration*, 302(3):527–539, 2007.

[165] M. Vorländer. *Messtechnik der Akustik*, chapter 9 Digitale Signalverarbeitung in der Messtechnik, pages 537–576. Springer, 2010.

[166] J. Wahlström, A. Söderberg, and U. Olofsson. A cellular automaton approach to simulate the contact situation between the pad and disc in disc brakes. In *6th European Conference on Braking JEF 2010*, Lille, France, 2010.

[167] J. Wallaschek, K.-H. Hach, U. Stolz, and P. Mody. A Survey of the Present State of the Friction Modelling in the Analytical and Numerical Investigation of Brake Noise Generation. In *ASME Design Engineering Technical Conferences and Computers in Engineering Conference (DETC)*, Las Vegas, NV, USA, 1999.

[168] B. Wernitz and N. Hoffmann. Recurrence analysis and phase space reconstruction of irregular vibration in friction brakes: Signatures of chaos in steady sliding. *Journal of Sound and Vibration*, 331(16):3887–3896, 2012.

[169] S. Yang and R. F. Gibson. Brake vibration and noise: Reviews, comments, and proposals. *International Journal of Materials and Product Technology*, 12:496–513, 1997.

[170] D. E. Yuhas, J. J. Ding, and S. Venkatesan. Non-linear aspects of friction material elastic constants. *SAE Technical Paper*, 2006-01-3193, 2006.

[171] O. C. Zienkiewicz. *Methode der finiten Elemente*, chapter 8 Gekrümmte, isoparametrische Elemente und numerische Integration, pages 136–157. Hanser Verlag, 1975.

[172] A. Zomotor. *Fahrwerktechnik: Fahrverhalten.* Vogel Verlag, 1991.

List of Figures

List of Tables